BILINGUAL PUBLISHING GROUP

Volume 5 · Issue 3 · July 2023 ISSN 2810-9384(Online)

Advances in Geological and Geotechnical Engineering Research

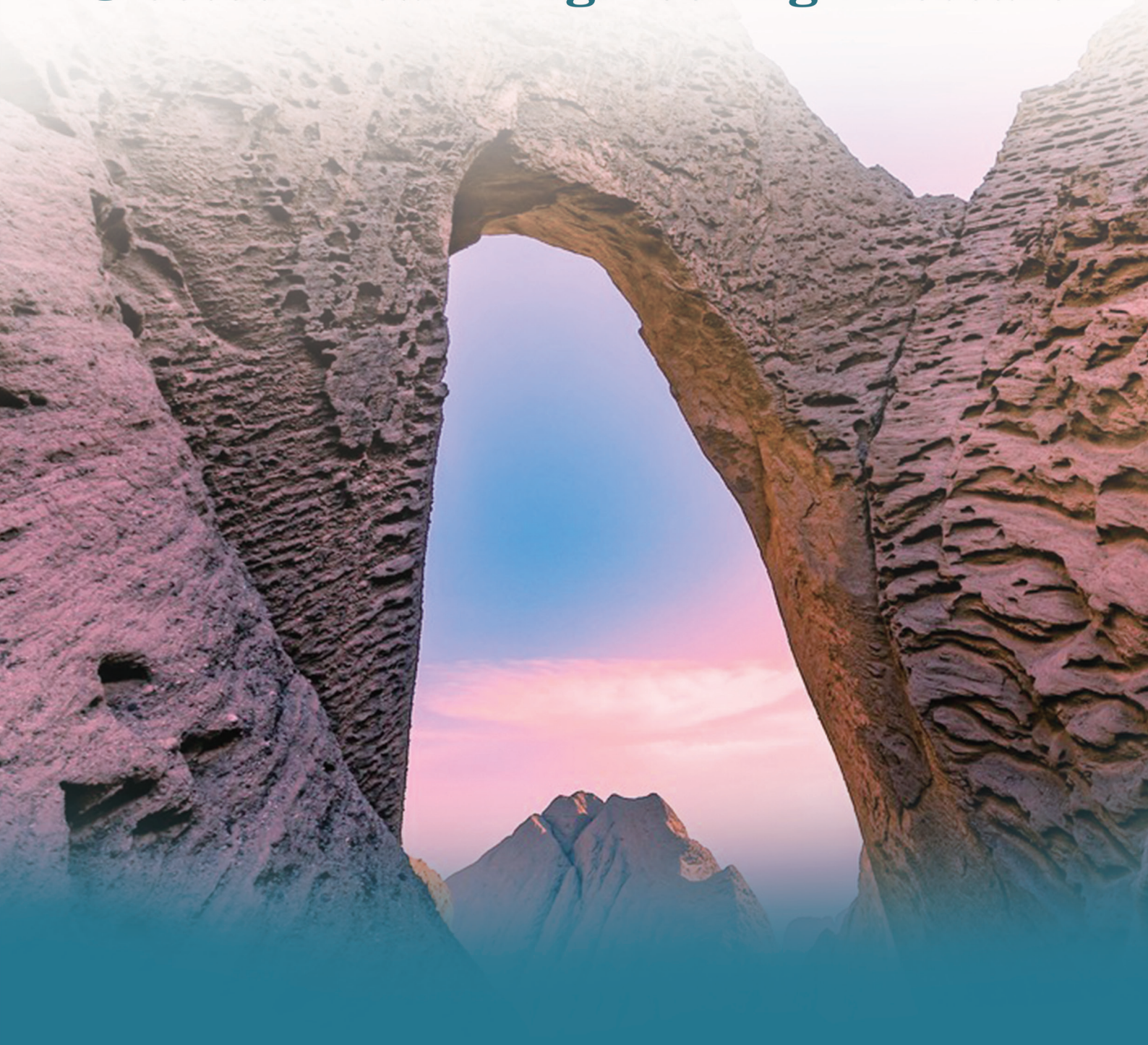

BILINGUAL PUBLISHING GROUP

Editor-in-Chief

Prof. Sayed Hemead
Cairo University, Egypt

Prof. Wengang Zhang
Chongqing University,China

Associate Editor

Prof. Amin Beiranvand Pour
Universiti Malaysia Terengganu, Malaysia

Editorial Board Members

Salvatore Grasso, Italy
Shenghua Cui, China
Golnaz Jozanikohan, Iran
Mehmet Irfan Yesilnacar, Turkey
Ziliang Liu, China
Sunday Ojochogwu Idakwo, Nigeria
Jianwen Pan, China
Wen-Chieh Cheng, China
Wei Duan, China
Intissar Farid, Tunisia
Bingqi Zhu, China
Zheng Han,China
Vladimir Aleksandrovich Naumov, Russian Federation
Dongdong Wang, China
Jian-Hong Wu, Taiwan China
Abdel Majid Messadi, Tunisia
Vasiliy Anatol'evich Mironov, Russian Federation
Maysam Abedi, Iran
Anderson José Maraschin, Brazil
Alcides Nobrega Sial, Brazil
Ezzedine Saidi, Tunisia
Mokhles Kamal Azer, Egypt
Ntieche Benjamin, Cameroon
Jinliang Zhang, China
Kamel Bechir Maalaoui, Tunisia
Shimba Daniel Kwelwa,Tanzania
Antonio Zanutta, Italy
Swostik Kumar Adhikari, Nepal
Hu Li, China
Irfan Baig, Norway
Shaoshuai Shi, China
Sumit Kumar Ghosh, India
Bojan Matoš, Croatia
Massimo Ranaldi, Italy
Gehan Mohammed, Egypt
Márton Veress, Hungary
Vincenzo Amato, Italy
Siva Prasad BNV, India
Ahm Radwan, Egypt
Nadeem Ahmad Bhat, India
Mojtaba Rahimi, Iran
Mohamad Syazwan Mohd Sanusi, Malaysia
Sohrab Mirassi, Iran
Zhouhua Wang, China
Bahman Soleimani, Iran
Luqman Kolawole Abidoye, Nigeria
Tongjun Chen, China
Saeideh Samani, Iran
Khalid Elyas Mohamed E.A., Saudi Arabia
Mualla Cengiz, Turkey
Hamdalla Abdel-Gawad Wanas, Saudi Arabia
Gang Li, China
Williams Nirorowan Ofuyah, Nigeria
Ashok Sigdel, Nepal
Ramesh Man Tuladhar, Nepal
Mirmahdi Seyedrahimi-Niaraq, Iran
Olukayode Dewumi Akinyemi, Nigeria
Raphael Di Carlo Santos, Brazil
Zhaofei Chu, China
Zhenhua Zhou, China

Volume 5 Issue 3 • July 2023 • ISSN 2810-9384 (Online)

Advances in Geological and Geotechnical Engineering Research

Editor-in-Chief

Prof. Sayed Hemead

Prof. Wengang Zhang

BILINGUAL PUBLISHING GROUP

BILINGUAL PUBLISHING GROUP

Volume 5 | Issue 3 | July 2023 | Page1-68

Advances in Geological and Geotechnical Engineering Research

Contents

Articles

BILINGUAL PUBLISHING GROUP

Advances in Geological and Geotechnical Engineering Research

https://ojs.bilpublishing.com/index.php/agger

ARTICLE

Contribution of GIS to Hydromorphometric Characterization of the Nkoup Watershed (Nun Plain-Cameroon)

***Paul Bertrand Tsopkeng*[1*], *Josiane Feugue Kenfack*[2], *David Guimolaire Nkouathio*[3], *Charles Antoine Basseka*[1], *Leonel Koudjou Tsague*[4]**

[1] *Postgraduate School for Pure and Applied Sciences, The University of Douala, P.O.Box 2701, Douala, Cameroon*

[2] *Department of Geography, Faculty of Letters and Human Sciences, P.O.Box 49, The University of Dschang, Cameroon*

[3] *Department of Earth Sciences, Faculty of Sciences, P.O.Box 67, The University of Dschang, Dschang, Cameroon*

[4] *Department of Hydraulics and Water Management, National Advanced School of Engineering of Maroua, The University of Maroua, P.O.Box 46, Maroua, Cameroon*

ABSTRACT

The Nkoup watershed (10°35'-10°47'E and 5°27'-5°42'N) is a volcanic zone situated in Nun Plain West Cameroon. The high fertility of the soils makes it a strategic agropastoral area where water resources are heavily exploited and used for several purposes. Due to human activities, soils and water resources are deteriorating, giving birth to water pollution and hydromorphological hazards. This work aims to determine the hydromorphometric parameters of the Nkoup watershed so that the data obtained help in the sustainable management of water resources and conservation of soil. To achieve this aim, various data were collected from DEM dataset derived from SRTM and processed in specialized software (QGIS and ArGIS). The simplified hydrological balance was calculated using the upstream approach. The Nkoup watershed has: Axial length $\mathbf{L_{ax}}$ = **25.8** km, Axial Width $\mathbf{W_{ax}}$ **= 11.1** km, Perimeter **P** = **132.6** km, Area **A** = **173.7** km^2, Average Altitude $\mathbf{H_a}$ = **1726.3** m, Compactness Index **Icomp** = **2.8**, Relief ratio Rr = **3.9** m/km, Circularity ratio **Rc = 0.1**, Elongation ratio **R = 0.1**, Drainage texture ratio **Rt = 0.6**, Drainage density $\mathbf{D_d}$ = **0.5** km/km^2. Stream Frequency **Fs = 0.4**, Channel Sinuosity Index **CSI = 0.8**, Stream gradient **Sg = 0.6** and global slope Index **Ig** = **6.8** m/km. The specific height Difference **Ds** = **89.4** m shows moderate relief. The precipitation and evapotranspiration are unevenly distributed. With **P** = **187.7** mm/an, **ETP** = **953.4** mm/an, **Q** = **4.2** m^3/s, **R** = **762.5** mm/an, **ETR** = **832.3** mm/an and **I** = **282.9** mm/an. The Nkoup, **36.9** km long, has a sinuous aspect due to the low slope and the high CSI. The piezometric levels vary according to the seasons and the groundwater flow follows the N-S direction as surface flow.

Keywords: Nkoup watershed; Water resources; Hydromorphometric parameters; Hydrological balance; Groundwater flows direction

*CORRESPONDING AUTHOR:

Paul Bertrand Tsopkeng, Postgraduate School for Pure and Applied Sciences, The University of Douala, P.O.Box 2701, Douala, Cameroon; Email: paultsopkeng@yahoo.fr

ARTICLE INFO

Received: 13 March 2023 | Revised: 28 April 2023 | Accepted: 5 May 2023 | Published Online: 8 June 2023

DOI: https://doi.org/10.30564/agger.v5i3.5534

CITATION

Tsopkeng, P.B., Kenfack, J.F., Nkouathio, D.G., et al., 2023. Contribution of GIS for Hydromorphometric Characterization of the Nkoup Watershed (Nun Plain-Cameroon). Advances in Geological and Geotechnical Engineering Research. 5(3): 1-15. DOI: https://doi.org/10.30564/agger.v5i3.5534

COPYRIGHT

Copyright © 2023 by the author(s). Published by Bilingual Publishing Group. This is an open access article under the Creative Commons Attribution-NonCommercial 4.0 International (CC BY-NC 4.0) License. (https://creativecommons.org/licenses/by-nc/4.0/).

1. Introduction

The Nkoup watershed (173.7 km^2) is located in the South-East of the Nun Plain (West Region-Cameroon), between longitudes 10°35'-10°47'E and latitudes 5°27'-5°42'N. It is a volcanic zone that includes the localities of Foumbot, Baïgom and a part of Koutaba and Kouoptamo (**Figure 1a**). The high fertility of the soils makes it a strategic agropastoral area where water resources are heavily exploited and used for several purposes. Due to human activities, soils and water resources are deteriorating, giving birth to water pollution [1] and hydromorphological hazards. Thus, it is important to determine the hydromorphometric parameters of this watershed so that the data obtained contribute to the prevention of water pollution and help in the sustainable management of water resources (water-related conflicts); and conservation of soil in this area. A watershed is a natural hydrological unit that generates surface runoff from the rainfall which flows through channels, streams, rivers, lakes or oceans [2-5]. Prioritization of watershed is a crucial part of watershed management as it contains some sensitive information regarding surface hydrology and is able to answer some crucial questions such as where to construct check dam, reservoir, embankment, etc., to minimize soil erosion, flooding, bank erosion and maximize infiltration [4]. Morphometric characteristics influence watershed processes [6-9], describe geomorphology and hydrogeology features [10,11] and provide valuable information on water resources potential assessment and management [12]. The geomorphometric analysis was distinguished for the first time by Horton [13]; it was further reviewed by Evans [14]. The traditional approach in watershed prioritization from basin morphometry is based on calculating compound parameter values, as averages of individual parameter values [5]. In recent studies, Hamdan [6] notes that geospatial technology in earth science is an emerging tool by which the hydrogeologist can assess the watershed properties using Geographic Information System (GIS), Remote Sensing (RS) and Global Positioning System (GPS). Gis is ideal for morphometric analysis because of its strength in visualizing, processing and quantifying topographic attributes [15]. This study is very important due to the fact that it permits to implementation of some parameters of hydro-morphometric characteristics of Nkoup watershed and brings out the solutions to various hydrological problems for Nkoup watershed management. Located on the Cameroon volcanic line, it is marked by the following geological formations: Alluviums, Rhyolites, Basalts, Pyroclasts and migmatitic gneiss (**Figure 1b**). The **alluvial formations** are made up of a mixture of weathering products (mud and sand) and partly cover the gneissic bedrock. **Ryolites** outcrop in the form of domes and present a porphyritic texture made up of an arrangement of K-feldspars (Or_{97-89}), Na-feldspars (Ab_{99-88}), quartz and Fe-Ti oxides [16]. **Basalts** are present in two types: Old basalts or plateau basalts that present a porphyritic microlitic texture consisting of olivine and pyroxene phenocrists; and recent basalt (vacuolar) with porphyritic microlitic texture made up of olivine and pyroxene phenocrists. Microscopically, the mineralogy of these basalts is homogeneous: Olivine, clino-pyroxene, plagioclase, Fe-Ti oxide and chromite. The geochemistry of these lavas shows enrichment in SiO_2 (41.2-46.4%), Al_2O_3 (11.4-17.1%), Na_2O (2.4-3.9%), K_2O (1.0-1.9%) and impoverishment in MgO (13.8-4.6%), CaO (11.9-7.6%) [16]. **Pyroclastic formations** composed of Pumices, Slags, Lapillis and volcanic ashes occupy about a third of the watershed with thicknesses varying from 1 to more than 15 m. They have two colors (red and black) and are strongly concentrated around the craters forming cones. The bedrock consists of strongly fractured migmatitic gneiss and presents quartzo-feldspatic veins with N25°-40°E orientation. It has a migmatitic texture made from the following minerals: Quartz, Feldspars, Biotite, Amphibole and Muscovite.

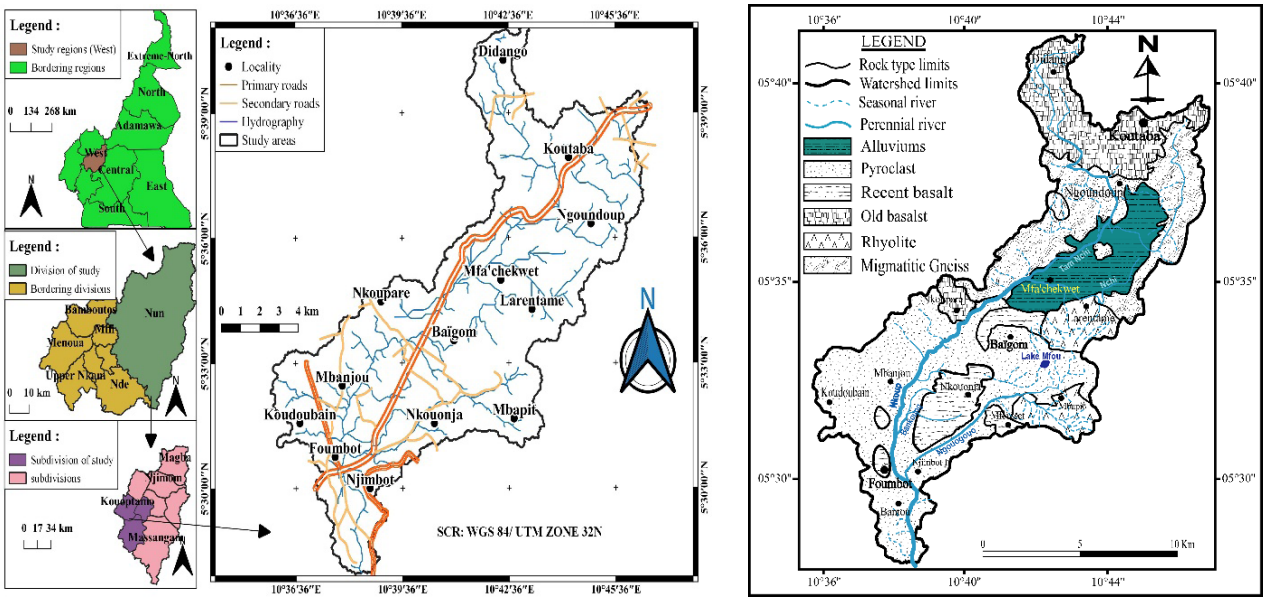

(a) (b)

Figure 1. (a) Localisation and (b) geological units of the Nkoup watershed.

2. Methodology

The Digital Elevation Model (DEM) is the major dataset for various applications [17,18]. Hydrological analysis in particular relies heavily on DEM data [20-22]. To achieve this aim, GIS data were collected from DEM dataset derived from Shuttle Radar Topography Mission (SRTM) with 30 m resolution and processed in specialized software. Several types of data were used: Cartographic data (Landsat ETM+ images downloaded in April 2020 from the website www.earthexplorer.usgs.gov); Radar SRTM images downloaded in April 2020 from the website www.earthexplorer.usgs.gov; Google earth images; 1/200000 scale geological maps from National Institute of Cartography of Cameroon); Climatic data (precipitation and temperature obtained in four meteorological stations (Foumbot, Kouoptamo, Koutaba and Baïgom) downloaded in April 2020 from the website www.climate-data.org; Evapotranspiration (ETP and ETR) calculated from the precipitation and temperature of each station and piezometric data. These data were stored and processed in specialized software (QGIS and ArGIS 10.3). Geomorphometric information was digitized and georeferenced with WGS84/UTM zone 32°N in order to produce thematic maps. Some of the parameters were measured using ArGIS tools and calculated using mathematical formulas developed by several authors and vector models.

The simplified hydrological balance was calculated using the upstream approach. It was a question of determining the numerical value of each term of the following hydrological balance formula (Equation (1)).

$$\mathbf{P = I + R + ETR} \quad (1)$$

In this formula, the hard-to-quantify real evapotranspiration was determined from the monthly rainfall data and the potential evapotranspiration. It is therefore necessary to calculate the ETP. Its expression is given by the Thornthwaite [23] formula as Equation (2):

$$\mathbf{ETP} = 16\left(10\frac{T}{I}\right)^{a})\lambda \quad (2)$$

with: $\mathbf{a = 6{,}75.10^{-7}\, I^3 - 7{,}71.10^{-5} I^2 + 1{,}79.10^{-2} + 0{,}49239}$;

$\mathbf{I} = \sum_{i=1}^{12}(i)$ **and** $i = \left(\frac{T}{5}\right)^{1{,}514}$.

with: **ETP** = mensual potential evapotranspiration for the fictitious month of 30 days and a theoretical period of 12 hours sunshine; **T** = Monthly average temperature in °C for the month considered; **I** = An-

nual thermal Index; **a** is a function of thermal index and **λ** = Correction coefficient according to the latitude and the month.

To determine **ETR**, Thorntwaite's algorithm was used. It is based on the easily usable reserve (RFU) according to the following situations for **i** ranging from **1** to **12** in Equations (3)-(7).

a) If $P_{(i+1)} \geq ETP_{(i+1)}$ hence $ETR_{(i+1)} = ETP_{(i+1)}$ (3)

b) If $P_{(i+1)} = ETP_{(i+1)}$ hence $ETR_{(i+1)} = ETP_{(i+1)} = P_{(i+1)}$ (4)

c) If $P_{(i+1)} < ETP_{(i+1)}$ hence:

- $ETR_{(i+1)} = RFU_i + P_{(i+1)}$ *if* $RFU_i + P_{(i+1)} < ETP_{(i+1)}$ (5)

- $ETR_{(i+1)} = ETP_{i+1}$ if $RFU_i + P_{(i+1)} \geq ETP_{(i+1)}$ (6)

- $ETR_{(i+1)} = P_{(i+1)}$ if $RFU_i + P_{(i+1)} < ETP_{(i+1)}$ with $RFU_i = 0$ (7)

The easily usable reserve (RFU) is determined as Equation (8):

$$RFU_{(i+1)} = RFU_i + P_{(i+1)} - ETP_{(i+1)} \text{ ; with } 0 \leq RFU \leq 100 \quad (8)$$

IfP ≥ ETR, there is an excess **P – ETR** which is assigned in priority to the **RFU** and if **RFU = RFU-max(100)**, this excess is rather assigned to the flow. After the calculation of the RFU, any negative value is reduced to zero while any value greater than 100 is reduced to 100.

3. Results and interpretation

3.1 Relief of the Nkoup watershed

The relief of the Nkoup watershed is marked by a vast plain surrounded by cones/summits at varying altitudes, which the highest, Mount Mbapit culminates at 1840 m. This relief is the result of an important more or less recent volcanic activity. The lower part covers about 85% of the watershed and is made up of geomorphological units located between 980 and 1220 m (**Figure 2a**). The steep slopes are encountered in the East and the far North where the geomorphological units are the highest (**Figure 2b**).

3.2 Climate of the Nkoup watershed

The climate of the Nkoup watershed is tropical sudano-guinean with two seasons [24]. The rainy season extends from mid-March to mid-November and the dry season from mid-November to mid-March (**Figure 3a**). The average annual rainfall is 156.5 mm with minimums in December and maximums in August. It varies decreasingly according to the year (between 2016 and 2020) with the rainy year 2016 and the least rainy year 2017 (**Figure 3b**).

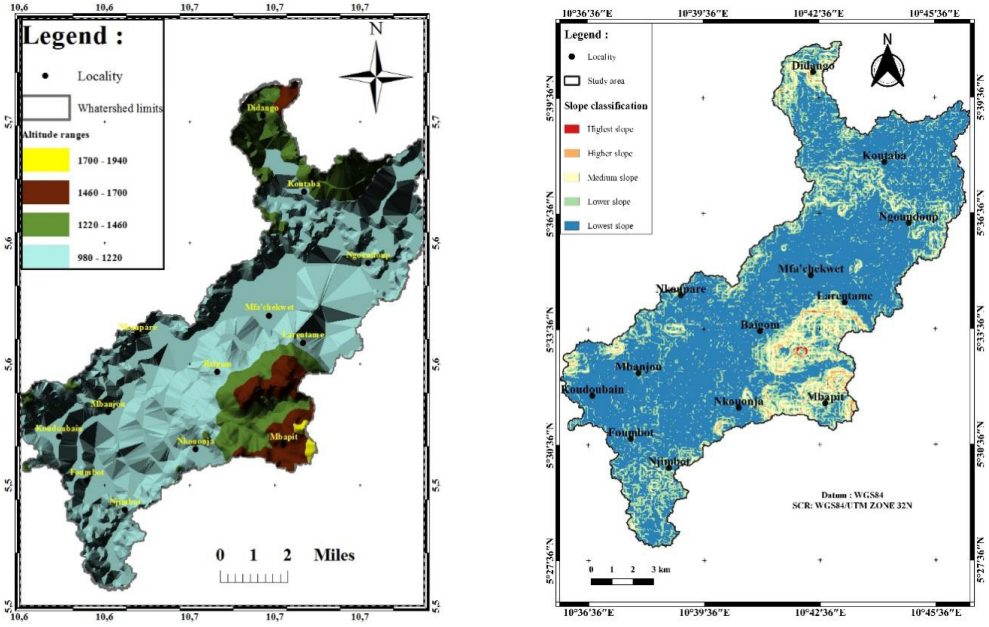

(a) (b)

Figure 2. Maps showing (a) the relief units; (b) the distribution of slopes in the Nkoup watershed.

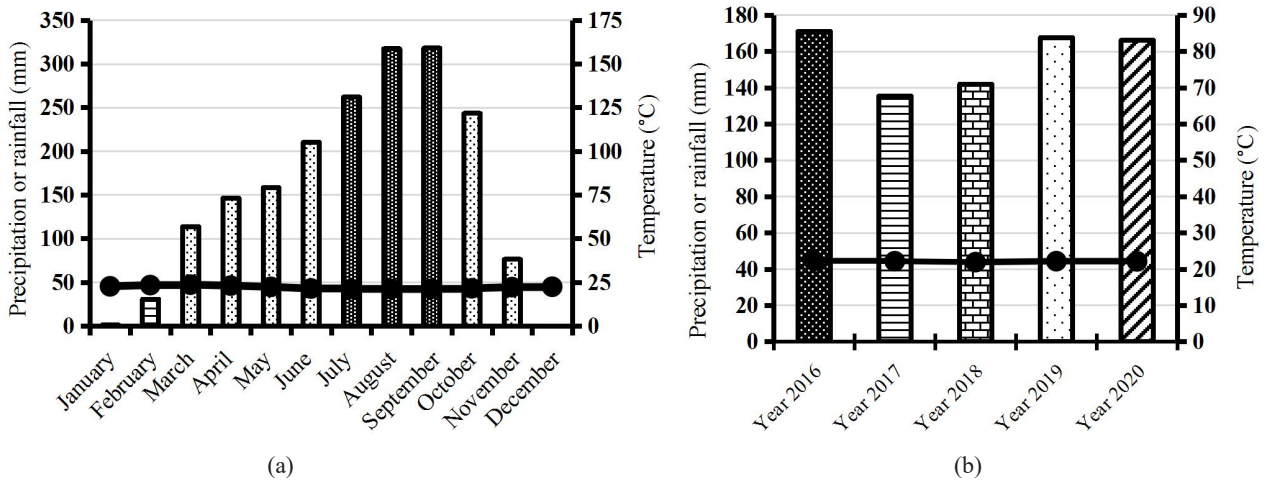

Figure 3. Ombrothermal diagram of (a) monthly averages (b) annual rainfall averages over 5 years, from 2016 to 2020 from Foumbot meteorological station [25].

The cartographic interpolation of data from the following meteorological stations: Foumbot, Kouoptamo, Koutaba and Baïgom makes it possible to note unequal distribution of rainfall and evapotranspiration in the watershed. Rainfall is low in the South-West and the East; and high in the West and far North (**Figure 4a**). The ETR is low in the centre and the North; and high in the extreme South-West of the watershed (**Figure 4b**).

The aridity index $\mathbf{I_a}$ is calculated by De Martonne [26] formula:

$$\mathbf{I_a = 12P_m/T_m + 10} \quad (9)$$

with $\mathbf{P_m}$ and $\mathbf{T_m}$ respectively the average monthly rainfall and temperature. De Martonne defines the following aridity index classes: $\mathbf{I_a < 20}$ (arid); **20 <**

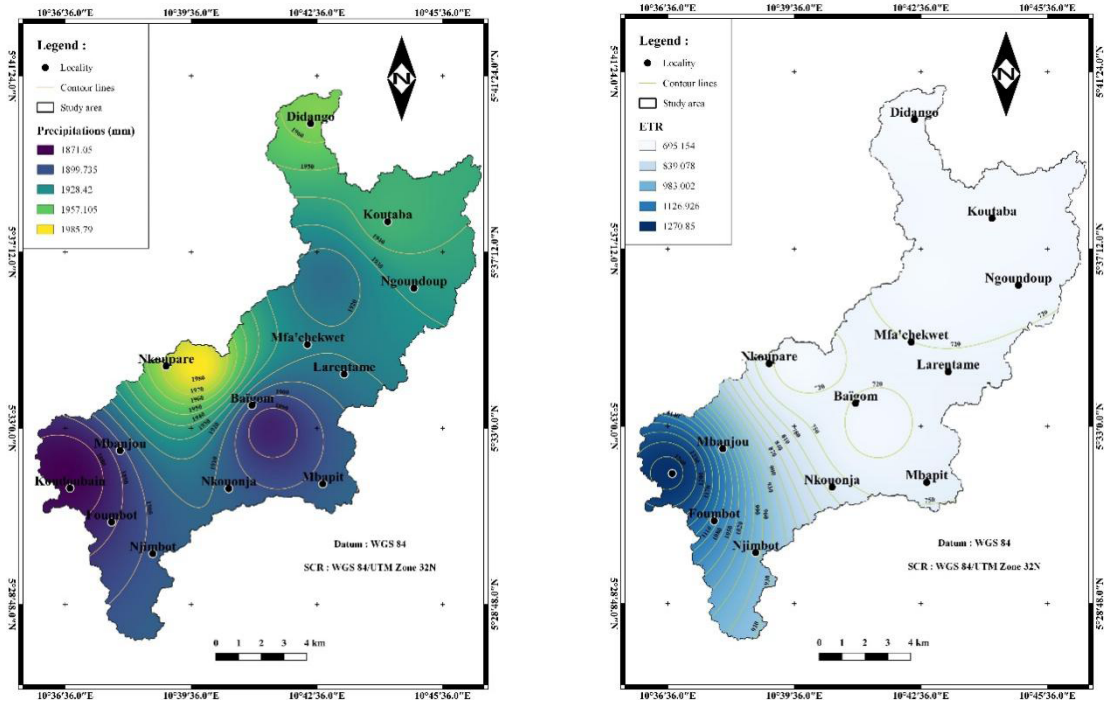

Figure 4. Map showing the distribution of (a) precipitation, (b) ETR in the Nkoup watershed.

$\mathbf{I_a < 50}$ (semi-arid); $\mathbf{50 < I_a}$ (wet). It appears from the results in **Table 1** that December, January and February are the arid months; November and March are semi-arid months; and the months from April to October are wet. Overall, with an average aridity index of **58.39**, the Nkoup watershed is located in a wet zone.

3.3 Hydro-morpho-metric parametres of the Nkoup watershed

Hydrography and hydrographic network density of the Nkoup watershed

The Nkoup is the main river of the watershed and Nchi, Tam Nchi and Ngouogouo are its important tributaries. Lake Mfou, located on one of the peaks of the Mbapit massif constitutes the most important surface water plan. It is a crater lake that has no (visible) outlet. It is noted the predominance of seasonal streams and dry drains to the East of the watershed and around Mount Mbapit. According to the Schumm [27] classification, the Nkoup watershed has an arborescent hydrographic network made up of third-order rivers. The source of the river Nkoup is located at an altitude of **1224** m (Didango) and its outlet is situated at Mbatou, at an altitude of **980** m (**Figure 5**).

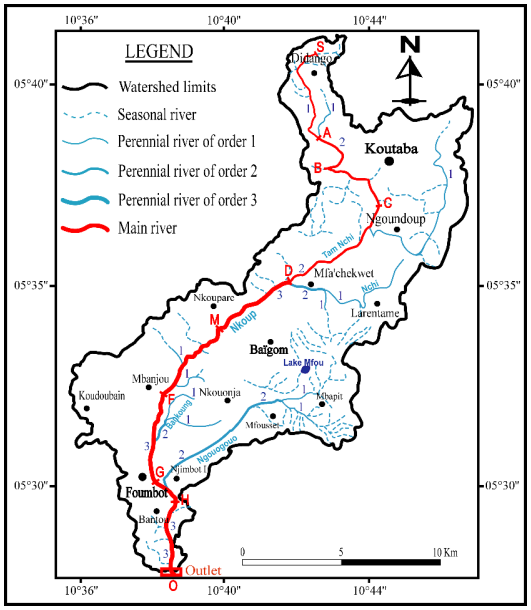

Figure 5. The main rivers map of the Nkoup system.

The stream frequency

The Stream Frequency (**Fs**) is the ratio between the number of flow channels per unit area of the watershed [13]. It is expressed by Equation (10):

$$\mathbf{Fs = Ni/A} \quad (10)$$

Ni = Number of flow channels (**Ni = 71**) and **A** = Area of the watershed (**173.7** km^2), the Stream Frequency of Nkoup watershed is **Fs = 0.41** km^{-2}. This value is related to the high relief of the zone [28].

Table 1. Aridity index of the Nkoup watershed.

Month	P_m (mm)	T_m (°C)	$12P_m$	T_m+10	I_a	Observations
January	0.6	22.58	7.2	32.58	0.22	Arid
February	30.74	23.28	368.88	33.28	11.08	Arid
March	113.66	23.52	1363.92	33.52	40.69	Semi-arid
April	146.26	22.98	1755.12	32.98	53.22	Wet
May	158.32	22.28	1899.84	32.28	58.86	Wet
June	210.34	21.34	2524.08	31.34	80.54	Wet
July	262.12	21.1	3145.44	31.1	101.14	Wet
August	317.48	21.04	3809.76	31.04	122.74	Wet
September	318.26	21.12	3819.12	31.12	122.72	Wet
October	243.56	21.46	2922.72	31.46	92.90	Wet
November	76.4	22.12	916.80	32.12	28.54	Semi-arid
December	00.00	22.34	00.00	32.34	00.00	Arid
Average	156.48	22.1	1877.76	32.1	59.39	Wet zone

Drainage density

The drainage density ($\mathbf{D_d}$) is the ratio of the total stream lengths in the hydrographic network per unit area of the watershed [13]. It is determined by Equation (11):

$$\boldsymbol{D_d = \frac{\sum_{i=1}^{n} L_i}{S}} \quad (11)$$

$\mathbf{L_i}$ = Total Stream Lengths ($\sum \mathbf{L_i}$ = **83.376** km) and **A** = Area of the watershed (**173.7** km^2), $\mathbf{D_d}$ = **0.48** km/km^2. The cartographic interpolation of the data made it possible to obtain **Figure 6**.

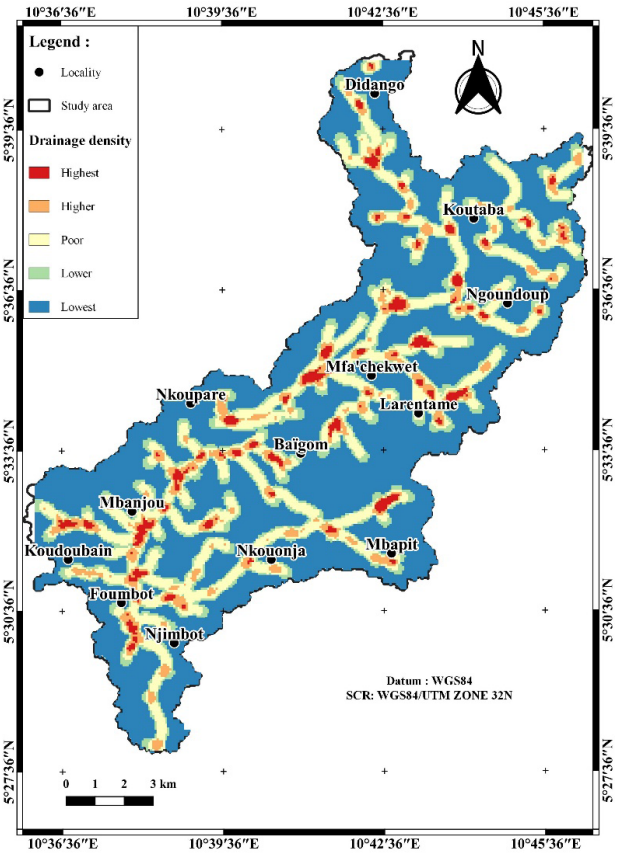

Figure 6. The drainage density map of the Nkoup system.

The constant of Channel Maintenance (**C**) is the inverse of drainage density and corresponds to the area required to maintain stable hydrological conditions in a unit hydrographic vector of the watershed [26,27]. It is determined by Equation (12):

$$\mathbf{C = 1/Dd} \quad (12)$$

with $\mathbf{D_d}$ = drainage density (**0.48** km/km^2), **C** = **2.083** km^2/km.

Hypsometry of the Nkoup watershed

Figure 7 shows the delimitation of the Nkoup watershed according to the contour lines. The Nkoup watershed has: Axial length $\mathbf{L_{ax}}$ = **25.83** km, Axial width $\mathbf{W_{ax}}$ = **11.11** km, Perimeter **P** = **132.645** km and an area **A** = **173.7** km^2.

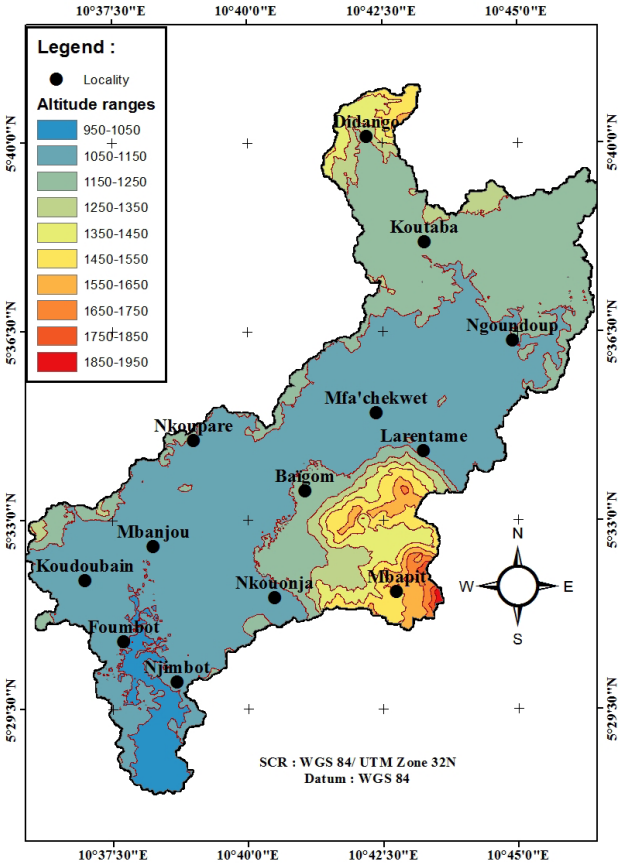

Figure 7. Hypsometric map of the Nkoup watershed.

This distribution made it possible to obtain 10 intervals of 100 m equidistance. The partial and cumulated areas of each slice are presented in **Table 2**.

The hypsometric curve in **Figure 8** is established by planimetry of the surfaces corresponding to the definition of the ordinate for each of the contour lines [29]. This curve is a representation of "altitude range as a function of areas and cumulated areas".

The Nkoup watershed has an average altitude of **1726.31** m; $\mathbf{H_{5\%}}$ = **1473** m; $\mathbf{H_{50\%}}$ = **1130** m and $\mathbf{H_{95\%}}$ = **1048** m (**Figure 8**). The average slope ($\mathbf{S_s}$) of the stream was determined between points **A** and **H** by Equation (13):

Table 2. Distribution of the surface area of the Nkoup watershed by altitude range.

Altitude bands (m)	Median altitude (H_i)(m)	Surface area		S_iH_i (km^3)	Cumulated area	
		km^2	%		km^2	%
950-1050	1000	7.2	4.1	7.2	7.2	4.1
1050-1150	1100	93.7	53.9	103.0	100.9	58
1150-1250	1200	46.6	26.8	55.9	147.5	84.8
1250-1350	1300	7.8	4.5	10.1	155.3	89.3
1350-1450	1400	7.6	4.4	10.6	162.9	93.7
1450-1550	1500	6.6	3.8	9.8	169.5	97.5
1550-1650	1600	3.1	1.8	4.9	172.6	99.3
1650-1750	1700	0.9	0.5	1.5	173.5	99.8
1750-1850	1800	0.2	0.1	0.4	173.7	99.9
1850-1950	1900	0.1	0.1	0.2	173.8	100.0
Total		173.8	100	203.7	173.8	100

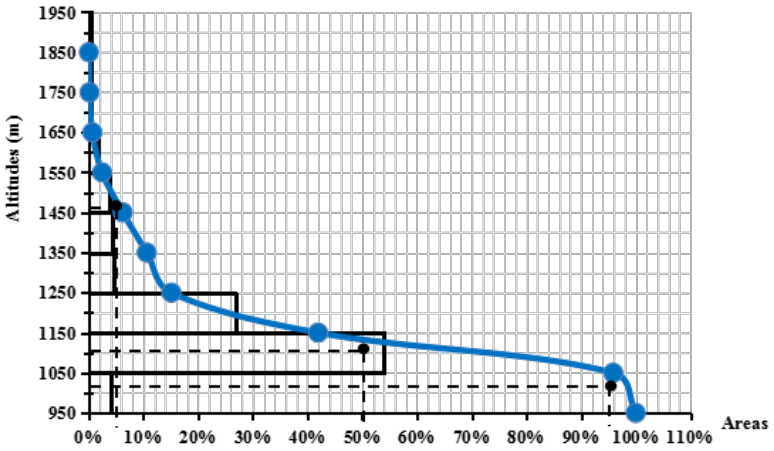

Figure 8. Hypsometric curve of the Nkoup watershed.

$$H_a = \frac{\sum_{i=1}^{n} A_i H_i}{A} \quad (13)$$

with H_i = median altitude of a slice delimited by two consecutive H_a and H_b level curves: $H_i = \frac{Ha + Hb}{2}$. A_i = Partial area of the slice between two consecutive contour lines H_a and H_b; A = Total area of the watershed. The Nkoup watershed has an average altitude H_a = **1726.31 m**.

The relief of the Nkoup watershed is the result of the following products: Pyroclasts, basalts and rhyolites. The Nkoup watershed is characterised by high relief with steep slop resulting from significant volcanic activities.

Stream gradient of the Nkoup River

By subdividing into 14 portions according to the variations in the sinuosity of the main stream, the longitudinal profile of the Nkoup River was produced (**Figure 9**). The average slope of the stream (S_g) was determined between points **A** and **H** of the longitudinal profile by Equation (14):

$$S_g = \frac{\Delta H}{\Delta L} \quad (14)\ [30]$$

with **ΔH** = altitude difference between two chosen points and **ΔL** = distance in meters between the two chosen points.

$$\underline{\text{NA}}: \ S_g = \frac{1212-1045}{|5400-33200|} = 0.006 \text{ or } 0.6\%$$

The maximum flow length of the Nkoup River is L_f = **36.93** km. Its average slope is very low (**0.6%**) over the first 33 kilometers from the source and high (**18%**) at the outlet due to the presence of the Mbatou waterfall. This low slope influences the flow of

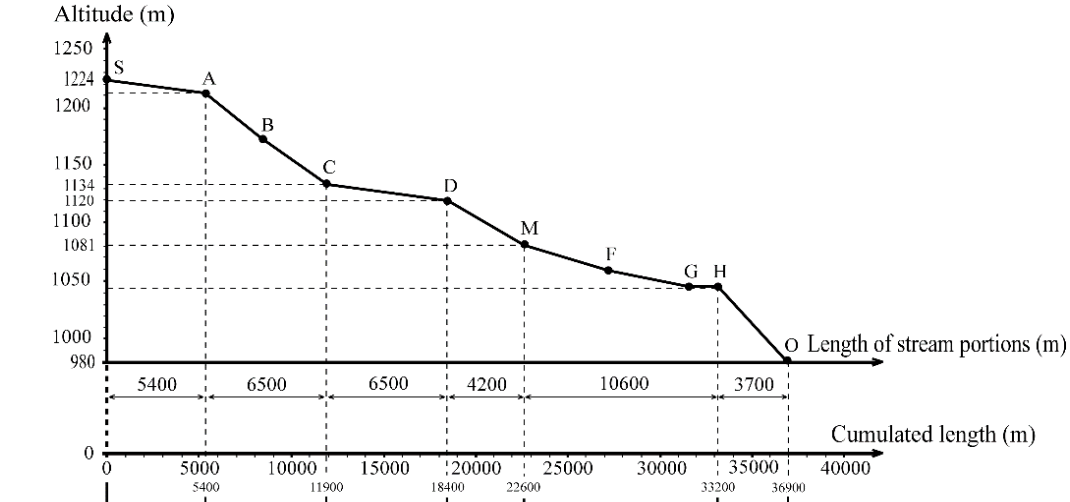

Value	0.002	0.012	0.002	0.009	0.003	0.18
Slope (%)	0.2	1.2	0.2	0.9	0.3	18
Average value	0.006					
Average slope (%)	0.6					

Figure 9. Longitudinal profile of the Nkoup River.

surface water, thus justifying a high sinuosity coefficient (75%).

Channel sinuosity index

The Channel Sinuosity Index (**CSI**) [29] is the relationship between the length of the bird's-eye stream from source to outlet and the actual length of the main stream. It is calculated by Equation (15):

$$\mathbf{CSI = Ld/Lf} \quad (15)$$

with $\mathbf{L_d}$ = length of the bird's-eye stream from source to an outlet (**27.7** km); $\mathbf{L_f}$ = Actual length of the main stream (**36.93** km).

NA: CSI = 27.7/36.9 = 0.75; or **75%**

This high Channel Sinuosity Index CSI = 0.75 is justified by the low slopes observed along the stream.

Gravelius compactness index

The Gravelius Compactness Index or Coefficient of Form (**Icomp**) [30] is determined by Equation (16):

$$\boldsymbol{Icomp} = \frac{\mathbf{0.282\ x\ P}}{\sqrt{\boldsymbol{S}}} \quad (16)$$

P = watershed perimeter (**132.645** km) and **A** = watershed area (**173.7** km^2).

$$\mathbf{NA:}\ \boldsymbol{Icomp} = \frac{\mathbf{0.282\ x\ 132.645}}{\sqrt{\mathbf{173.7}}} = \mathbf{2.8}$$

Equivalent rectangle

The equivalent rectangle is a purely geometric transformation in which the lines parallel to the widths of the rectangle and the outlet are the short side of the rectangle [31]. In a watershed, it is assumed that the flow is almost the same as on a rectangle of the same area under climatic, hypsometric, land cover and drainage density conditions. The dimensions of the equivalent rectangle for the Nkoup watershed are determined as Equations (17) and (18):

- The equivalent rectangle Length:

$$\mathbf{Leq} = \sqrt{\mathbf{A}}\ \boldsymbol{X}\ \left(\frac{\boldsymbol{I_{comp}}}{\mathbf{1.128}}\right)\ \boldsymbol{X}\ \left[\mathbf{1} + \sqrt{\left(\mathbf{1} - \left(\frac{\mathbf{1.128}}{\boldsymbol{I_{comp}}}\right)^{\mathbf{2}}\right)}\right] \quad (17)$$

$$\underline{\boldsymbol{NA}}\mathbf{:\ Leq} = \sqrt{\mathbf{173.7}}\ \boldsymbol{X}\ \left(\frac{\mathbf{2.8}}{\mathbf{1.128}}\right)\ \boldsymbol{X}\ \left[\mathbf{1} + \sqrt{\left(\mathbf{1} - \left(\frac{\mathbf{1.128}}{\mathbf{2.8}}\right)^{\mathbf{2}}\right)}\right] = \mathbf{62.7\ km}$$

- The equivalent rectangle Width:

$$\mathbf{Weq} = \sqrt{\mathbf{A}}\ \boldsymbol{X}\ \left(\frac{\boldsymbol{I_{comp}}}{\mathbf{1.128}}\right)\left[\mathbf{1} - \sqrt{\left(\mathbf{1} - \left(\frac{\mathbf{1.128}}{\boldsymbol{I_{comp}}}\right)^{\mathbf{2}}\right)}\right] \quad (18)$$

or $Weq = \frac{A}{L_{eq}}$ **NA: Weq** $= \sqrt{173.7}\, X \left(\frac{2.8}{1.128}\right)\left[1 - \sqrt{\left(1 - \left(\frac{1.128}{2.8}\right)^2\right)}\right]$

= 2.8 km

Relief Ratio

The Relief Ratio ($\mathbf{R_r}$) of the Nkoup watershed is given by Equation (19) [27]:

$$\mathbf{R_r} = \frac{\Delta_{max}}{Leq} \quad (19)$$

where Δ_{max} = **Hmax –Hmin (**Δ_{max} = *maximum height dif ference*). **Hmin** = Minimum altitude (980 m), **Hmax** = Maximum altitude (1224 m) and **Leq** = Equivalent rectangle length (62.7 km).

$$\underline{\mathbf{NA}}: R_r = \frac{1224-980}{62.7} = 3.89\ \mathbf{m/km}$$

The Relief Ratio $\mathbf{R_r = 3.9}$ shows that the area has low slope that can not create high potential energy for transporting water and sediment down slope [4].

Global slope index

The Dubreuil [32] global slope Index (**Ig**) of the Nkoup watershed is calculated from the hypsometric distribution using Equation (20):

$$\mathbf{Ig} = \frac{D}{L_{eq}} \quad (20)$$

where **D = H5% – H95%** with $\mathbf{H_{5\%}}$ = Altitude having 5% of the watershed above (**1473** m) and $\mathbf{H_{95\%}}$ = Altitude having 95% of the watershed below (**1130** m).

$$\underline{\mathbf{NA}}: \mathbf{Ig} = \frac{1473-1130}{62.7} = 6.78\ \text{m/km}$$

Specific height Difference

The specific height Difference (**Ds**) is given by Equation (21):

$$Ds = \mathbf{Ig}\ \mathbf{x}\ \sqrt{A} \quad (21)$$

With **Ig** = global slope Index and **A** = watershed area. **NA:** $DS = 6.78 \times \sqrt{173.7} = 89.36$ **m**.

Elongation ratio

The elongation ratio (**R**) is defined as the ratio of the diameter of a circle of the same area as the watershed to the maximum watershed length [27]. Its value varies from 0 (highly elongated shape) to 1 (round shape).

$$R = \frac{2}{\pi}\sqrt{\frac{A}{L^2}} \qquad \underline{\mathbf{NA}}: R = \frac{2}{\pi}\sqrt{\frac{173.7}{62.7^2}} = 0.13$$

The elongation ratio R = 0.1 shows that the watershed is a more elongated shape. So the Nkoup river shows the a longer lag time and a low risk of soil erosion and flooding [11,34,35].

Circularity ratio

The Circularity ratio (**Rc**) [33] is the ratio of the watershed area to the area of a circle having the same perimeter as the watershed. It is ranging from 0 to 1 and be calculated as follows:

$$Rc = \frac{4\,\Pi A}{P^2} \qquad \underline{\mathbf{NA}}: \quad Rc = \frac{4*3.14*173.7}{132.6^2} = 0.12$$

The Circularity ratio Rc = 0.1 showing that the Nkoup watershed is elongated in shape and may have lower runoff potential resulting from the presence of highly permeable pyroclastic materials [9].

Drainage texture ratio

Drainage texture ratio (**Rt**) [13] is the ratio between the total length of stream segments of all orders and the perimeter of the watershed. It is expressed by the following formula:

$$Rt = \frac{\mathbf{Li}}{\mathbf{P}}$$

Li = total length of stream segments of all orders; and P = perimeter of the watershed.

$$\mathbf{NA:}\ Rt = \frac{\mathbf{83.376}}{\mathbf{132.6}} = \mathbf{0.63}$$

The texture ratio is classified into four categories < 4 per km coarse, 4-10 per km intermediate, 10-15 per km fine and > 15 per km ultra fine [35]. The Drainage texture ratio **Rt** = 0.6 indicating that the Nkoup watershed falls in coarse category.

3.4 Simplified hydrological balance of the Nkoup watershed

Table 3 presents the average values of the data obtained from the meteorological stations of Foumbot, Kouoptamo, Koutaba and Baïgom.

Table 3 shows that the Nkoup Watershed has a precipitation of 1877.74 mm/year, a Potential Evapotranspiration of 953.42 mm/year, for a Real EvapoTranspiration of 832.31 mm/year. The outlet is located in Batou with coordinates 5°30'31.20"N,

Table 3. The different values of ETP, RFU and ETR.

Month	P (mm)	T (°C)	i	a	λ	ETP (mm)	RFU	ETR (mm)
January	00.60	22.58	09.80	0.503	1.02	79.90	00.00	00.60
February	30.74	23.28	10.26	0.503	0.93	71.55	00.00	30.74
March	113.66	23.52	10.43	0.502	1.03	78.75	34.91	78.75
April	146.26	22.98	10.07	0.503	1.02	78.70	100.00	78.70
May	158.32	22.28	9.60	0.503	1.06	82.48	100.00	82.48
June	210.34	21.34	9.00	0.504	1.03	81.27	100.00	81.27
July	262.12	21.1	8.85	0.504	1.06	83.87	100.00	83.87
August	317.48	21.04	8.81	0.504	1.05	83.15	100.00	83.15
September	318.26	21.12	8.86	0.504	1.01	79.91	100.00	79.91
October	243.56	21.46	9.98	0.503	1.03	77.13	100.00	77.13
November	76.40	22.12	9.50	0.504	0.99	77.40	99.00	76.40
December	00.00	22.34	9.64	0.503	1.02	79.31	19.69	79.31
Total	1877.74	265.16	123.8	6.04	12.25	953.42	853.6	832.31
Average	156.48	22.10	10.32	0.503	01.02	79.45	71.13	69.36

10°37'52.7"E and 980 m.

The runoff of a watershed is a function of the following parameters: The flow rate of its main river taken at the outlet, its area and the time of year (Equation (22)).

$$\mathbf{R} = (\mathbf{Q} \times \mathbf{t})/\mathbf{A} \quad (22)$$

with: **Q** = average annual flow in m^3/s of the Nkoup; t = time in seconds; **A** = Nkoup watershed area in m^2. The flow rate (**Q**) is a function of the speed (**V**) of the current and its flow section (**S**). It is expressed mathematically as follows: **Q** = **VS**. The flow calculation takes into account the following situations: The speed of the current at the surface is greater than the speed of the deeper parts of the stream; The speed of the current in the middle is greater than the speed at the edge of the stream. Thus the value of the flow rate obtained is corrected by a coefficient "**B**" such as **0.6** < **B** < **0.8**; thus the flow rate formula becomes Equation (23):

$$\mathbf{Q} = \mathbf{BVS} \quad (23)$$

The Nkoup River has flow rates that vary according to the seasons (1.0-8.6 m^3/s) for an annual average value of 4.2 m^3/s. For **Q** = 4.2 m^3/s; t = 1 year = 31,536,000 s and A = 173.7 km^2 = 173,770,000 m^2. R = (4.2 × 31,536,000)/173,700,000 = 0.76253 m. **NA: R** = **762.53** mm.

The infiltration is calculated using the following hydrological balance formula (Equation (24)):

$$\mathbf{P} = \mathbf{I} + \mathbf{ETR} + \mathbf{R} \quad (1)$$

$$\rightarrow \mathbf{I} = \mathbf{P} - (\mathbf{ETR} + \mathbf{R}) \quad (24)$$

NA: I = 1877.74 – (832.31 + 762.53)

I = **282.9** mm/year. Hydrologically, the Nkoup Watershed has the following parameters: Total precipitation **P** = **1877.74** mm/year; Total potential evapotranspiration **ETP** = **953.42** mm/year; Real evapotranspiration, **ETR** = **832.31** mm/year, that is 44.3% of precipitation; Runoff **R** = **762.53** mm/year, that is 40.6% of precipitation; Infiltration **I** = **282.9** mm/year, that is 15.1% of precipitation.

The runoff parameters are very important because water resources management decisions depend on the timings of runoff characteristics of a watershed [36]. Rainfall and evapotranspiration are influenced by Mount Mbapit and are unevenly distributed in the watershed (**Figure 4**). The infiltration (15% of precipitation) is partly linked to the very low slope and the permeability of recent basaltic formations in the lower zone which covers around 85% of the watershed (**Figure 2 and 7 and 8**).

3.5 Groundwater flow

The piezometric levels vary according to the seasons. They increase to 2 or 7 m depending on the work. These variations have very little influence on the direction of groundwater flow. The highest piezometries are observed in the Northern part (Koutaba) while the lowest piezometries are found in the South

of the watershed. The underground flow follows a North-South direction (**Figure 10**).

Groundwater recharge is very rapid with an increase in the piezometric level to 2 to 7 m in September. The direction of the groundwater flow is North-South and is very weakly influenced by seasonal variations in the piezometric level. The high piezometries are observed in the high zone and the shallow piezometries are located in the lower zone.

4. Conclusions

The Nkoup watershed has five geological formations: The basement rock (migmatitic gneiss), rhyolites, plateau basalt, recent basalt and pyroclasts, which cover an area of 173.7 km^2. These formations are fractured in two major directions (N20°-50°E and N50°-90°W). The Nkoup, 36.9 km long is the main river. It takes its source at 1224 m altitude in Didango and flows along a meandering stream with an average slope of 0.6%, up to 980 m altitude at its outlet at Mbatou. Its average annual flow rate is 4.2 m^3/s and a particle that leaves the main source will take 4 hours 57 minutes to reach the outlet. With a total annual rainfall of 1877.74 mm, infiltration represents 15.1%, against 44.3% and 40.6% respectively for the ETR and the Runoff. According to the following parameters: Axial Length Lax = 25.8 km, Axial Width Wax = 11.1 km, Perimeter P = 132.6 km, Area A = 173.7 km^2, Average altitude Ha = 1726.3 m, Compactness Index Icomp = 2.8, Relief ratio Rr = 3.9 m/km, Circularity ratio Rc = 0.1, Elongation ratio R = 0.1, Drainage texture ratio Rt = 0.6, Drainage density Dd = 0.5 km/km^2. Stream Frequency Fs = 0.4, Channel Sinuosity Index CSI = 0.8, Stream gradient Sg = 0.6 and global slope Index Ig = 6.8 m/km. The specific height Difference Ds = 89.4 m; the Nkoup River shows a longer lag time and low risk of soil erosion and flooding. The relief of Nkoup watershed is characterised by moderate slop resulting from significant volcanic activities. That relief is the result of the following products: Pyroclasts, basalts and rhyolites. The watershed is more elongated in shape and may have lower runoff potential resulting from the presence of highly permeable pyroclastic materials. The Nkoup watershed has an aquifer potential that should be identified through the distribution of water structures and in-depth studies of each geological formation.

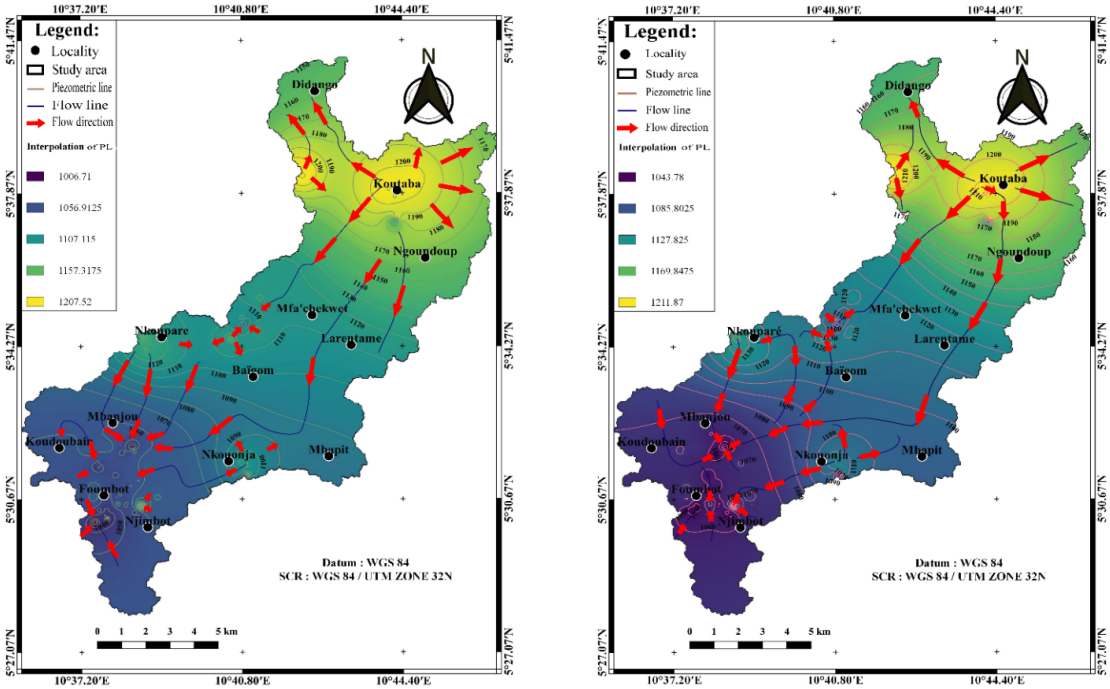

(a) (b)

Figure 10. Piezometry and direction of groundwater flow in the Nkoup watershed (a) April and (b) September.

Author Contributions

Paul Bertrand TSOPKENG: Choice of theme and study area; constitution of the work team; direction of work; collection, processing and synthesis of data; consolidation of the final document; financing of all works. Josiane FEUGUE KENFACK: Collection and processing of climate data, field assistance. David Guimolaire NKOUATHIO: Advice and guidance on the choice of theme and site. Charles Antoine BASSEKA: Advice and assistance for data processing. Leonel KOUDJOU TSAGUE: Assistance for the production of certain thematic maps.

Conflict of Interest

The authors declare that they have no competing interests.

References

[1] TITA M. A., 2008. Warter pollution of the Nkoup river system and its environmental impact on Foumbot town (Western Cameroun) Thèse de Doctorat ph/D Univ de Yaoundé I. 212p.

[2] Prabhakar, A.K., Singh, K.K., Lohani, A.K., et al., 2019. Study of Champua watershed for management of resources by using morphometric analysis and satellite imagery. Applied Water Science. 9, 1-16.
DOI: https://doi.org/10.1007/s13201-019-1003

[3] Chopra, R., Dhiman, R.D., Sharma, P.K., 2005. Morphometric analysis of sub-watersheds in Gurdaspur district, Punjab using remote sensing and GIS techniques. Journal of the Indian Society of Remote Sensing. 33, 531-539.

[4] Gopinath, G., Nair, A.G., Ambili, G.K., et al., 2016. Watershed prioritization based on morphometric analysis coupled with multi criteria decision making. Arabian Journal of Geosciences. 9, 1-17.

[5] Bezinska, G.V., Stoyanov, K.S., 2019. Modelling and hydro-morphometric analysis of sub-watershed. A case study of Mesta river southwestern Bulgaria. European Journal of Geography. 10(2), 77-88.

[6] Hamdan, A.M., 2020. Hydro-morphometric analysis using geospatial technology: A case study of Wadi Gabgaba and Wadi Allaqi watersheds, southern Egypt-northern Sudan. Journal of Asian Scientific Research. 10(3), 190-212.
DOI: https://doi.org/10.18488/journal.2.2020.103.190.212

[7] Garde, R.J., 2006. River morphology. New Age International (Pvt) Ltd.: New Delhi.

[8] Iqbal, M., Sajjad, H., Bhat, F.A., 2013. Morphometric analysis of Shaliganga sub catchment, Kashmir Valley, India using geographical information system. International Journal of Engineering Trends and Technology. 4(1), 10-21.

[9] Singh, P., Thakur, J.K., Singh, U.C., 2013. Morphometric analysis of Morar River Basin, Madhya Pradesh, India, using remote sensing and GIS techniques. Environmental Earth Sciences. 68(7), 1967-1977.

[10] Bloomfield, J.P., Bricker, S.H., Newell, A.J., 2011. Some relationships between lithology, basin form and hydrology: A case study from the Thames basin, UK. Hydrological Processes. 25(16), 2518-2530.

[11] Soni, S., 2016. Assessment of morphometric characteristics of Chakrar watershed in Madhya Pradesh India using geospatial technique. Applied Water Science. 7, 2089-2102.

[12] Chandrashekar, H., Lokesh, K.V., Sameena, M., et al., 2015. GIS—based morphometric analysis of two reservoir catchments of Arkavati River, Ramanagaram District, Karnataka. Aquatic Procedia. 4, 1345-1353.

[13] Horton, R.E., 1945. Erosional development of streams and their drainage basins; hydrophysical approach to quantitative morphology. Geological Society of America Bulletin. 56(3), 275-370.

[14] Evans, I.S., 1972. General geomorphometry, derivatives of altitude, and descriptive statistics. Spatial analysis in geomorphology. Harper and Row: New York. pp. 17-90.

[15] Altaf, F., Meraj, G., Romshoo, S.A., 2013. Morphometric analysis to infer hydrological behaviour of Lidder watershed, Western Himalaya, India. Geography Journal. 178021.

[16] Wandji, P., Wotchoko, P., Bardintzeff, J.M., et al., 2010. Late tertiary and quaternary alkaline volcanism in the western Noun Plain (Cameroon Volcanic Line): New K-Ar ages, petrology and isotope data. Bulgarian Academy of Sciences. 48, 67-94.

[17] Jenson, S.K., 1991. Applications of hydrologic information automatically extracted from digital elevation models. Hydrological Processes. 5(1), 31-44.

[18] Wise, S., 2000. Assessing the quality for hydrological applications of digital elevation models derived from contours. Hydrological Processes. 14(11-12), 1909-1929.

[19] Patel, A., Katiyar, S.K., Prasad, V., 2016. Performances evaluation of different open source DEM using Differential Global Positioning System (DGPS). The Egyptian Journal of Remote Sensing and Space Science. 19(1), 7-16.

[20] Bastawesy, M.E., Gabr, S., White, K., 2013. Hydrology and geomorphology of the Upper White Nile Lakes and their relevance for water resources management in the Nile basin. Hydrological Processes. 27(2), 196-205.

[21] Li, J., Wong, D.W., 2010. Effects of DEM sources on hydrologic applications. Computers, Environment and Urban Systems. 34(3), 251-261.

[22] Moore, I.D., Grayson, R.B., Ladson, A.R., 1991. Digital terrain modelling: A review of hydrological, geomorphological, and biological applications. Hydrological Processes. 5(1), 3-30.

[23] Thornthwaite, C.W., 1954. The measurement of potential evapotranspiration. JM Mather, Seabrook: New Jersey. pp. 222.

[24] Olivry, J.C., 1986. Fleuves et rivières du Cameroun (French) [Rivers and rivers of Cameroon]. Collection "Hydrological monographs. ORSTOM" N°9. Paris. P.781. (LVC) [PhD thesis]. Yaoundé: Université de Yaoundé I. p. 57.

[25] Gaussen, H., Bagnouls, S., 1957. Les Climats biologiques et leur signification (French) [Biological climates and their significance]. Ann. Geol. XXVI. 193220 Ekodeck G.E (1984). 6(355), 194.

[26] De Martonne, E., 1926. Une nouvelle fonction climatique: l'Indice d'Aridité (French) [A new climatic function: The Aridity Index]. La météorologie. 449-458.

[27] Schumm, S.A., 1956. Evolution of drainage systems and slopes in badlands at Perth Amboy, New Jersey. Geological Society of America Bulletin. 67(5), 597-646.

[28] Rekha, B.V., George, A.V., Rita, M., 2011. Morphometric analysis and micro-watershed prioritization of Peruvanthanam sub-watershed, the Manimala River Basin, Kerala, South India. Environmental Research, Engineering and Management. 57(3), 6-14.

[29] Leopold, L.B., Wolman, M.G., Miller, J.P., 1964. Fluvial processes in geomorphology. WH Freeman and Co.: San Francisco.

[30] Gravelius, H., 1914. Grundrifi der gesamten gewcisserkunde (German) [Basic plan of the entire Gewisserkunde]. Band I: Flufikunde (Compendium of Hydrology. vol. I., Rivers in German). Goschen: Berlin.

[31] Hack, J.T., 1957. Studies of longitudinal stream profiles in Virginia and Maryland. US Government Printing Office: Washington, DC.

[32] Dubreuil, P., 1974. Introduction à l'analyse hydrologique (French) [Introduction to hydrological analysis]. Masson-ORSTOM: Paris. pp. 216.

[33] Miller, V.C., 1953. Quantitative geomorphic study of drainage basin characteristics in the Clinch Mountain area, Virginia and Tennessee. Technical Report. Department of Geology Columbia University: New York. pp. 389-402.

[34] Strahler, A.N., 1964. Quantitative geomorphology of drainage basin and channel networks. Handbook of applied hydrology. McGraw Hill: New York. pp. 439-476.

[35] Choudhari, P.P., Nigam, G.K., Singh, S.K., et al., 2018. Morphometric based prioritization of watershed for groundwater potential of Mula river basin, Maharashtra, India. Geology, Ecology, and Landscapes. 2(4), 256-267.

[36] Dinpashoh, Y., Singh, V.P., Biazar, S.M., et al., 2019. Impact of climate change on streamflow timing (case study: Guilan Province). Theoretical and Applied Climatology. 138, 65-76.

Appendix

Appendix 1. Temperature in °C.

Month / Year	Jan.	Feb.	March	April	May	June	July	August	September	October	November	December	Average
2016	23	23.4	23.6	23.1	22.4	21.4	21.1	21.2	21.3	21.6	22.3	22.5	22.24
2017	22.8	23.4	23.6	23	22.3	21.3	20.9	21	21.1	21.5	22.2	22.4	22.13
2018	22.5	23.1	23.3	22.8	22.1	21.2	20.8	20.9	20.8	21.2	21.9	22	21.88
2019	22.8	23.2	23.5	22.9	22.2	21.3	21.2	21.1	21.2	21.6	22.2	22.5	22.14
2020	21.8	23.3	23.6	23.1	22.4	21.5	21.5	21	21.2	21.4	22	22.3	22.09
Average	22.58	23.28	23.52	22.98	22.28	21.34	21.1	21.04	21.12	21.46	22.12	22.34	22.1

Appendix 2. Precipitation (rainfall) in mm.

Month / Year	Jan.	Feb.	March	April	May	June	July	August	September	October	November	December	Average
2016	0	30.2	127.8	204.8	160.7	123.9	253.7	392.1	284	312.6	163.3	0	171.09
2017	0	6.5	90.3	141.1	137.1	144	266.8	216.1	281.6	279	62.9	0	135.45
2018	0	0	106.5	74.8	149.5	318.1	271.4	266.3	285.3	198.5	33.3	0	141.98
2019	3	0	50.4	187.6	212.2	199.3	266.5	344.4	450.7	227	71.2	0	167.69
2020	0	117	193.3	123	132.1	266.4	252.2	368.5	289.7	200.7	51.3	0	166.18
Average	0.6	30.74	113.66	146.26	158.32	210.34	262.12	317.48	318.26	243.56	76.4	0	156.48

Appendix 3. Altitudes of points and length of different portions of the Nkoup stream.

Points	S	A	B	C	D	M	F	G	H	O
Altitudes (m)	1224	1212	1172	1134	1120	1081	1059	1046	1045	980
Cumulated lengths mesured in the field (km)	0	5.4	8.4	11.9	18.4	22.6	27.2	31.5	33.2	36.9
Portions of the Nkoup stream	SA	AB	BC	CD	DM	MF	FG	GH	HO	
Length mesured on the map (cm)	9.8	5.4	6.4	11.7	7.6	8.3	7.7	3.2	6.7	
Length mesured in the field (km)	5.4	3.0	3.5	6.5	4.2	4.6	4.3	1.7	3.7	

BILINGUAL PUBLISHING GROUP

Advances in Geological and Geotechnical Engineering Research

https://ojs.bilpublishing.com/index.php/agger

ARTICLE

On the Possible Cometary Nature of the Uchur Cosmic Body (Fall 3.08. 1993)

***Tselmovich Vladimir A.*[1*], *Amelin Ivan I.*[2], *Gusiakov Viacheslav K.*[2], *Kirillov Vadim E.*[3], *Kurazhkovskii Alexander Yu.*[1]**

[1] *Geophysical Observatory "Borok", Branch of the Schmidt Institute of Physics of the Earth, Russian Academy of Sciences (GO "Borok" IPE RAS), Yaroslavl region, Borok, 142, 152742, Russia*

[2] *Institute of Computational Mathematics and Mathematical Geophysics of the Russian Academy of Sciences (IVMiMG SO RAN), 6 Ak. Lavrentieva Ave., Novosibirsk, 630090, Russia*

[3] *Institute of Tectonics and Geophysics named after Yu. Kosygin, Russian Academy of Sciences, ul. Kim Yu Chen 65, Khabarovsk, 680000, Russia*

ABSTRACT

An expeditionary study of the area of the alleged impact event that occurred on 3.08.1993 in the area of the Lower Konkuli River (southeast of the Aldan Highlands, Lurikan Range, Russia) was carried out. According to the materials of remote sensing, the places of collision with the earth of a cosmic body are determined. In the area of the impact of the shock wave on the Earth's surface, peat samples were selected, the micro probe analysis of which showed the presence of a cosmogenic substance in concentrations 6-8 times higher than the background. Silicate and magnetite micro spheres, native iron, moissanite, and carbon micro tubes coated with a film consisting of pure nickel were found. Of particular interest were the findings of specific Ni film micro structures that allow us to make an assumption about the cometary nature of the Uchur cosmic body. Most researchers associate the observed flights of fireballs with the subsequent fall of meteorites. Researchers are trying to find the massive body of the fallen space body. However, often, even after many years of searching, a massive cosmic body cannot be found. This happened when studying the site of the fall of the Tunguska cosmic body. In this case, it remains to be assumed that the cosmic body contained microscopic dust particles. The structure and composition of such particles can only be studied using microscopic research methods. When studying the Uchur cosmic body, the authors concluded that it could be of a cometary nature due to the findings of specific particles—thin films of pure nickel on the surface of plant remains of terrestrial origin. This hypothesis arose from the recent discovery of atomic nickel vapors in comets.

Keywords: Uchur cosmic body; Impact event; Cosmogenic matter; Microtubes; Nickel films; Microstructures; Cometary nature

*CORRESPONDING AUTHOR:

Tselmovich Vladimir A., Geophysical Observatory "Borok", Branch of the Schmidt Institute of Physics of the Earth, Russian Academy of Sciences, Yaroslavl region, p. Borok, 142, 152742, Russia; Email: tselm@mail.ru

ARTICLE INFO

Received: 25 April 2023 | Revised: 19 June 2023 | Accepted: 30 June 2023 | Published Online: 13 July 2023

DOI: https://doi.org/10.30564/agger.v5i3.5705

CITATION

Tselmovich, V.A., Amelin, I.I., Gusiakov, V.K., et al., 2023. On the Possible Cometary Nature of the Uchur Cosmic Body (Fall 3.08. 1993). Advances in Geological and Geotechnical Engineering Research. 5(3): 16-24. DOI: https://doi.org/10.30564/agger.v5i3.5705

COPYRIGHT

Copyright © 2023 by the author(s). Published by Bilingual Publishing Group. This is an open access article under the Creative Commons Attribution-NonCommercial 4.0 International (CC BY-NC 4.0) License. (https://creativecommons.org/licenses/by-nc/4.0/).

1. Introduction

Among the various natural disasters to which modern civilization is subject, a special place is occupied by the dangers associated with the fall of cosmic bodies to the Earth. On the one hand, there is no evidence in the historical and archaeological sciences that any cosmic processes had an impact on the course of the historical process. On the other hand, geologists and geophysicists involved in this topic point to the existence of more than a dozen impact craters that formed on the Earth's surface during the same period and too obvious traces of major climatic anomalies and environmental downturns that have no established connection with Earth processes [1]. Thus, in previous studies [2,3], traces of a catastrophe of presumably impact origin 5000-5500 years ago were found at different objects.

The largest space catastrophe of the 20th century occurred in Russia and is known to the whole world under the name of the Tunguska cosmic body, although no large material traces of the cosmic body that exploded over the Siberian taiga on June 30, 1908 have yet been found [4]. Another major event that also happened on the territory of Russia was the fall of the Sikhote-Alin meteorite on February 12, 1947, which affected an area of about 48 square km, where about 150 impact craters ranging in size from 1 to 27 meters were later identified [5]. In total, about a dozen large fireball explosions and almost 200 falls of cosmic bodies weighing more than 1 kg on Earth were recorded over the 20th century [6]. The last well-known event of this kind was the fall of the Chelyabinsk meteorite on February 15, 2013. The monograph *Methods and means of information-analytical assessment of asteroid and comet hazard* [7] summarizes information about this event and analyzes the actions of the Ministry of Emergency Situations to eliminate its consequences. The book concludes that this event gave rise to an emergency at the federal level, which required the concentration of significant resources to eliminate its consequences. The Chelyabinsk event initiated the inclusion of space (asteroid-comet) hazards in the official list of natural hazards that need forecasting and planning for counteraction, protection and elimination of consequences.

The issues of practical implementation of such planning require, first of all, adequate risk assessments arising from space threats. In turn, the basis for such estimates are estimates of the probability of falling cosmic bodies of one size or another to the Earth. It is most important to obtain such estimates for the current stage of geological history, i.e. for the Holocene (the last 10-12 thousand years). The existing estimates, which are used by the community of astronomers and astrophysicists, are based mainly on observations of comets and asteroids, as well as analysis of craters on the Moon and other bodies of the Solar System [8,9]. However, the most reliable data on the probabilities of cosmic bodies falling to the Earth can be obtained from an analysis of the actual statistics of such falls, provided that ground tracks are reliably recorded and there is reliable evidence of their connection with cosmic bodies [10].

Practical adherence to this recommendation encounters, first of all, the scarcity of information about such falls even at the present stage (the last 50-100 years). Falls of cosmic bodies capable of leaving traces on the earth's surface occur quite rarely, while more than two-thirds of this surface is covered with water. Despite the extensive development of observational astronomy, means of communication and mass communications, far from all cases of falls and air explosions, even over land, become known to scientists and specialists. Such a fall includes the Uchur cosmic body, which fell in a remote area, in the Khabarovsk Territory of Russia. The nature of this fall is still unknown, and such cases are known in history. Suffice it to recall that the fact of the Tunguska explosion became known to the scientific community almost 20 years after the event itself [4]. The introduction into scientific circulation of each potentially dangerous case of the interaction of cosmic bodies with the Earth is extremely important. It requires careful and comprehensive study, since it changes (always increasing) the estimates of the probability of cosmic bodies falling to the Earth at the present stage of its geological history. Awareness

of the reality of space hazards requires the development of a system of measures to protect against them and reduce the consequences, based, among other things, on obtaining reliable estimates of the expected frequency of falls [11].

It should be noted that the least studied are the collisions of the earth with objects like the "Tunguska cosmic body". Such space objects can have a very significant impact on regional ecosystems. At the same time, there are still no convincing conclusions about their nature, since it is extremely difficult to obtain data on their mineralogical composition and even state of aggregation. Progress in their research can be made possible by direct fixation and research of the fall of such objects on the earth's surface. An example of such an event, witnessed by one of the authors of this article (V.E. Kirillov), is an air explosion and a possible collision with the Earth of a rather large cosmic body that occurred in the evening between 21 and 22 hours local time (10 and 11 hours UTC) 3 August 1993 in the basin of the river. Lower Konkuli (Aldan Highlands, Lurikan Ridge). The present work is devoted to the study of such an event. The group of geologists working in the river valley, which he headed, left the area of the event a few days before it. During the event itself, the detachment was located 15-20 km southeast of the epicenter and was shielded from the effects of the explosion by the Lurikan ridge with altitudes up to 1800 m. In his book of memoirs, V.E. Kirillov writes: "Suddenly, the soil shook violently; then two fading shocks followed, accompanied by a distant rumble to the north" [12]. According to sensations, the intensity of the first most powerful shock was about 3 points. Sound phenomena in the form of a fading rumble lasting 4-5 seconds followed a few seconds after the seismic shocks.

After 2-3 days, the geologists again found themselves in the Lower Konkuli valley. The age-old forest was so disfigured, as if an atomic bomb had exploded here. Huge trees were "cut down" either at the base or in the middle part, or sticking out in the form of whips without branches. A high barricade of chopped, chipped and broken trees with sharp broken branches sticking out in all directions was formed below. The height of the barricades from the shafts in the zone of severe destruction reached 4 m. Later, even the heavy equipment of the Amur artel explorers could not overcome these barricades. Wade through such rubble, four hundred meters wide, was a real torment. The length of the ellipse of destruction was about one and a half kilometers; at least that follows from route observations. In one place we came across a deer, littered with trunks and already gnawed by a bear. Along the periphery of the ellipse of destruction for several kilometers in the area, some of the trees were uprooted and lay with their tops in one direction—to the southwest [12].

As shown by the results of modeling the damaging effects of cosmic bodies with a diameter in the range of 10-50 m and the study of the impact sites of large meteorites (Tunguska, Chelyabinsk, Sikhote-Alin, etc.), in such cases, the bulk (95.0-99.9%) of a space body entering the Earth's atmosphere is destroyed when moving in the upper layers of the atmosphere due to the ablation process. The mass reaching the lower dense layers of the atmosphere, as a rule, breaks up into fragments ranging in size from a few meters, which fall to the Earth's surface, forming impact craters, to micro particles tens to hundreds of micrometers in size, which form a dust trail that falls along the fall trajectory. At the same time, the dust component contains magnetite micro spheres [13], which are formed in large quantities as a result of ablation, native iron, and, in a smaller amount, nickel (the mechanism of their formation is considered [14]. Therefore, the areas of the fallout of the dust component of a large meteorite turn out to be very large in area and can many times exceed the scattering ellipse of individual specimens of visible size (1-2 mm or more). For example, the total area of scattering of fragments of the Sikhote-Alin meteorite was an ellipse 10 × 2 km in size [15], which is an order of magnitude larger than the size of the crater field with the area of damaged forest (about 1 km^2) and the area of the fallout of visible fragments (about 2.5 km^2).

Micron-sized nickel particles found in the snow cover near the flight path several tens of kilometers

from the place of the alleged fall still remain the only material evidence of the fall of the Vitim fireball in 2002 [16]. Magnetite and silicate micro spheres are evidence of the fall of the Tunguska cosmic body in 1908 [13].

Thus, in conditions of inaccessibility of the study area, taking into account the limited time and small size of the research group, the most effective is the search for indicator micro particles in the surface layers of the soil [14]. It is also important that such a search in the field does not require expensive and heavy equipment (deep metal detectors, georadar, etc.). Cosmic particles are especially effectively accumulated and stored in peat deposits, so the main goal of the expeditionary work was to take surface samples of peat in the area of the supposed fall of the Uchur cosmic body (UCB). Subsequently, the samples were studied at the Geophysical Observatory Borok, Branch of the Schmidt Institute of Physics of the Earth, Russian Academy of Sciences, using a technique combining the petromagnetic and micro probe methods with micro mineralogical analysis.

2. Materials and methods

Investigation of the impact area of a meteor explosion. The expedition survey of the impact area of the UCB was performed twice, in July-August 2016 and in August 2017. The detachments were led by an employee of the IVMiMG SB RAS, Ph.D. Amelin I.I. (IVMiMG SB RAS), the detachments included Amelin I.V. (geologist, artel of prospectors "Golden Pole") and Tynda L.B. (a chemical engineer from Moscow). During the first trip, the group examined the areas to the north and northwest of it and took samples of peat. The length of the routes in the area of the fall of the UCB (p. Lower Konkuli, Unga-Bereyakan, Ayakachan, Synnyar) was 25 km. The list of objects inspected in 2016 is presented in **Table 1** and **Figure 1**.

The second expedition carried out in August 2017 allowed us to increase the area of the studied area, reach the area of forest fallout and slope stability violations, as well as to select additional peat samples.

Using medium-resolution satellite images of the Sentinel-2 spacecraft and the Landsat-8 spacecraft (10 m/pixel and 20 m/pixel, respectively, [lv.eosda.com]), a search was carried out for signs of modern changes in forest vegetation and relief in the upper reaches of the Lower Konkuli River. The most extensive violation of the forest cover was found near the mouth of the stream. Using the revealed violations of the continuity of forest vegetation under the influence of external factors and assuming that the genesis of this area is due to the collision of fragments of the UCB with the Earth, we will call it the cosmogenic impact area. This area has a total area of about 4-5 sq. km and is located in the valley of the Lower Konkuli, between the Vershinny stream and the channel of the river Lower Konkuli. It consists of 6 fragments, between which there are free-standing trees, as well as areas of instability on the left slope of the valley of the river Lower Konkuli. The area of the fragments of the dump is 0.5-1.5 hectares. Under the snow cover, the outlines of fallen tree trunks with a diameter of at least 50 cm are visible. The forest area in the valley of the Lower Konkuli River is represented by trees 25-30 m high and 0.6-1 m in diameter at the base of the trunk (spruce, larch, poplar). The mosaic of forest fallout in the valley of the river Lower Konkuli at the Vershinny stream indicates the fragmentation of the cosmic body before the collision with the Earth.

3. Results

To search for micro particles that were part of the UCB and a possible ablative trace, an analysis of the surface layers of peat in the area of the intended impact was carried out. The micro mineralogical analysis was carried out using a scanning electron microscope "Tescan Vega II" with a prefix for energy dispersion analysis. To determine the background concentration of cosmic matter in the region, the study of the surface layer of peat outside the dust trail of the expected impact event was carried out. The sampling site is the valley of the Aldan River 1.5 km east of the village Chagda, a riding swamp (**Figure 1**, **Table 2**). The upper 15 cm of the sample was analyzed.

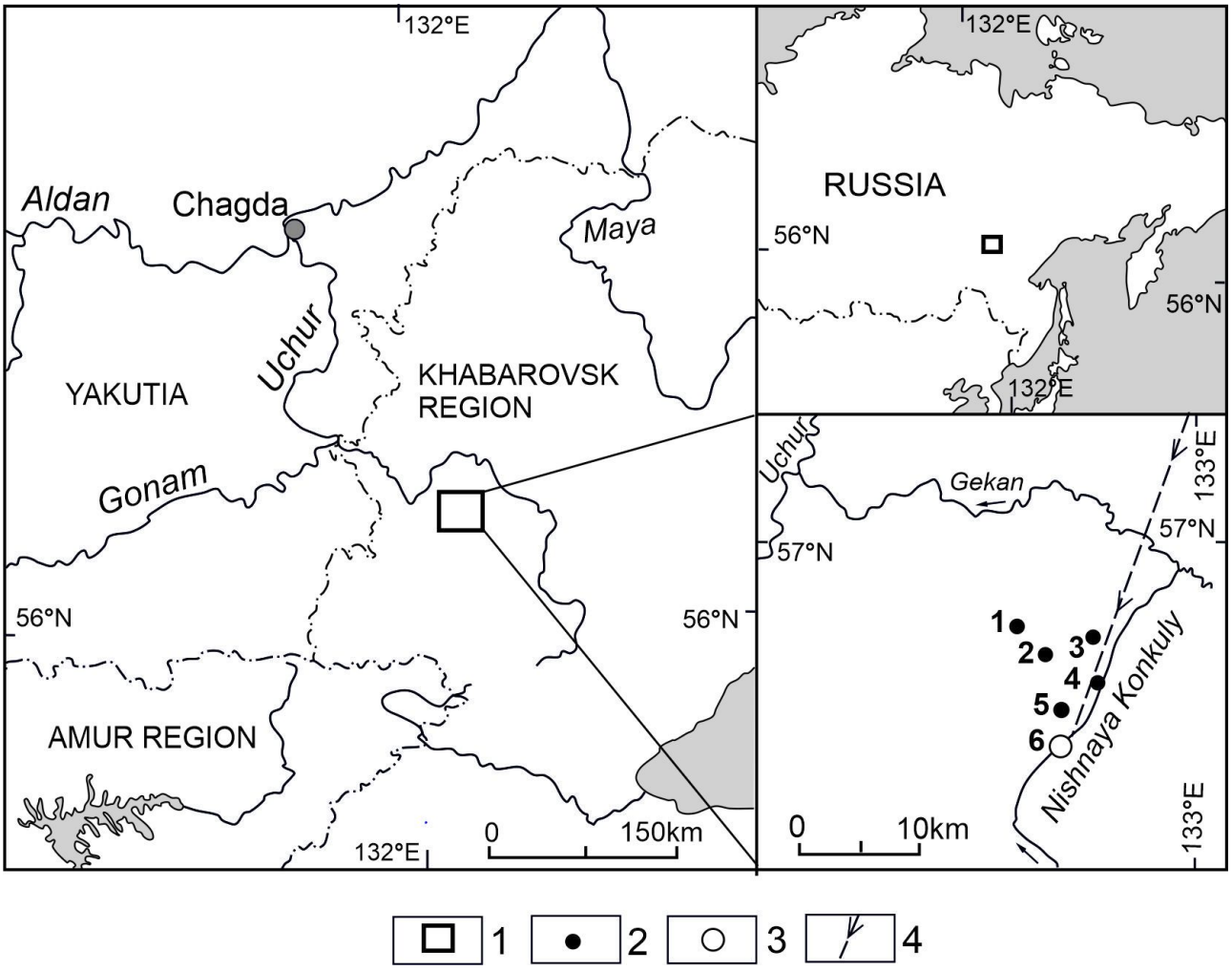

Figure 1. Position of the Uchur cosmic body impact site on the map of Russia and the Far East region and the research site in the Lower Konkuli river basin.

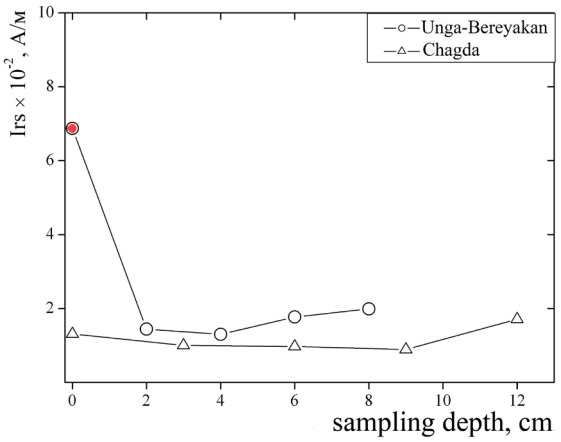

Figure 2. Dependence of saturation remanence (Irs, A/m) on sampling depth, cm.

To search for peat samples most enriched with mineral (in this case cosmogenic) matter, we measured their residual saturation magnetization of the Irs. This parameter is determined by the presence and number of "large" (more than 0.1 microns) mineral particles with residual magnetization. The size of the separated and studied particles was 1-20 microns.

The results of the Irs measurements of the studied samples are shown in **Figure 2**. It can be seen that the Irs of the surface layer of peat from the fall area of the UCB significantly exceeds the residual saturation magnetization of the underlying layers (7×10^{-2} A/m versus 1.5-2 $\times10^{-2}$ A/m) both from the fall area and the control sample of the Chagda (by 600-700%!). The assessment of the depth of the "catastrophic layer" with UCB particles in peat was carried out based on the fact that the expected impact event occurred in 1993. The rate of peat formation in this area (middle taiga) approximately coincides with the area of the Tunguska event, for which this value

is 0.5 mm/year [17]. The upper 10 cm of the peat part is quite sufficient for analysis (23 years have passed from the moment of the expedition work to the expected impact event, that is, a "catastrophic layer" can be expected at a depth of 1.2-1.3 cm), which is confirmed by the results of the Irs study shown in **Figure 2**.

In the second stage, the layers with the highest Irs of the series and background samples were subjected to micro probe analysis to determine the morphology and chemical composition of micro particles [14]. The micro mineralogical analysis was carried out using a scanning electron microscope "Tescan Vega II" with an EDS attachment. A micro probe study of the particles of the surface layer of the sample from the area of the fall of the UCB ("catastrophic" layer) showed that its distinctive feature is the presence of structures in it that could arise when hot UCB particles collide with organic material (peat). Structures of this shape with no film have been found. (**Figures 3a,b,c**). Inside each structure, there is a charred biogenic fragment. The energy dispersive spectrum (**Figure 3d**) of the film shows that it consists of pure nickel (100% Ni).

1) The site of the fall of the UCB on the map; 2) research sites; 3) possible place of fall of fragments of the UCB; 4) the direction of movement of the UCB.

Comments for research sites: 1) felling of the forest with a pronounced general direction of falling trunks; 2) "burn" of elfin and soil; 3) depressions in the upper reaches of the Unga-Bereyakan; 4) base of the exploration team of the Amur artel, 5) "fresh" signs of the impact of the shock wave on the boulders of the slope; 6) the alleged place of the fall of the UCB.

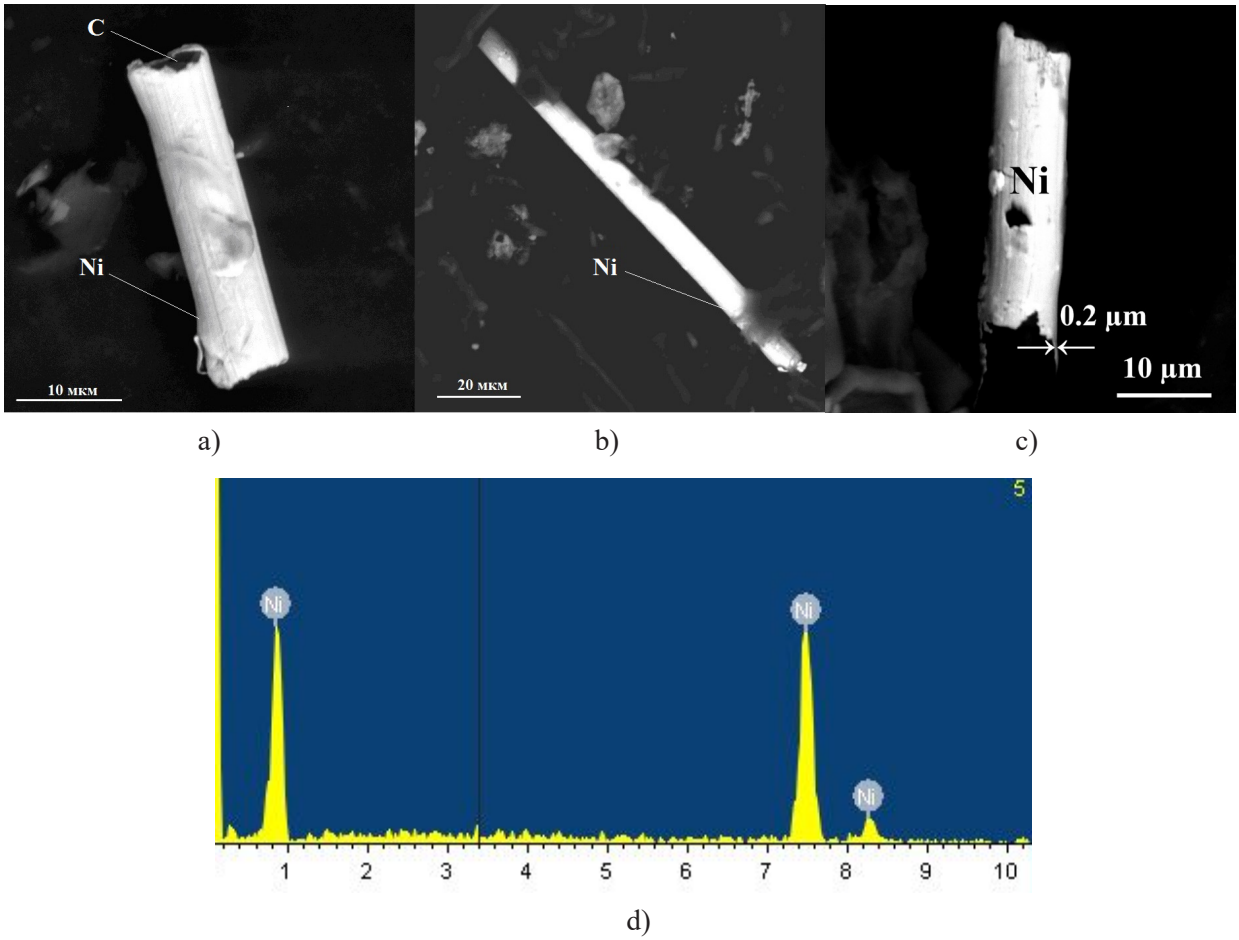

Figure 3. Microparticles from the site of the UCB fall: a) Ni tube (film) 0.5 × 6 × 35 microns with biogenic carbon residue inside; b) Ni tube (film) 0.5 × 8 ×100 microns; c) Ni tube (film) 0.2 × 6 × 40 microns; d) The energy dispersive spectrum of the film shows that it consists of pure nickel.

Table 1. Coordinates, dimensions and location of objects in the area of the impact of the UCB found during search routes and remote sensing decryption.

The name of the object	Coordinates of the center of the structure, northern latitude, eastern longitude	Absolute height, m	Area, hectare	Distance from the fall of the forest (1 in Figure 1), km
1. The fallout of the forest with the general e.g. trunks	56.93854° 132.75706°	900-1000	20-30	10-11
2. Falling out of the forest with chaotic e.g. trunks on the Ayakachan River	56.95211° 132.85342°	800-900	100-200	9-10
3. Probable "burn" of the elfin and soil	56.91480° 132.81825°	1050	1-2	7.5
4. Traces of movement of boulders on the slope (chipped outer surface)	56.86249° 132.85127°	950-1100	0.5-1	1.7
5. Epicenter of severe destruction (fallen forest)	56.84773° 132.84257°	860-870	3-4	-

Table 2. Characteristics of the selected peat samples.

Location of the selection coordinates	Coordinates northern latitude, Eastern longitude; absolute height, m	Geometric dimensions (L-W-H), mm	Distance from the intended epicenter, km
Unga-Bereyakan	56.92579° 132.87410°; 850	150 × 60 × 280	9
Chagda	58.73823° 130.64098°; 197	150 × 200 × 300	248

4. Discussion

A key finding in the study of UCB was the detection of thin films (0.1-0.2 microns thick) of metallic nickel and iron on the surface of terrestrial objects—plant residues. It was impossible to explain the formation of such films by terrestrial processes. However, on 31.08.2019, an interstellar comet passing through the Solar System (2I/Borisov) was discovered. Analyzing the observations of comets of the Solar System and the interstellar comet 2I/Borisov, obtained with a Very Large Telescope (VLT drive). At the European Southern Observatory (ESO), astronomers discovered the presence of nickel and iron in their atmospheres, even in those that were far from the Sun.

This was the first detection of heavy metals, usually associated with hot environments, in the gas shells of cold ice wanderers. "It was a big surprise to find iron and nickel atoms in the atmospheres of all comets that we have observed over the past two decades—and there were about twenty of them," notes Jean Manfroid from the University of Liege (Belgium) [18]. At temperatures exceeding 700 °K, comets also emit metallic vapors, which are formed as a result of the sublimation of metal-rich dust particles. The authors reported spectroscopic observations of atomic Ni vapors in the cold comet 2I/Borisov [19].

5. Conclusions

Usually, researchers in search of traces of impact events focused on the search for massive objects. However, no massive object was found during the study of the UCB. Specific microstructures were found in the form of thin films of pure nickel. Under terrestrial conditions, the formation of such films is impossible. A possible mechanism for the formation of thin nickel films has become clear due to the recent discovery of atomic nickel vapor in cometary atmospheres [18,19]. It is likely that atomic nickel vapor from the comet's atmosphere formed a thin film

of nickel on them when it collided with terrestrial objects.

The authors have shown the possibility of using specific film microstructures to identify both UCB and other cosmic bodies of presumably cometary origin, to which we referred UCB.

Studying the trails of fallen comets is extremely important, as they can carry traces of extraterrestrial life, and could also destroy ancient civilizations.

Author Contributions

Tselmovich V.A.: General work management, sample preparation, microscopic and microprobe measurements.

Amelin I.I.: Organization of expeditionary work in 2016-2017, collection of samples.

Gusiakov V.K.: Substantiation of research, processing of expeditionary results.

Kirillov V.E.: Primary expeditionary work at the site of the fall of the Uchur cosmic body in 1993.

Kurazhkovskii A.Yu.: Magnetic measurements of peat samples.

Conflict of Interest

No conflict of interest.

Funding

The work was carried out within the framework of the state tasks of the IPE RAS (project no. FMWU-2022-0026, project no. FMWU-2022-0027) and IVMiMG SO RAN (project no. 0251-2021-0004).

Acknowledgement

The authors express their gratitude to the administrations of the institutes (Geophysical Observatory Borok, Branch of the Schmidt Institute of Physics of the Earth, Russian Academy of Sciences, Institute of Computational Mathematics and Mathematical Geophysics of the Russian Academy of Sciences and Institute of Tectonics and Geophysics named after Yu. Kosygin, Russian Academy of Sciences) for the possibility of carrying out expeditionary work and analytical studies.

References

[1] Гусяков В.К., 2021. От Чикскулуба до Челябинска: космические катастрофы на Земле. (Russian) [From Chikskulub to Chelyabinsk: Space catastrophes on Earth. Science First Hand]. Наука из первых рук. 1/2(91), 6-27.

[2] Tselmovich, V.A., Kurazhkovskii, A.Yu., Kazansky, A.Yu., et al., 2019. Studying the dynamics of cosmic dust flux on the Earth's surface from peat deposits. Izvestiya, Physics of the Solid Earth. 55, 517-527.

[3] Песков, А.Ю., Крутикова, В.О., Захарченко, Е.Н., et al., 2020. ГЕОХИМИЯ И МАГНЕТИЗМ ТОРФЯНИКОВ МЕЖДУРЕЧЬЯ РЕК ХОР И КИЯ, СИХОТЭ-АЛИНЬ (ПРЕДВАРИТЕЛЬНЫЕ ДАННЫЕ) (Russian) [Geochemistry and magnetism of peatlands in the interfluous of the Khor and Kia rivers, Sikhote-alin (preliminary data)]. ТИХООКЕАНСКАЯ ГЕОЛОГИЯ. 39(2), 79-89.

[4] Васильев, Н.В., 2004. Тунгусский метеорит. Космический феномен лета 1908 года. М.: Русская панорама (Russian) [Space phenomenon in the summer of 1908]. Russian panorama: Moscow. pp. 359.

[5] Кринов, Е.Л., 1981. Железный дождь (Russian) [Iron rain]. Nauka: Moscow. pp. 191.

[6] Дудоров, А.Е., 2020. Частота падений метеоритов и болидов (Russian) [The frequency of falling meteorites and fireballs]. Астрономический вестник. 54(3), 247-259.

[7] Kulagin, V.P., Shustov, B.M., Kuznetsov, Y.M., et al., 2016. Methods and means of information-analytical assessment of asteroid and comet hazard. Solar System Research. 50, 464-470. DOI: https://doi.org/10.1134/S0038094616070145

[8] Bobrowsky, P.T., Rickman, H., 2007. The asteroid impact hazard and interdisciplinary issues. Comet/asteroid impacts and human society. An interdisciplinary approach. Springer-Verlag:

Berlin. pp.146-162.

[9] Ivanov, B.A., Hartmann, W.K., 2007. Exogenic dynamics, cratering and surface ages. Treatise on geophysics. Elsevier: Amsterdam. pp. 207-242.

[10] Амелин, И.И., Гусяков, В.К., Ляпидевская, З.А., 2013. Методика оценки частоты импактных событий (Russian) [Methods for estimating the frequency of impact events]. Проблемы информатики. 4, 21-35.

[11] Витязев, А.В., Печерникова, Г.В., 1997. Астероидная и сейсмическая опасность: введение в новые аспекты проблемы (Russian) [Asteroid and seismic hazard: An introduction to new aspects of the problem]. ИФЗ РАН. 69.

[12] Кириллов, В.Е., 2004. Маршрутами, тропами и дорогами. Из бродяжьих воспоминаний дальневосточного геолога-поисковика (Russian) [Routes, paths and roads. From the vagabond memoirs of a Far Eastern prospecting geologist]. Хабаровск. 146.

[13] Badyukov, D.D., Ivanov, A.V., Raitala, J., et al., 2011. Spherules from the Tunguska event site: Could they originate from the Tunguska Cosmic Body? Geochemistry International. 49, 641-653.

[14] Цельмович, В.А. (editor), 2015. Возможность микроскопической диагностики космической пыли в торфе. Метеориты, астероиды, кометы. Материалы международной конференции и школы молодых ученых (Russian) [The possibility of microscopic diagnostics of cosmic dust in peat. Meteorites, asteroids, comets. Materials of the International Conference and School of Young Scientists]; 2015 May 21-23; Miass. p. 193-196.

[15] Цветков, В.И., 1989. Сихоте-Алиньский метеорит (Russia) [Sikhote-Alin meteorite]. Nature. 8, 78-85.

[16] Antipin, V.S., Yazev, S.A., Perepelov, A.B., et al., 2005. The 25 September 2002 Vitim meteorite: Results of complex research. Russian Geology and Geophysics. 46(10), 1050-1064.

[17] Kolesnikov, E.M., Longo, G., Bettger, T., et al., 2003. Isotope-geochemical study of nitrogen and carbon in peat from the explosion site of the Tunguska space body. Icarus. 161(2), 235-243.

[18] Manfroid, J., Hutsemékers, D., Jehin, E., 2021. Iron and nickel atoms in cometary atmospheres even far from the Sun. Nature. 593(7859), 372-374.
DOI: https://doi.org/10.1038/s41586-021-03435-0

[19] Guzik, P., Drahus, M., 2021. Gaseous atomic nickel in the coma of interstellar comet 2I/Borisov. Nature. 593(7859), 375-378.
DOI: https://doi.org/10.1038/s41586-021-03485-4

BILINGUAL PUBLISHING GROUP

Advances in Geological and Geotechnical Engineering Research

https://ojs.bilpublishing.com/index.php/agger

ARTICLE

Some Results of Direct FR Technology Applied to Study Methane Seepage Areas in the Arctic Region

***Mykola Yakymchuk*[1], *Ignat Korchagin*[2], *Valery Soloviev*[2*]**

[1] *Institute of Applied Problems of Ecology, Geophysics and Geochemistry, Kyiv, 03126, Ukraine*

[2] *Institute of Geophysics, NAS of Ukraine, Kyiv, 03680, Ukraine*

ABSTRACT

The experimental study of the seepage processes' sources formation in structures of the Arctic Region was carried out using modified methods of frequency-resonance (FR) processing and decoding of satellite images and photographs with the vertical scanning of the cross-sections. The newly obtained results show that the intensity and dynamics of the methane seeps and pockmarks fields' formation depend on active deep degassing processes in the continental margin structures. The use of direct FR-sounding technologies allows for determining the probable origin and depth of geological sources of gas migration at marginal migration centers in Greenland, and Norwegian and Barents Seas. New results confirm the crust-mantle gas fluids' influence on the nature and degassing processes features in the scan points of polar marginal structures. These data are important arguments in favor of the "volcanic model" of various structural elements formation in this and other regions. The FR technologies data also showed a possibility of seeps use as shallow and deep hydrocarbon field indicators in gas emission areas. These independent data can be used in compiling models of the deep lithosphere structure and possible mechanisms of abiogenetic hydrocarbon formation in Arctic margin structures. The authors suppose that hydrocarbons through deep channels migrate (from 57 km deep) to the upper crustal horizons where their fields can form. During this migration, gas seeps and pockmarks are formed on the sea bottom and part of the gas can migrate into the atmosphere. Data show that basaltic volcanoes in Greenland scan points can be the real channels through which hydrogen migrates to the upper crustal horizons and further into the atmosphere. Active gas migration in Arctic seepage areas can be an important factor in the global climate change processes.

Keywords: FR mobile technologies; Active hydrocarbon seepage; Greenland; Spitsbergen; Polar Arctic

*CORRESPONDING AUTHOR:

Valery Soloviev, Institute of Geophysics, NAS of Ukraine, Kyiv, 03680, Ukraine; Email: solvalera@ukr.net

ARTICLE INFO

Received: 19 June 2023 | Revised: 6 July 2023 | Accepted: 10 July 2023 | Published Online: 19 July 2023

DOI: https://doi.org/10.30564/agger.v5i3.5792

CITATION

Yakymchuk, M., Korchagin, I., Soloviev, V., 2023. Some Results of Direct FR Technology Applied to Study Methane Seepage Areas in the Arctic Region. Advances in Geological and Geotechnical Engineering Research. 5(3): 25-38. DOI: https://doi.org/10.30564/agger.v5i3.5792

COPYRIGHT

Copyright © 2023 by the author(s). Published by Bilingual Publishing Group. This is an open access article under the Creative Commons Attribution-NonCommercial 4.0 International (CC BY-NC 4.0) License. (https://creativecommons.org/licenses/by-nc/4.0/).

1. Introduction

The idea of the Earth's deep zones degassing is an important factor in the development and evolution of our planet [1]. It allows us to reconsider the interconnected processes of global volcanism and the intrusion of deep fluids, mud volcanism, and local and long-lived gas seeps—zones of the anomalous release of carbon dioxide, methane, hydrogen, helium, nitrogen, and other gases.

These processes are realized due to the functioning of long-term active influence of localized flows of hydrocarbon fluids (mantle degassing products) on the rocks of deep and near-surface structures of various ages and genesis through the "gas pipes" (point channels) and deep linear fracture zones.

An important role in the inflow of deep fluids into the upper horizons of the earth's crust is played by the presence of a developed network of faults, as well as processes of tectonic activation, due to which degassing and concentration of gas emissions in emission centers occur.

New technologies for the interpretation of Earth remote sensing data (ERS-data) significantly complement the results of complex geological and geophysical research in hard-to-reach Polar marine areas and shelf structures of the World Ocean [2]. Special attention to the identification and study of modern methane-degassing sites in the Polar continental margins is connected with their important impact on the global climate change processes [3,4].

2. General principles and methods

Experimental studies were carried out using modified methods of frequency-resonance (FR) processing and decoding of satellite images and photographs, vertical scanning of the cross-section, and the method of integral assessment of hydrocarbon potential prospects areas [5-8].

These methods use the principles of the "substance" paradigm of geophysical research, the essence of which is to search for a specific substance in the sections- oil, gas, gas condensate, water, metals, hydrogen, etc. They are based on the experimentally proven assumption that a large amount of a homogeneous substance creates an electromagnetic field characteristic of a given substance, the radiation power of which is proportional to the concentration of the substance [5-8].

A separate method of this technology allows within the contours of detected anomalous zones (at the resonance frequencies of gas) to estimate the maximum value of the fluid pressure in the reservoirs at different intervals (depth including) of the cross-section.

According to the new paradigm of conducting geophysical research, the focus is not on the selection of certain structural elements in the section and the determination of their physical properties, but on the detection of the specific substances in the section [2,5-8].

Databases of chemical elements, minerals, oil, and condensate samples, as well as sedimentary, igneous, and metamorphic rocks, are classified and divided into separate types and groups, the resonance frequencies of which are used in the processing satellite images and photographs, and became important components in the modifications of direct search methods.

The developed methods are based on the analysis of standing electric wave distribution, discovered by Nikola Tesla in 1899 in the deep horizons of the Earth. In modified versions of the methods of frequency-resonance processing of satellite images and photographs, as well as vertical sounding (scanning) of the cross-section, existing databases (sets, collections) of sedimentary, metamorphic, and igneous rocks (http://rockref.vsegei.ru/petro/), minerals and chemical elements are used. The peculiarities and potentialities of the methods used, as well as the technique of instrumental measurements, carried out [2,5,6,8].

In the process of performing experimental studies of a reconnaissance or detailed nature (carrying out instrumental measurements!) within the blocks and areas of the survey, the following sequence of procedures (graphs) for processing an individual satellite

image (or its local fragment) is used.

1) The procedure for fixing responses (signals) from the surface at the frequencies of the following set of substances: oil, condensate, gas, amber, bacteria (methane-oxidizing bacteria), shale, gas hydrates, ice, coal, anthracite, hydrogen, living (deep) water, dead water, diamonds, potassium magnesium salt, sodium chloride salt;

2) Graph of responses from the groups of sedimentary, metamorphic, and igneous rocks in the cross-section registration;

3) Procedure for determining the presence of the deep channels (volcanoes) in a survey area that is filled with various groups of rocks; assessment of depths of the roots of volcanoes location;

5) Graph for determining groups of rocks (or individual samples of groups), from which signals are recorded at frequencies of oil, condensate, gas, and water;

6) The procedure for recording responses of oil, condensate, gas, and phosphorus at the surface (depth) of 57 km—the boundary of the hydrocarbons synthesis in deep channels (Volcanoes and Faults), filled with certain groups of rocks [6];

7) Graph of signals registration from water on the surfaces of 11, 46, 57, and 68 km—the predicted boundaries of water synthesis in volcanoes of a certain type [6];

8) The procedure for scanning a cross-section with different steps from the surface up to 15 km to determine the depth intervals, within which responses are recorded at the resonant frequencies of oil, condensate, and gas. Refinement of the depths of the location of the most promising hydrocarbon intervals of cross-section during additional scanning with a finer step;

9) Graph for assessing the depth of the upper boundary (edge) of basalts, as well as the depths of the beginning of fixing responses at the resonant frequencies of hydrogen and living (healing) water from basalts. It is implemented in case of fixing responses from the 6-th group of igneous rocks (basalts) in the surveyed area.

3. Results

Previously, examples of the developed direct universal FR-sounding technologies used for solving a wide range of geological and geophysical problems were shown [2,5,6,8]. They include: 1) determining the composition and the main features of the deep structure of the studied structures; 2) assessment of the prospects of territories for the most important types of minerals; 3) determination of the volcanic structures composition and their formation depth; 4) detection and mapping of deep fluid migration vertical channels; 5) identification of local areas of gas emission into the atmosphere and assessment of the sources of degassing processes depth.

The use of the universal "substance" paradigm in the study of pockmarks, seeps, gas hydrates, and mud volcanoes as a result of frequency-resonance studies, makes it possible to obtain new and independent data on their composition, formation depths, and position in the section, to reveal the presence of gas emissions from bottom structures.

The data obtained can be used to assess the manifestation of degassing processes in local structures, as well as to establish their possible connection with deep accumulations of hydrocarbons.

Detection and mapping of gas hydrates in the sections of sedimentary strata make it possible to assess their origin and the degree of their participation in the processes of migration of "greenhouse" gases into the atmosphere. Special attention to the identification and study of modern methane-degassing places is connected with the assessment of their impact on the processes of global climate change [4].

Some results of the use of these technologies on modern methane seepage sites in various structures of the Polar margins are considered below (**Figure 1**).

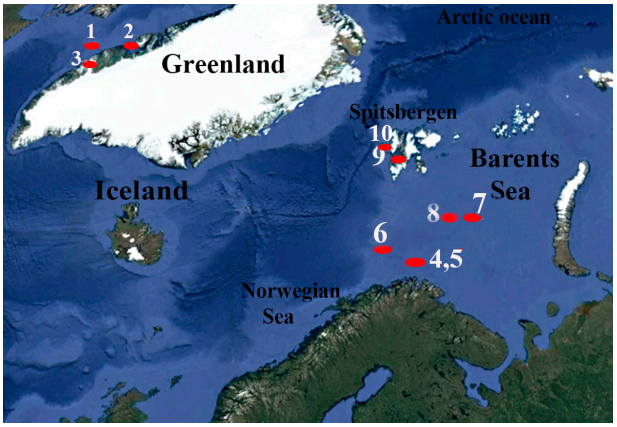

Figure 1. FR-scanning points (SP) position in the Polar Region, and their coordinates (1: 68°24.148 N, 55°43.383 W; 2: 69°12.762 N, 51°27.541 W; 3: 65°15' N, 51°50' W; 4: 71°36'00" N, 21°10'00" E; 5: 71°26'25" N, 20°47'10" E; 6: 72°00.05 N, 14°43.5 E; 7: 75°09'20" N, 32°05'00" E; 8: 75°00'00" N, 28°00'00" E; 9: 78°20'00" N, 15°27'00" E; 10: 78°39'12" N, 09°25'48" E.

3.1 Seepage areas in the central West Greenland margin

In the central part of the Western Greenland margin (Disko Bay region), two FR scanning points (PG2011-12 and PG2012-03), located within fields of pockmarks and seeps were selected for research [9-11].

Sounding point PG2011-12 (Ilulissat area) is located at the south-western flank of the Nuussuaq Basin, and near the mouth of the Isfjord **(Figures 2A and 2B)**, at a depth of 433 m, inside the largest pockmark, the width of which reaches 200 m, and the depth is 23 m. No acoustic indications for hydrocarbons within the Mesozoic strata have been reported for this distal part of the Nuussuaq Basin [9].

Seismic data showed that the pockmarks resulted due to expulsing fluids, neo-tectonic faulting, and crustal uplift [11]. Active modern gas migration in pockmarks was not observed, and it can be supposed that the pockmarks are the result only of neo-tectonic activity and gas hydrate was not involved in their formation in this area [9].

Our FR-sounding data of the PG2011-12 satellite image confirmed the modern active migration of gas but there are no signals from gas hydrates. Salt signals are recorded in the range of 435-882 meters. The joint signal of gas and salt is fixed in the interval of 468-742 m. FR data fixed the salt volcano presence with the root at 99 km. A hydrocarbon synthesis signal is recorded at a depth of 57 km.

Scanning point site PG2012-03 is located in the deepest part of a pockmark-like structure with a large diapir in the upper sediment unit where gas/fluid escape features lie close to the seabed [9]. The seismic data show that in an elongated depression (20 × 35 km large, 575 m deep) on the inner shelf west of Disko Bay younger sediments (**Figure 2C**) cover the Cretaceous-Paleocene strata with gas-hydrates and a bottom simulating reflector (BSR) below seabed [9].

The presence of gas hydrates is significant for future petroleum exploration offshore Greenland but gas hydrates there are mainly in sectors with a thin young sediment cover. The new geochemical data point to methane migration from a deeper-lying petroleum system [9].

These data are confirmed by the FR-sounding results at point PG 2012-03, where the signals of synthesis of oil, gas condensate, and gas at a depth of 57 km are recorded, and there are no signals of gas hydrates. It has been established that the signals at the resonant frequencies of oil, condensate, and gas are recorded only in areas, where the channels (volcanoes) are filled with certain groups of sedimentary and igneous rocks. In the survey areas, the responses from the Hydrocarbons are recorded at a boundary of 57 km within the central parts of the channels (volcanoes) of the deep fluid migration. Below this boundary, the responses are recorded at the frequencies of hydrogen and carbon, above that of oil, condensate, and gas.

The salt signal is fixed in the interval of 588-810 meters, and the joint signal of salt and gas is fixed in the interval of 590-766 meters (**Figure 2C**). The signals of dolomites (0.81-1.3 km, 2.0-99 km) and the ultramafic magma group (1.3-2.0 km, 99-470 km) are recorded. A degassing process with gas migration from the surface to the atmosphere is fixed though no sign of present-day gas seepage was found in the area [9].

These results support previous predictions that

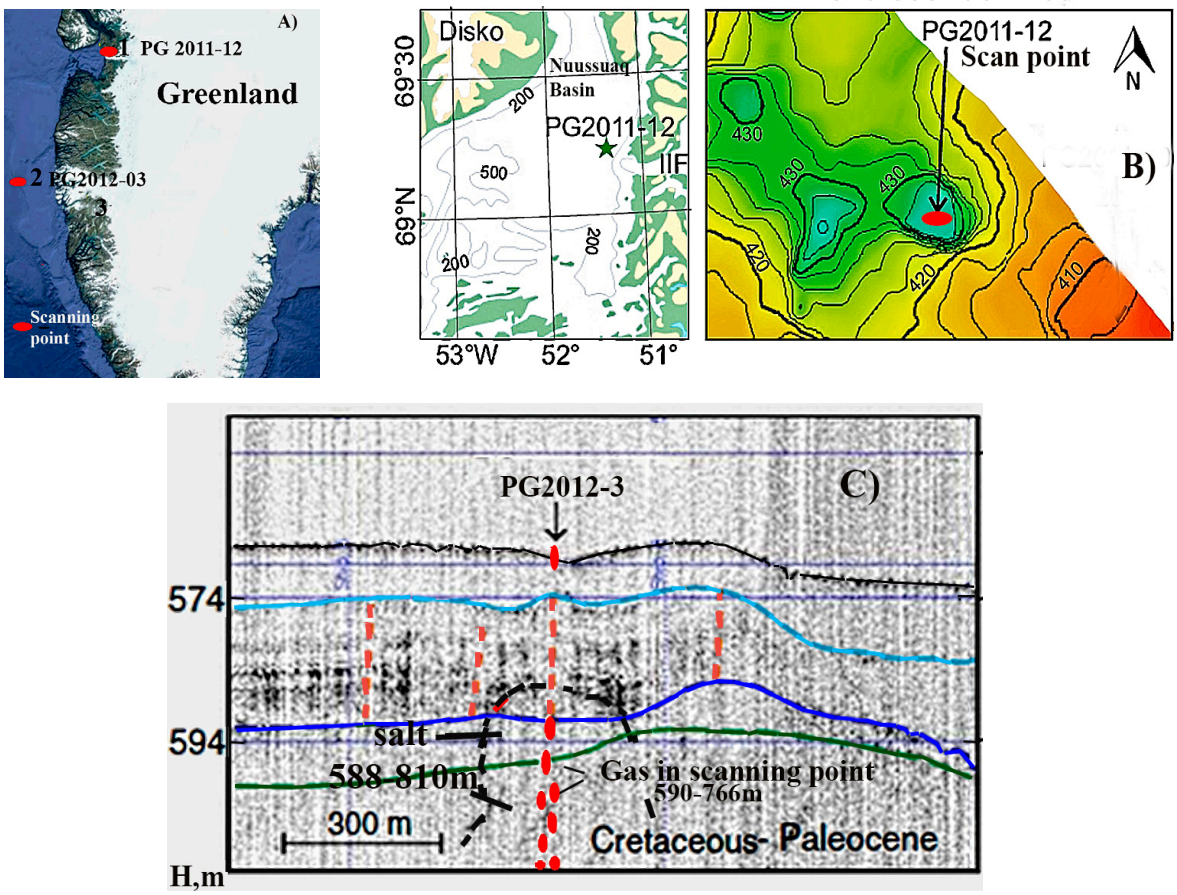

Figure 2. Seepage areas in central West Greenland continental margin (A); B: bottom relief in Nuussuaq Basin (Disko Bay) and PG 2011-12 scan point position off the mouth of Ilulissat Isfjord (IIF) [9]; C: high-resolution seismic profile structure across PG 2012-03 point. In (C) the light blue, dark blue, and green lines are the units in a 40 m thick sediment sequence; the orange lines are gas-fluid escape features [9].

Mesozoic sedimentary basins in the central West Greenland margins could hold high quantities of oil and gas but the processes of mature source rocks in the subsurface, their transformation, and the vertical and lateral migration of hydrocarbons into traps are enough debatable [12]. We suppose that gas originated not only from gas hydrates and the Cretaceous-Paleocene sediments because our data showed the possible realization of the abiotic hydrocarbon crustal-mantle generation mechanism in this as in other Arctic areas.

3.2 Maniitsoq structure, central West Greenland

The Maniitsoq structure in the North Atlantic Craton of West Greenland (**Figure 3**) has been proposed to host a ~3 Gyr old impact crater, allegedly the oldest on Earth but these interpretations have been challenged [13,18].

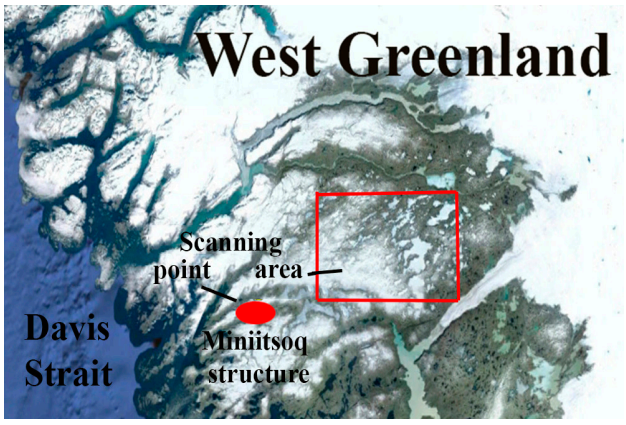

Figure 3. FR-scanning point in Maniitsoq structure position in West Greenland (65°15' N, 51°50' W) and scanning area with the possible process of hydrogen degassing position (red square).

Many geological features in the Maniitsoq region associated with impacts (from microscopic structures

at the mineral scale to macroscopic structures at the terrane scale, as well as the age and geochemistry of rocks) can be explained by endogenous (non-impact) processes that are related to magmatism, metamorphism, and deformation associated with tectonometamorphic reworking and stabilization of the North Atlantic Craton in the late Archean [13].

During the processing using the FR methods of satellite images within the Maniitsoq structure (scanning point position in **Figure 1**), a volcanic complex filled with ultramafic rocks was discovered with a root at a depth of 723 km. It is an additional argument in favor of the endogenous nature of its origin. A volcano with a root at a depth of 99 km and an upper boundary at a depth of 15 m was discovered in the surveyed hydrogen-degassing area located to the East of the Maniitsoq structure (**Figure 3**, red square). Responses at hydrogen frequencies are recorded here from 25 m. The results of the study of areas of active hydrogen degassing were found according to the data of FR-scans in various regions of the world [8].

Thus, the results of experimental studies using the FR scanning method provide new independent information indicating the endogenous (non-impact) nature of this structure, which is confirmed by the materials of modern geological and geochemical studies [13].

3.3 Barents Sea areas

We used the FR methods to study the nature and determine the degassing processes' sources origin, and the depth of their formation in various structures of the Barents Sea, including in areas where large gas fields are located, and hydrocarbon fluids migrated from deep-seated reservoirs (**Figure 1**).

Southwestern Barents Sea, Hammerfest Basin

The SW Barents Sea is located between Norway and the Svalbard archipelago. There are large seeps and pockmarks areas, gas chimneys, and leaking faults systems that show hydrocarbon leakage and fluid migration in structures of this Region.

The known Snøhvit and Albatross fields are located in the SW Barents Sea, in the Hammerfest Sedimentary Basin (**Figure 4**).

FR methods were used in this area where the sub-bottom hydrocarbon fluid-flow process and leakage were discovered by seismic data that included zones of chaotic low-amplitude seismic, discontinuous reflections in the seismic records, areas of high amplitude anomalies, vertical fluid flow features and shallow gas accumulations [14].

Active methane seepage in the study area may be due to the thermogenic and abiogenic oil and gas source, the negative effect of global warming on the ice sheet, permafrost, and gas hydrate stability, some mechanisms of the influence of deep faulting tectonics and tectonic deformation system in the lithosphere-asthenosphere. Other factors such as neotectonics, glaciation history, and deep and shallow degassing processes from hydrocarbon reservoirs of the petroleum system that includes multiple source rocks from the Carboniferous to the Cretaceous are the major factors too [14].

The major deep-seated faults are the main hydrocarbon migration pathways from the deep source rocks and the reservoirs; further leakage to the seabed was through the smaller Paleocene to Early Eocene faults. The major gas chimneys in the southwestern and northeastern parts of the field originated from the Triassic source and reservoir rocks [15,16].

As a result of FR scanning at a point near 7121/4-1 well (Snohvit Field) the gas signal is fixed in the intervals: 362-496 m, 515-673 m, 769-879 m, 896-1027 m.

Obtained data can confirm the fact that natural shallow gas is discovered in some deep hydrocarbon layers of reservoir rocks stacked vertically in the scanning points and formed gas chimneys, pockmarks, and fluid escape pipes in this area.

At the surface, a signal of degassing is recorded, and their gas migrates to the atmosphere (**Figure 4B**).

FR scanning shows that gas signals of high intensity are fixed up to 10 km. We think that the roots of this petroleum system originated not only in source rocks from the Carboniferous to the Cretaceous [14]

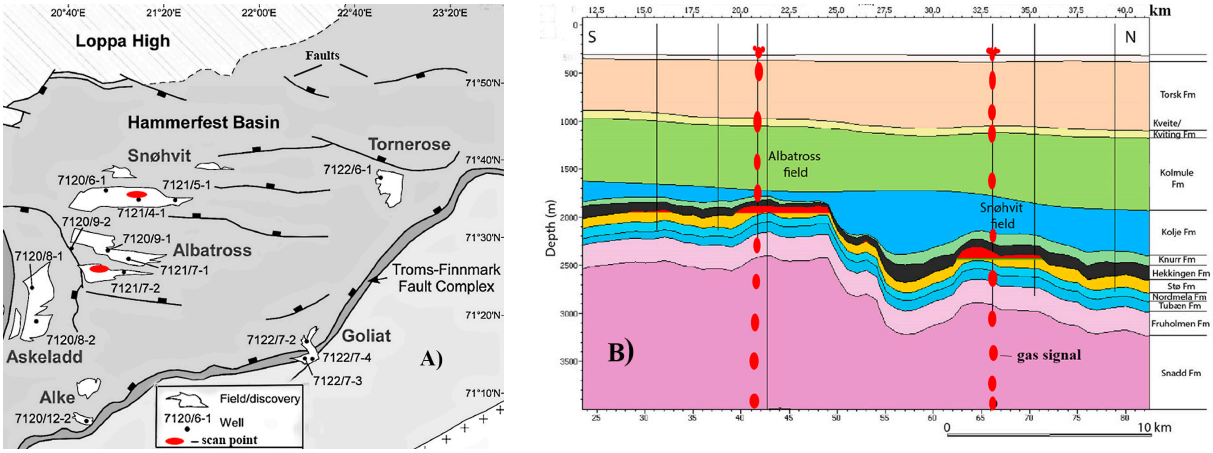

Figure 4. Schematic map (A) of the Hammerfest Basin (SW Barents Sea) with structural elements, Fields and wells [15,16]; B: a well section profile across the Snøhvit reservoir with the results of FR scanning and the depths of the reservoirs [17].

but much deeper, at a depth where a hydrocarbon synthesis signal is recorded [5-8].

The Haakon Mosby mud volcano

Seafloor mud volcano Haakon Mosby (72°00.05 N, 14°43.5 E) with a diameter of 1.5 km is located in SW Barents Sea at a depth of 1250 m in the area between the coast of Norway and Bear Island (**Figure 1**).

It was discovered in 1995. The main products of its eruptions are mud and gases, of which more than 99% is methane. Under the mud volcano, there is a 1- to 2-km-wide disturbed zone with free gas which extends to a depth of > 3 km [18]. Reconnaissance scanning showed that oil and gas signals were found in the section of the mud volcano, and the emission of gases into the water column was also confirmed.

Northern Norwegian Barents Sea, Sentralbanken high area

Methane fluxes from > 7000 seeps in the Arctic significantly deplete seawater, but nevertheless, reach the sea surface and may transfer to the atmosphere [19,20]. 4,137 acoustic 'flares' diagnostic of bubble emission sites (seeps) were identified at the Sentralbanken area with the highest gas flare density in the central part of this structural high (**Figure 5**).

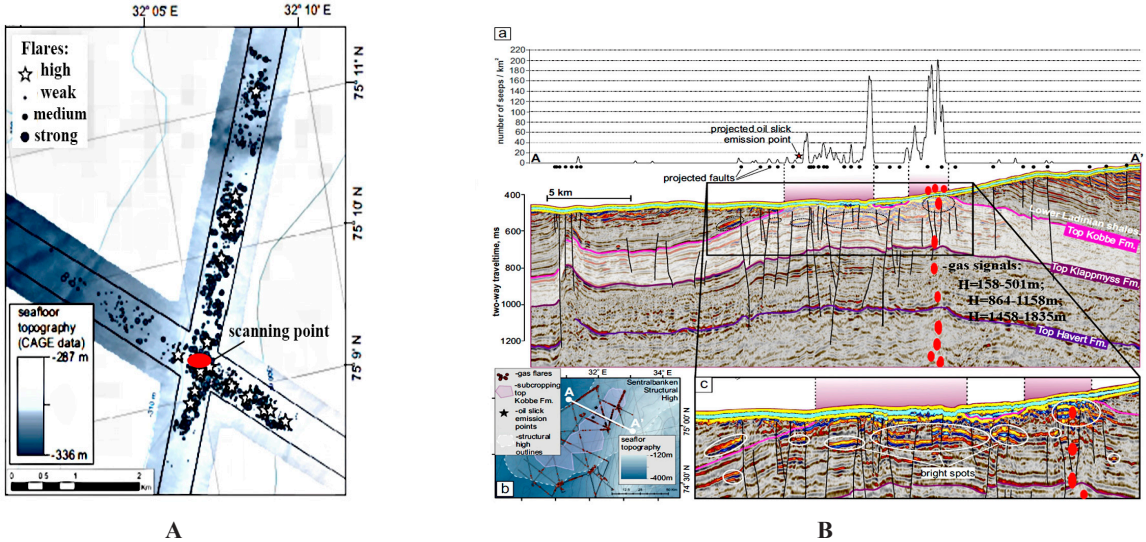

Figure 5. Gas flares location (A) in the Sentralbanken high area [20]; B: correlation of gas release and sub-cropping reservoir Kobbe Formation and faults. a: seepage density, faults, and sub-cropping Kobbe Formation along transect A-A'; b: transect A-A' location; c: bright spots distribution within the apex of Sentralbanken structural high [20]. There is also a possible depth of gas signals by FR scanning (B, a, c).

The results of FR scanning in the Sentralbanken area show that the signal of old granites is recorded from 470 km. The signals of oil, gas, and gas condensate are recorded at a depth of 57 km. The gas signal is fixed in depth intervals: 158-501 m, 864-1158 m, 1458-1835 m, further probing was not carried out. The gas signals are recorded in the depth range of 1,835-10 km. The signal of gas hydrates is fixed in the interval 0-400 m. The degassing process from the water surface into the atmosphere is recorded.

These obtained data indicate the existence of additional sources and processes of deep degassing that can explain the magnitude of the formation and manifestation of seep and pockmark fields in various structures of the Barents and other seas of the Arctic region.

Norwegian Barents Sea

The first studies of pockmark fields in the Norwegian part of the Barents Sea [19-21] showed that the main part of the round or oval pockmarks found during the research had a diameter of 10 to 400 m and a depth of 2 to 15 m, and was found in the form of single structures, clusters, and extended chains.

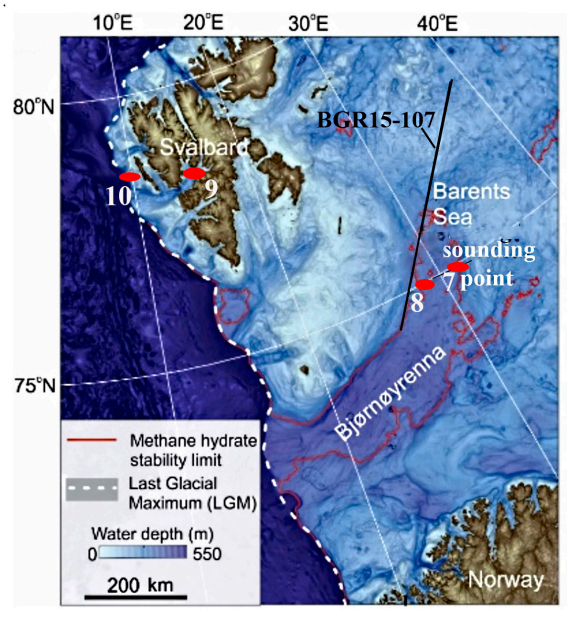

Figure 6. The sounding points in the degassing areas in the Barents Sea [19,20] and Spitsbergen [26,28], and the modeling profile position in the Norwegian part of the Barents Sea [22].

The formation of such accumulations of pockmarks could occur in various areas of the Barents Sea as a result of seepage of gases of deep or biogenic (in the case of thick sedimentary strata) origin [23].

Gas flares (more than 600), consisting of 97% methane and rising above the bottom to a height of up to 200 m, as well as numerous pingos (heaving mounds), the diameter of which reached 1100 m, were found at the research site, and the height is 20 m. Methane flares confirm the presence of modern degassing processes in this region, caused, according to the authors, by the decomposition of gas hydrates [19].

From our point of view, the formation of such gigantic (more than 1 km in diameter) pockmarks requires the involvement of additional sources of impulsive methane supply over a long period. The mechanism of deep degassing by "gas pipes" through accumulations of gas hydrates seems to be more reliable in explaining the formation of these large bottom structures. Such a mechanism was proposed for one of the sites (Hornsund Fault Zone) in the northwestern part of the Barents Sea [2].

The results of FR-sounding (up to 8.0 km) in the area of accumulation of giant pockmarks and pingos (**Figures 6 and 7**) showed that signals from hydrocarbons and the presence of gas accumulations are recorded here at depths: 1.3-2.0 km, 2.29-3.12 km, and 3.32-4.5 km. The intervals of these distinguished depths of gas accumulations are close to the depths of oil and gas—bearing Paleocene-Eocene and Middle Triassic horizons containing hydrocarbon source rocks enough for the formation of oil and thermogenic gas [22-24]. The presence of a fault system (**Figure 7**) makes it possible for deep gases to migrate to the upper horizons of the sedimentary strata, which creates additional conditions for the formation of pockmark and pingo fields in this area.

3.4 Spitsbergen area

Seep area in the Greenland Sea

On the continental margin of Svalbard (**Figure 1**), the field of seep accumulations was studied and the main factors of the formation and evolution of the gas hydrate stability zone were determined, as well

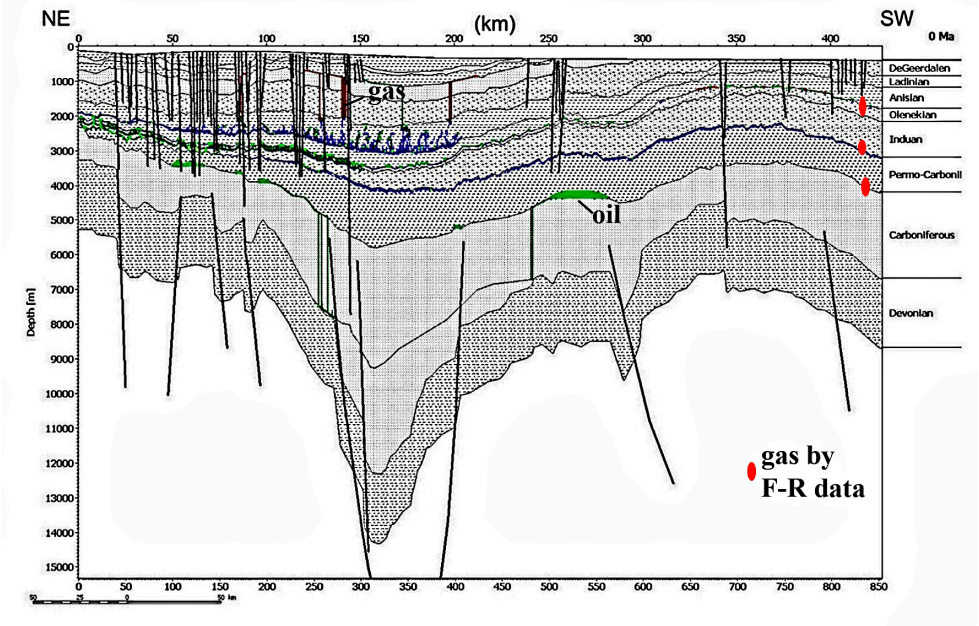

Figure 7. Modeling profile BGR15-107. The position of faults, accumulations of hydrocarbons, and the boundaries of oil-saturated (above the threshold value of 0.01%) sedimentary rocks are shown [22]. The position of gas accumulation zones according to FR-sounding data in the southwestern part of the section is also shown. The position of the profile is in **Figure 6**.

as the patterns of distribution of sources of methane plumes in the section [25,26].

The zone of stability of gas hydrates extends to a depth of 370-410 m (**Figure 8**), and the available results of seismic studies show the presence in this area of a system of "gas pipes" through which gas migrates into the sedimentary strata from deep gas "pockets" [25]. The authors suggest that the "gas pipes" do not reach the bottom surface.

The mechanism of gas transfer has not been sufficiently studied, since no extended, going to great depths, faults, which are considered to be the main

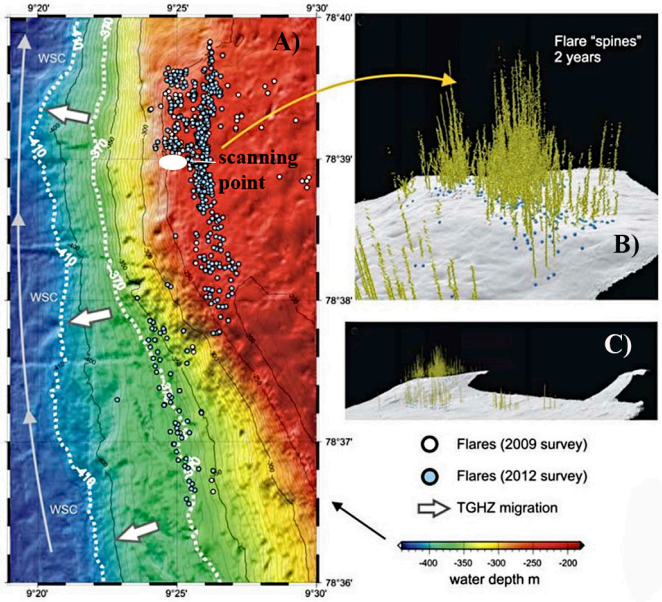

Figure 8. Bathymetric map (A) of the continental margin of the Spitsbergen area with a field of seeps (A) and their three-dimensional image (B, C) in the study area [26]. WSC, CC, and ESC are the dominant currents in this area (Western Spitsbergen; Coastal; East Spitsbergen Current). Arrows indicate the migration of the gas hydrate stability zone (TGHZ) over the past 30 years from a depth of 370 m to 410 m [27].

element of the influx of deep fluids into the sedimentary strata, have been found in the study area.

Studies of seep fields identified along the continental margin to the west of Svalbard at depths of 150-400 m showed that the released methane is due to the dissociation of gas hydrates due to a 1 °C increase in the temperature of the West Svalbard Current over the past 30 years. The presence of numerous additional flares at the shelf suggests that this particular region west of Prins Kalrs Forland is prone to hydrocarbon seepage and that gas seafloor emission unaffected by gas hydrate dissociation is common in the region [27].

It is assumed that such a relationship between the formation of methane seep fields and the processes of destruction of gas hydrates is also characteristic of other regions of the polar Arctic.

Based on the results of FR sounding at a scanning point in the central part of the seep field (**Figure 8**), gas accumulations were identified that form methane flares of this field, located in the upper part of the earth's crust.

Degassing processes occur from depths: 731-905 m, 1084-1141 m, and 1370-1471 m (deeper sounding was not carried out). In addition, gases emission into the water column and the atmosphere are recorded.

Spitsbergen, Isfjorden area

The Spitsbergen and its continental margins' cold seeps are the most studied by geophysical methods in the Arctic. The degassing processes investigation in this area contributed to a detailed study of the formation and evolution of gas hydrate and free gas accumulations, as well as the nature of their sources [2]. Particular emphasis in these works was placed on the study of the dynamics of the dissociation of gas hydrates and gas emissions associated with paleoclimatic changes in the region. Their important result was the identification of numerous fields of pockmarks, as well as associated "degassing pipes" and systems of tectonic faults extending to considerable depths [23-31].

The distribution of pockmarks in Isfjorden has a mosaic character [28], and their most actively expressed fields are spatially associated with known active fault zones of the Svalbard fold-thrust belt and other faults (Billefiorden, Isfiorden Fault Zones).

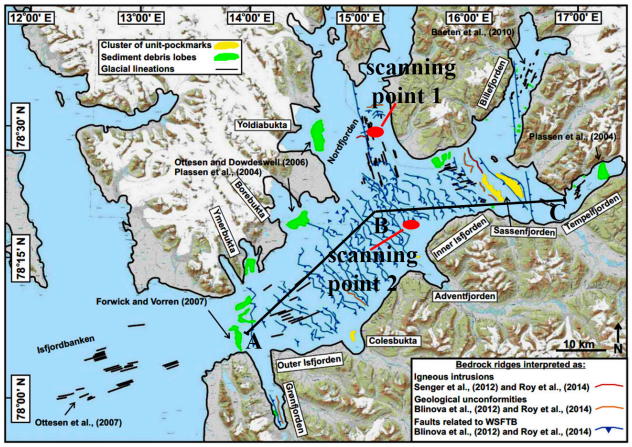

Figure 9. Satellite image of the Isfjorden in Spitsbergen [28] with the scanning points position; A-B-C: seismic profile [29] position.

One of the scanning points of the satellite image of the Svalbard archipelago (scanning point 1, SP1) is located in the north of Isfjorden, in Nordfjorden, in the central part of a large accumulation of pockmarks (**Figure 9**), formed on the southeastern continuation of the Blomesletta fault.

More than 1300 pockmarks (diameter from 14 to 265 m, depth from 1 to 11 m, and frequency of distribution up to 20 per km^2) were found in Isfjorden, and 535 pockmarks—in Nordfjorden [28].

Their genesis can be determined by the influx of hydrocarbon fluids (of biogenic or thermogenic origin), decomposition of gas hydrates, thawing of permafrost, and a number of other factors operating in polar latitudes. Geochemical analysis of hydrocarbon anomalies in the near-surface marine deposits of the fjords in the west and around Svalbard indicates a mixed (thermogenic and biogenic) nature of gases [28,30].

Detailed analysis of geophysical data in Nordfjorden showed the presence of gas flares only above a part of the pockmark fields (**Figure 10**), which may be due to the absence of modern degassing processes and sufficient gas accumulations under them, as well as to changes in the paths of deep fluid migration.

The complex filled with sedimentary rocks of groups 1-7 and 10 were identified at site SP1 (**Figure 10**), with a root at a depth of 470 km. Signals from

oil, gas, gas condensate, carbon dioxide, methane-oxidizing bacteria, yellow phosphorus, oil shale, gas hydrates, anthracite, nitrogen, oxygen, carbon, and ice have been registered [2,5-8].

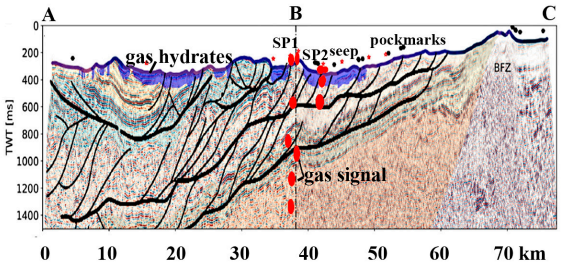

Figure 10. Geological cross-section with GHSZ extents of A-B-C profile [29]. The location of the seismic transect across Isfjorden is shown in **Figure 9**. Pockmarks and flares within 250 m of the transect have been projected onto the profile. BFZ: Billefjorden Fault Zone. SP1 and SP2: FR scanning points.

Responses at the gas frequency were obtained at depths: 1335-1932 m; 2459-3321 m; 3933-4467 m. The sounding in point (SP1) was carried out to a depth of 4789 m. FR instrumental measurements at this point confirmed the gas migration into the atmosphere (**Figure 10**).

The degassing processes and gas migration into the atmosphere at sounding point 2 (SP2) were fixed too. The gas signals were fixed there in intervals: 290-615 m, 996-1159 m, and 1198-1314 m but deeper sounding was not carried out (**Figure 10**).

In the central part of Svalbard, the flow of thermogenic gas along fault zones and large tectonic lineaments may be the main geological factor in the formation of seeps and pockmarks, and other factors (the presence of free gas accumulations, filtration processes, seismic activity, and etc.) may be also important. It is also noted that faults and magmatic sills play an important role in the formation of channels for the flow of fluids into the pockmark fields and the water column in many areas. The processes of active gases entering the water column and the atmosphere can change over time; they depend on many parameters, including the thickness of the water column, temperature, and wave dynamics [31].

4. Discussion

At present, the formation of extensive fields of seeps and pockmarks in the structures of the Polar Regions is mainly explained by the processes of decomposition of gas hydrates. In this case, the presence of sub-hydrate gas in the section and the inflow of deep gas fluids of various genesis is often assumed, partially migrating to the upper horizons of sedimentary strata along faults that disrupt the continuity of gas hydrates.

The study of the fields of methane seeps and pockmarks showed that the intensity and dynamics of their formation largely depend on the influx of gas fluids, the sources of which are located in the deep horizons of the crust and mantle.

The areas of degassing are located within the zones of the existence of volcanic apparatuses with a developed system of deep channels, along which gases migrate, as well as deep oil and condensate. The result of such migration is the formation of gas seeps, as well as oil slicks on the water surface - indicators of deep oil synthesis.

Our data confirm the significant but insufficiently taken into account influence of crustal-mantle gas fluids on the nature and features of degassing processes in the structures of the continental margins of various regions.

The obtained data show that in all the structures studied, the influx of fluids formed in the deep horizons of the lithosphere cannot be ignored [3,5,6,8].

5. Conclusions

The results of FR soundings of structures in the polar Arctic Regions showed that gas hydrates could be formed in various horizons of sedimentary and crystalline rocks of the Earth's crust due to degassing products of the Earth's deep geospheres.

The use of FR technology makes it possible to quickly assess the contribution of various geological sources of methane and other gases to the overall balance of greenhouse gases in the places of their greatest emission.

On the basis of the obtained results of using the technologies of FR-sounding of satellite images and photographs for the structures of the Polar regions, a conclusion was made about the possibility of

remotely determining the material composition, structure, and probable depth of occurrence of sources of deep geofluides migration in various geospheres of the Earth.

The proposed volcanic degassing model for hydrocarbon formation can explain many features of both large-scale and local degassing processes on the Earth.

We believe that modern FR technologies can significantly speed up the processes of remote detection and mapping of numerous new volcanic structures of various types in the World Ocean, as well as similar structures on the planets of the Solar system [6].

The results of the research showed that the use of reference frequencies for various types of known rocks and minerals makes it possible to apply frequency-resonance methods to study the deep structure of our planet and solve the problems of searching for many types of minerals.

Author Contributions

M.Y. and I.K. carried out the experiments and developed the concepts of this research. V.D. collected the data and wrote this manuscript with contributions on discussion from M.Y. and I.K. All authors contributed to reading, manuscript revision, read, and approved the submitted version.

Conflict of Interests

The authors declare no conflict of interest.

References

[1] Shestopalov, V.M., Lukin, A.E., Zgonik, V.A., et al., 2018. БАДАТА-Интек сервис (Russian) [Essays on Earth's degassing]. BADATA-Intek Service: Kyiv. pp. 632.

[2] Yakymchuk, M., Korchagin, I., Levashov, S., et al., 2022. Вулканізм і процеси дегазації в структурах полярних регіонів Землі (огляд за результатами частотно-резонансних досліджень) (Ukrainian) [Volcanism and degassing processes in the structures of the Earth's Polar Regions (review based on the results of frequency-resonance studies)]. Dodo Books Indian Ocean Ltd. and OmniScriptum S.R.L Publishing group: London. pp. 276. Available from: https://morebooks.de/shop-ui/shop/search?q=978-620-0-63606-5&page=1

[3] Bogoyavlensky, V.I., Sizov, O.S., Nikonov, R.A., et al., 2020. Earth degassing in the Arctic: The genesis of natural and anthropogenic methane emissions. Arctica: Ecology and Economy. 39, 6-22.
DOI: https://doi.org/10.25283/2223-4594-2020-3-6-22

[4] WMO Greenhouse Gas Bulletin (GHG Bulletin): The State of Greenhouse Gases in the Atmosphere Based on Global Observations through 2021 [Internet]. Available from: http://www.indiaenvironmentportal.org.in/content/473810/greenhouse-gas-bulletin-ghg-bulletin-the-state-of-greenhouse-gases-in-the-atmosphere-based-on-global-observations-through-2021/

[5] Yakymchuk, N.A., Korchagin, I.N., Bakhmutov, V.G., et al., 2019. Геофизические исследования в Украинской морской антарктической экспедиции 2018 г: мобильная измерительная аппаратура, инновационные прямопоисковые методы, новые результаты (Russian) [Geophysical investigation in the Ukrainian marine Antarctic expedition of 2018: mobile measuring equipment, innovative direct- prospecting methods, new results]. Геоинформатика. 1, 5-27.

[6] Якимчук Н.А., Корчагин И.Н., 2019-2021. Технология частотно-резонансной обработки данных ДЗЗ: результаты практической апробации при поисках полезных ископаемых в различных регионах земного шара (Russian) [Technology of frequency-resonance processing of remote sensing data: Results of practical approbation during mineral searching in various regions of the globe]. Геоинформатика. Часть I. 3(71), 29-51; Часть II. 4, 30-58; Часть III. 1, 19-41; Часть IV. 3, 29-62; Часть V. 3-4, 51-88.

[7] Levashov, S.P., Yakymchuk, N.A., Korchagin, I.N., 2012. Частотно-резонансный принцип,

мобильная геоэлектрическая технология: новая парадигма геофизических исследований (Russian) [Frequency-resonance principle, mobile geoelectric technology: New paradigm of geophysical investigations]. Геофизический журнал. 34(4), 166-176.

[8] Yakymchuk, M., Korchagin, I. (editors), 2023. About the opportunity of direct-prospecting methods application for detection areas of gas and natural hydrogen migration to the surface and in the atmosphere. Proceedings of the 2nd International Scientific Conference; 2023 May 4-5; Dublin, Ireland. p. 220-251.
DOI: https://doi.org/10.5281/zenodo.7905551

[9] Nielsen, T., Laier, T., Kuijpers, A., et al., 2014. Fluid flow and methane occurrences in the Disko Bugt area offshore West Greenland: Indications for gas hydrates? Geo-Marine Letters. 34, 511-523.
DOI: https://doi.org/10.1007/s00367-014-0382-2

[10] Hogan, K.A., Dowdeswell, J.A., Cofaigh, C.Ó., 2012. Glacimarine sedimentary processes and depositional environments in an embayment fed by West Greenland ice streams. Marine Geology. 311, 1-16.

[11] Schumann, K., Völker, D., Weinrebe, W.R., 2012. Acoustic mapping of the Ilulissat Ice Fjord mouth, west Greenland. Quaternary Science Reviews. 40, 78-88.

[12] Christiansen, F.G., Bojesen-Koefoed, J.A., Dam, G., et al., 2020. A review of oil and gas seepage in the Nuussuaq Basin, West Greenland-implications for petroleum exploration. GEUS Bulletin. 44, 4567.
DOI: https://doi.org/10.34194/geusb.v44.4567

[13] Yakymchuk, C., Kirkland, C.L., Cavosie, A.J., et al., 2021. Stirred not shaken; critical evaluation of a proposed Archean meteorite impact in West Greenland. Earth and Planetary Science Letters. 557, 116730.
DOI: https://doi.org/10.1016/j.epsl.2020.116730

[14] Mohammedyasin, S.M., Lippard, S.J., Omosanya, K.O., et al., 2016. Deep-seated faults and hydrocarbon leakage in the Snøhvit Gas Field, Hammerfest Basin, southwestern Barents Sea. Marine and Petroleum Geology. 77, 160-178.
DOI: https://doi.org/10.1016/j.marpetgeo.2016.06.011

[15] Murillo, W.A., Vieth-Hillebrand, A., Horsfield, B., et al., 2016. Petroleum source, maturity, alteration and mixing in the southwestern Barents Sea: New insights from geochemical and isotope data. Marine and Petroleum Geology. 70, 119-143.
DOI: https://doi.org/10.1016/j.marpetgeo.2015.11.009

[16] Tasianas, A., Martens, I., Bünz, S., et al., 2016. Mechanisms initiating fluid migration at Snøhvit and Albatross fields, Barents Sea. Arktos. 2, 1-18.
DOI: https://doi.org/10.1007/s41063-016-0026-z

[17] Ostanin, I., Anka, Z., Di Primio, R., 2017. Role of faults in hydrocarbon leakage in the Hammerfest Basin, SW Barents Sea: Insights from seismic data and numerical modelling. Geosciences. 7(2), 28.
DOI: https://doi.org/10.3390 /geosciences7020028

[18] Shilov, V.V., Druzhinina, N.I., Vasilenko, L.V., et al., 1999. Stratigraphy of sediments from the Haakon Mosby Mud Volcano area. Geo-Marine Letters. 19(1-2), 48-56.

[19] Andreassen, K., Hubbard, A., Winsborrow, M., et al., 2017. Massive blow-out craters formed by hydrate-controlled methane expulsion from the Arctic seafloor. Science. 356(6341), 948-953.

[20] Serov, P., Mattingsdal, R., Winsborrow, M., et al., 2023. Widespread natural methane and oil leakage from sub-marine Arctic reservoirs. Nature Communications. 14(1), 1782.
DOI: https://doi.org/10.1038/s41467-023-37514-9

[21] Vogt, P.R., Gardner, J., Crane, K., 1999. The Norwegian-Barents-Svalbard (NBS) continental margin: Introducing a natural laboratory of mass wasting, hydrates, and ascent of sediment, pore water, and methane. Geo-Marine Letters. 19, 2-21.

[22] Lutz, R., Klitzke, P., Weniger, P., et al., 2021.

Basin and petroleum systems modelling in the northern Norwegian Barents Sea. Marine and Petroleum Geology. 130, 105128.

[23] Solheim, A., Elverhøi, A., 1985. A pockmark field in the Central Barents Sea; gas from a petrogenic source? Polar Research. 3(1), 11-19.

[24] Wallmann, K., Riedel, M., Hong, W.L., et al., 2018. Gas hydrate dissociation off Svalbard induced by isostatic rebound rather than global warming. Nature Communications. 9(1), 83.

[25] Sarkar, S., Berndt, C., Minshull, T.A., et al., 2012. Seismic evidence for shallow gas-escape features associated with a retreating gas hydrate zone offshore west Svalbard. Journal of Geophysical Research: Solid Earth. 117(B9).

[26] Veloso, M., Greinert, J., Mienert, J., et al., 2015. A new methodology for quantifying bubble flow rates in deep water using splitbeam echosounders: Examples from the Arctic offshore NW-Svalbard. Limnology and Oceanography Method. 13, 267-287.

[27] Westbrook, G.K., Thatcher, K.E., Rohling, E.J., et al., 2009. Escape of methane gas from the seabed along the West Spitsbergen continental margin. Geophysical Research Letters. 36(15), L15608.
DOI: https://doi.org/10.1029/2009GL039191

[28] Roy, S., Hovland, M., Noormets, R., et al., 2015. Seepage in Isfjorden and its tributary fjords, West Spitsbergen. Marine Geology. 363, 146-159.
DOI: http://dx.doi.org/10. 1016/j.margeo.2015.02.003

[29] Betlem, P., Roy, S., Birchall, T., et al., 2021. Modelling of the gas hydrate potential in Svalbard's fjords. Journal of Natural Gas Science and Engineering. 94, 104127.
DOI: https://doi.org/10.1016/j.jngse.2021.104127

[30] Forwick, M., Baeten, N.J., Vorren, T.O., 2009. Pockmarks in Spitsbergen fjords. Norwegian Journal of Geology. 89, 65-77.

[31] Roy, S., Senger, K., Hovland, M., et al., 2019. Geological controls on shallow gas distribution and seafloor seepage in an Arctic fjord of Spitsbergen, Norway. Marine and Petroleum Geology. 107, 237-254.
DOI: http://dx.doi.org/10.1016/j.marpetgeo.2019.05.021

BILINGUAL PUBLISHING GROUP

Advances in Geological and Geotechnical Engineering Research

https://ojs.bilpublishing.com/index.php/agger

ARTICLE

Weather Events Associated with Strong Earthquakes and Seismic Swarms in Italy

***Valentino Straser*[1*], *Daniele Cataldi*[2], *Gabriele Cataldi*[2]**

[1] *University Makeni Department of Agriculture, Fatima Campus, Makeni, 00000, Sierra Leone*

[2] *Group Radio Emissions Project, Lariano, Rome, 00076, Italy*

ABSTRACT

This study discusses the possible relationship between potentially destructive seismic events, earthquake swarms, and intense weather events occurring in the same epicentral zone at time intervals ranging from one day to a few weeks. The objective of the present study is, therefore, to analyze the interaction between the lithosphere, atmosphere, and ionosphere in order to propose, prospectively, a new hydro-climatic model to be applied not only in Italy, where this research was carried out. The study concerns some of the most intense Italian earthquakes starting from 1920, with the destructive event in Lunigiana, in North Western Apennines, until the recent earthquake swarm that hit the Emilia-Romagna region followed, as in the cases analyzed in this research, by strong atmospheric disturbances. The recurrence associating seismic events with atmospheric precipitation allows us to propose some hypotheses about the triggering mechanism. In tectonically stressed areas, during pre-seismic and seismic phases, the release of gases from the ground and electrical charges near active faults is known. It is hypothesized that water condensation nuclei are carried by radon gas on atmospheric gases, also originating from cosmic rays in the upper atmosphere, generated by air ionization.

Keywords: Extreme hydro-climatic events; Earthquakes; Radon gas; Earthquake swarms; Atmospheric precipitation

1. Introduction

The dramatic nature of hydro-climatic events that have affected various parts of the Planet makes it possible to consider various triggering mechanisms according to a holistic principle [1-3], that is, consid-

*CORRESPONDING AUTHOR:

Valentino Straser, Department of Agriculture, University of Makeni, Makeni, 00000, Sierra Leone; Email: valentino.straser@gmail.com

ARTICLE INFO

Received: 21 June 2023 | Revised: 31 July 2023 | Accepted: 2 August 2023 | Published Online: 10 August 2023

DOI: https://doi.org/10.30564/agger.v5i3.5802

CITATION

Straser, V., Cataldi, D., Cataldi, G., 2023. Weather Events Associated with Strong Earthquakes and Seismic Swarms in Italy. Advances in Geological and Geotechnical Engineering Research. 5(3): 39-54. DOI: https://doi.org/10.30564/agger.v5i3.5802

COPYRIGHT

Copyright © 2023 by the author(s). Published by Bilingual Publishing Group. This is an open access article under the Creative Commons Attribution-NonCommercial 4.0 International (CC BY-NC 4.0) License. (https://creativecommons.org/licenses/by-nc/4.0/).

ering both anthropogenic impact and geophysical events, without excluding the influence of radiation from the cosmos [4-6]. This mode of investigation is facilitated by technological advances, including satellite data retrieval and the development of new models and interpretation of natural processes by scientific teams. Italian chronicles from the last century and others around the world report the correspondence between potentially destructive seismic events and precipitation, such as rain or snow. Following are some excerpts from news reports.

Earthquake May 6, 1976, Friuli, magnitude 6.5: "After the disastrous telluric events of May 6, September 11 and 15, 1976, winter opened with a cold and snow event of the rare kind for Friuli Venezia Giulia. Here is the account experienced firsthand by yours truly in Udine during that exciting two days that brought over 15 cm of snow to the capital of Friuli" (http://www.centrometeo.com). Earthquake April 6, 2009, L'Aquila, magnitude 6.3: "After last night's tremors that brought back fear among the population of L'Aquila, since the first light of dawn it has been raining continuously on the whole area" (Abruzzo amid bad weather and new tremors—La Stampa. https://www.lastampa.it/cronaca/2009/04/21). Earthquakes of August 24 and October 30, 2016, a magnitude of 6.5 and a swarm of January 18, 2017, with a maximum magnitude of 5.5 in central Italy: "Strong earthquake tremors hit central Italy, already tested by the seismic events of August and October and the copious snowfall in recent days" (https://www.ilsole24ore.com). May 20, 2012 earthquake, magnitude 5.8 with epicentre in Emilia: "May 20, 2012—as early as late morning rain hit the towns affected by the quake and is not expected to subside until at least Monday morning" (https://www.ilfattoquotidiano.it 2012/05/20). "Exacerbating the situation came violent rain that has been falling since the early morning hours on the earthquake-affected municipalities" (https://www.gazzettadimodena.it). On a larger scale, examples of this between minimum depression and potentially destructive earthquakes include the Islands of Greece, or strong earthquakes, such as the Kumamoto earthquake in Japan in 2016. In this case, the main shock was followed by other earthquakes associated with intense precipitation, as Kazunori Miura (personal communication) pointed out with the superposition of seismic tail hypocenters with meteoric events [4]. Similar studies have been carried out by V. Straser, where recurrences of the link between seismic activity and baric variations, with even intense precipitation, two days before or two days after in the epicentral zone of the earthquake have been shown. The production of ions in seismically active zones [7,8] and the release of gases into the atmosphere, which can generate water condensation nuclei, and thus create a link of the interaction between lithosphere and atmosphere, have been discussed by both Sergey Pulinets [9], Sergey Pulinets and Kirill Boyarchuk [10]. Indeed, studies conducted by Nigel Marsh and Henrik Svensmark have shown that cosmic rays influence Earth's climate, through comparisons of changes in cloud cover and the flux of cosmic rays reaching the troposphere [11]. Ions are associated with nanoparticles and filamentous structures of various origins, caused by the combination of meteoric phenomena and ions in the air as reported by Marie-Agnès Courty and Jean-Michel Martinez, which would underlie hydro-climatic triggers [12,13].

2. Method, data, and limits of this research

Data retrieval does not contemplate detailed information on bad weather or weather conditions, especially in years prior to 2010. In this case, the presence of rainfall, drought or frost is mentioned, with no time reference. This has led to many problems in finding weather data to be associated with seismic data.

Meteorological data, to be superimposed on seismic swarm data are highly variable, due to the duration of the seismic swarm. So, if we want to indicate unambiguous meteorological data, regarding a swarm that lasts several months is, as we understand, very difficult and scientifically invalid. In this regard, it was decided to consider the weather data prior to the triggering of the swarm, that is, the date of the

beginning of the seismic tremors.

In some cases, the data did not cover weather conditions, and the duration of weather phenomena such as torrential rains, intense thunderstorms and adverse weather phenomena are not available. It was only possible to indicate when these occurred, where possible, before the seismic shock or the onset of the earthquake swarm.

When we talk about a seismic swarm, we must mention a geographical area (GPS data), but it is known that seismic swarms especially if they are long-lasting can encompass very large areas geographically and here express themselves from a seismic point of view. So, another limitation was precisely to indicate a geographical point where the seismic swarms occurred and there calculate the meteorological condition. The method used in this study was to compare data found on the website.

2.1 Origin of pre-seismic electromagnetic phenomena

Pre-seismic radio emissions (also called "Seismic Electromagnetic Precursors" or SEPs) are a natural phenomenon described for the first time in a scientific publication in 1890 by British geologist John Milne [16]. At present, the scientific community agrees that these radio emissions are generated by the piezoelectric effect caused by the accumulation of tectonic stress on fault edges [17] (**Figure 1**). Laboratory experiments conducted on rock fragments have found that during the creation of fractures in rocks under mechanical stress, they emit radio waves induced by piezoelectricity. This phenomenon is observed when crystals are applied on some of the mechanical stress in certain crystallographic directions: the opposite sides of the crystals were loaded instantly [18,29].

The creation of experimentally induced microfractures in the rocks was demonstrated for the first time through triaxial compression tests [18-21].

The characteristics of the tectonic stress, the geometric characteristics of the fault (irregularities) and the typology of minerals included in it determine the creation of microfractures which has different orientations: This determines the reaction of non-isotropic electromagnetic sources [22-24].

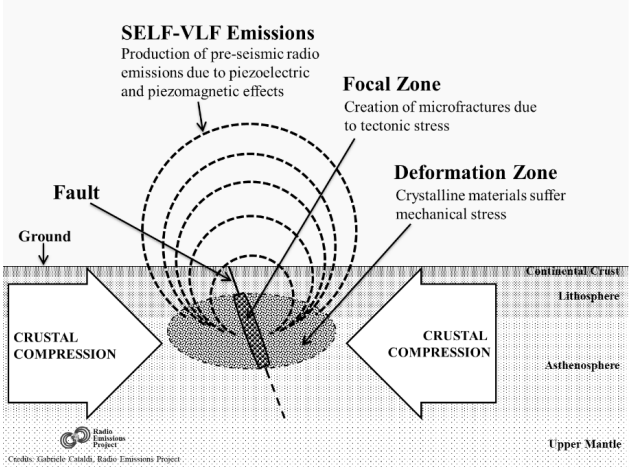

Figure 1. Pre-seismic radiofrequency is generated through the phenomenon of piezoelectricity. In the image above the geodynamic mechanism responsible for the pre-seismic radiofrequency emission has been represented. Credits: Gabriele Cataldi, Radio Emissions Project.

Other studies have shown that the volume of the earth's crust involved in the creation of microfractures is 24-520 times larger than the earthquake preparation zone [25].

The amplitude of the electromagnetic signals caused by the formation of microfractures of the rocks subjected to tectonic stress in the earthquake preparation area mainly depends on the density of the microfractures and their size; the morphology of the electromagnetic field depends on the orientation of the microfractures; on the other hand, the period of oscillation of the electromagnetic field (temporal modulation) depends on the geological characteristics of the fault and on the characteristics of the tectonic stress that determine a growth of the microfractures that does not proceed linearly [26].

According to T. Lay and T. C. Wallace only 1-10% of the energy and seismic moment contained in earthquake zones preparation is converted into seismic waves and it is therefore conceivable that the 90% (or more) of this energy, or part of it, can be converted to radiofrequency. Taking as a reference an earthquake of magnitude 5, this has an energy and a seismic moment between 10^{12} and 10^{18} Nm [27].

Considering that it is not possible to quantify the energy losses of the system in terms of thermody-

namic efficiency and the efficiency of energy conversion tectonic in other forms of energy, we assume that only 50% of the energy residual theorized by T. Lay and T. C. Wallace can be converted to radiofrequency [27].

2.2 Radon as a seismic precursor

The Radon gas is a chemical element that has been used for the first time as a seismic precursor in 1927 [28], but the first real recording that has had an important echo within the scientific community was realized following the Tashkent earthquake in 1966 [29]. Although the ICEF (International Commission on Earthquake Forecasting) has stated that it is obviously no significant correlation between the radon gas increases and seismic events; in our case the monitoring of the flow Rn_{222} has provided guidelines that were deemed correct, as confirmed by the RDF electromagnetic monitoring.

Certainly, the opinion ICEF does not contemplate the use of RDF technology confirming the creation of fractures in the subsurface, and this confirms that when using new media research, you can get unexpected results.

According to the authors, encouraging data about the use of radon as an imminent seismic activity indicator have been obtained, for example, against Radon gas flow measured before the M7.2 earthquake that was recorded in Kobe (Japan) on January 17, 1995 [1] (**Figure 2**).

Allegri and his team [31] and Pulinets and Boyarchuk [32] analyzed the flow of gas Radon in central Italy between 1979 and 1980 in the sites of Rome and Rieti experiencing between June and November 1980, an increase of +25% of the Radon flux and +170% of the baseline level, which preceded the M6.5 earthquake that was recorded in Irpinia (southern Italy) November 23, 1980 (**Figure 3**).

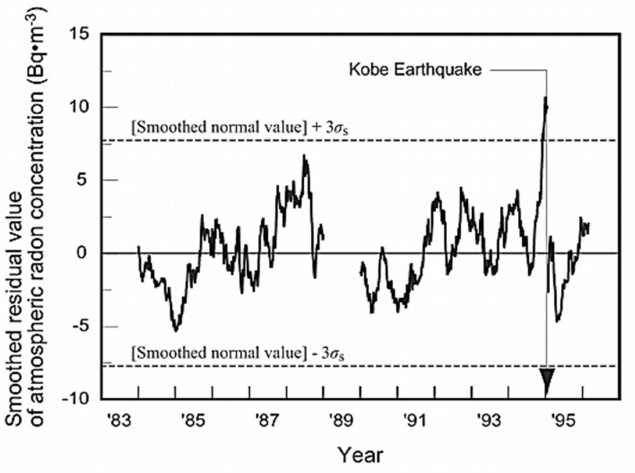

Figure 2. Radon gas concentration related to the M7.2 earthquake which was recorded in Kobe on January 17, 1995. In the graph above it is possible to observe the variation of the Radon gas concentration which preceded the M7.2 earthquake which was recorded in Kobe in 1995. Credits: Air radon concentration vs. time (by Kobe Pharmaceutical University) before the M = 7.2 Kobe earthquake of January 17, 1995 [29,30].

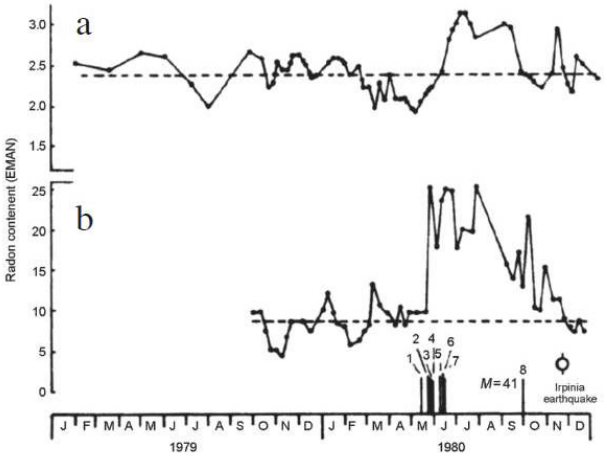

Figure 3. Radon gas concentration related to the M6.5 earthquake which was recorded in Irpinia (southern Italy) on November 23, 1980. In the graph above it is possible to observe the variation of the Radon gas concentration that preceded the M6.5 earthquake which was recorded in Italy in 1980. The 1979-1980 series of the groundwater radon content at: a) Rieti station, b) Rome station. The vertical bars in the bottom panel show the seismic shocks. The length of the bars is proportional to the magnitude (modified from Pulinets and Boyarchuk [10]).

3. Results

A total of 36 events occurred in the last century in Italy, that is, since 1920, were considered for the present research. The data are summarized in **Tables 1 and 2** and are broken down into 17 earthquake swarms and 19 earthquakes, of which 17 were destructive **Table 1**:

Below are the maps of the geographical areas

Table 1. Comparison of seismic swarms and intense weather events considered in Italy since 1927 and their respective occurrence intervals.

N.	Date of swarms start	Lat.	Long.	Main shock magnitude (Mw)	Area	Interval between earthquake and precipitation (in days) in the same area	Duration of meteorological events (days)
1	1927-1928	44.538584	9.648097	5.30	Bedonia, Alta Valterno, Italy	0	0
2	18/01/1990	39.115505	16.853912	4.00	Calabria, Crotone, Italy	0	2
3	26/09/1997	42.819109	13.184194	5.70	Appennino Umbro-Marchigiano, Italy	0	0
4	21/08/2000	44.889056	8.399895	4.90	Quattordio, Italy	0	0
5	18/11/2003	38.147984,	13.394317	5.60	Palermo, Italy	0	2
6	09/10/2004	39.904635	16.186023	4.20	Pollino, Italy	0	20
7	16/10/2008	42.387694	13.397661	4.60	L'Aquila, Italy	0	15
8	20/05/2012	44.826673	11.212160	6.10	Emilia Romagna, Italy	0	15
9	24/08/2016	42.497640	13.408839	6.00	Appennino Centrale, Italy	0	90
10	18/01/2020	42.625285	13.287986	4.20	Amatrice, Italy	0	20
11	24/05/2020	37.748736	15.007888	4.60	Etna, Italy	0	0
12	18/01/2021	37.766478	15.011280	4.10	Etna, Italy	0	15
13	31/07/2021	44.061205	12.601903	2.20	Rimini, Italy	0	0
14	22/03/2022	43.291692	12.318422	4.30	Umbertide, Italy	0	0
15	18/03/2022	40.842690	14.138801	2.00	Campi Flegrei, Italy	0	2
16	09/11/2022	43.503222	13.320910	5.70	Ancona, Pesaro, Macerata, Italy	7	15
17	28/05/2023	37.724041	15.118004	4.00	Milo, Italy	0	0

where the seismic swarms listed in **Table 1** occurred. Of these maps, one of the seismic swarms that occurred between 1927 and 1928 is missing, because this data, although witnessed, is not present in the archives of the INGV—National Institute of Geophysics and Volcanology, an archive where the data on the earthquakes in question have been extrapolated (**Figures 4-19**).

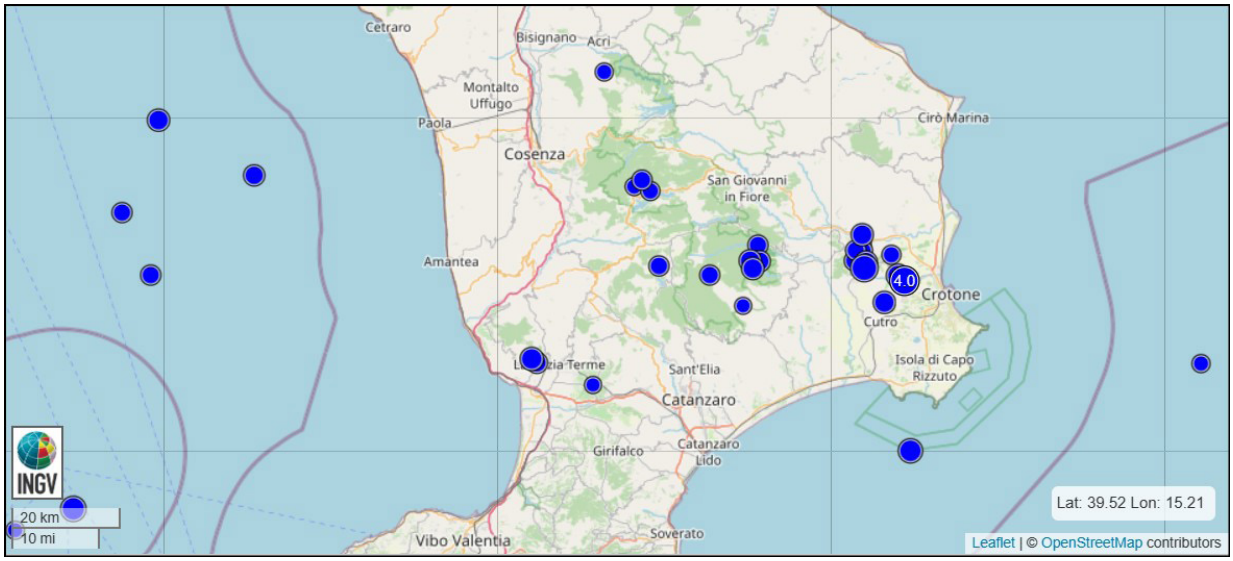

Figure 4. Earthquake swarm of January 18, 1990.

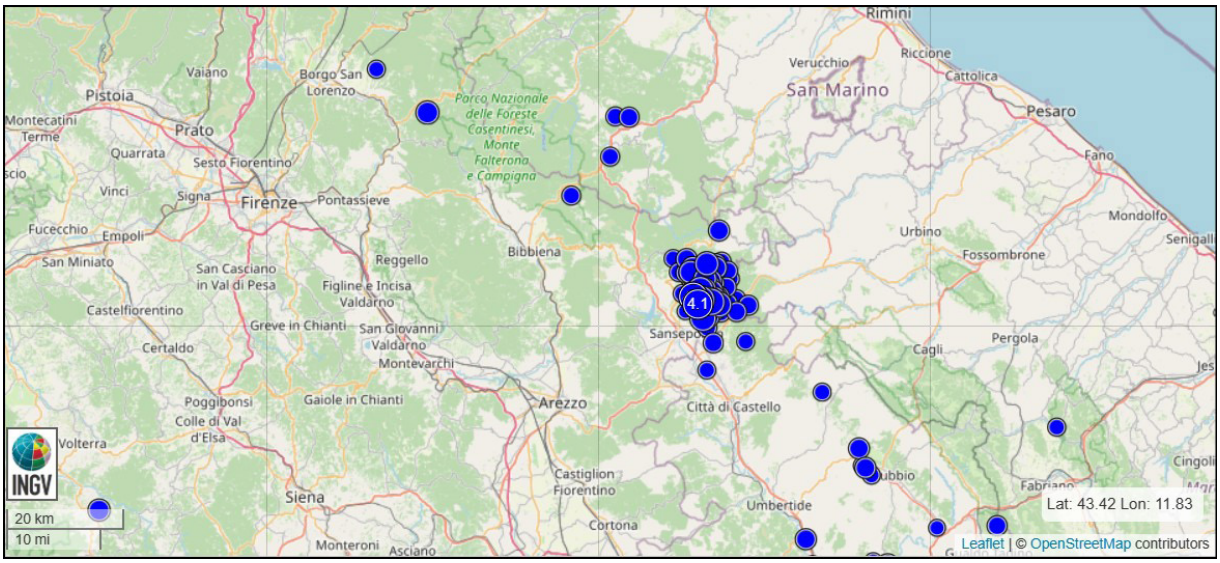

Figure 5. Earthquake swarm of September 29, 1997.

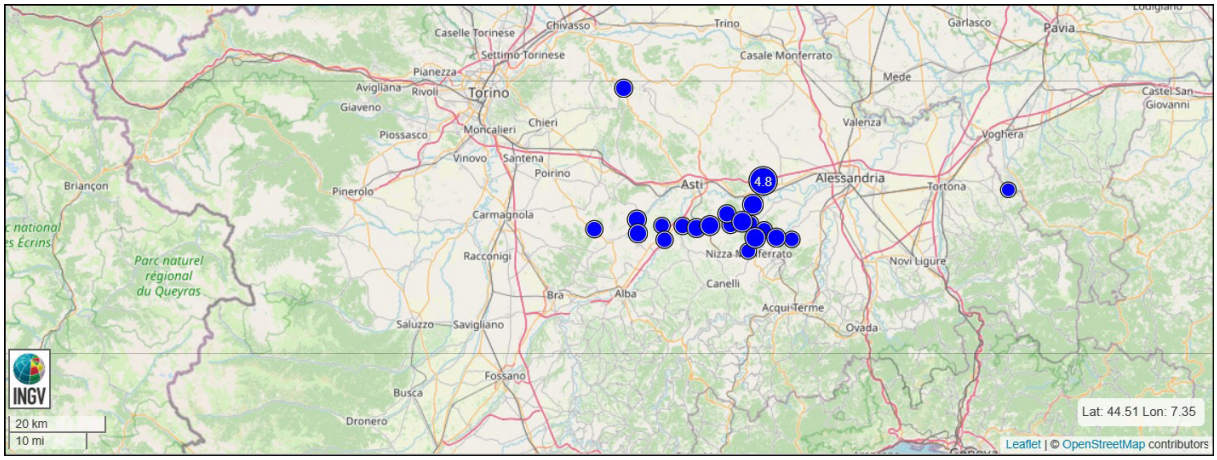

Figure 6. Earthquake swarm of August 21, 2000.

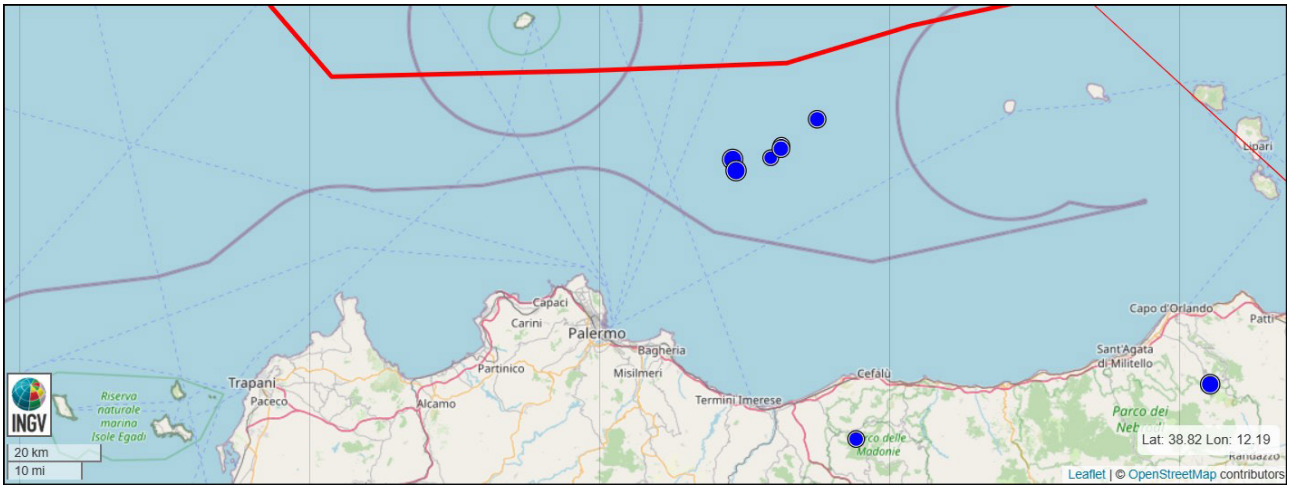

Figure 7. Earthquake swarm of November 18, 2003.

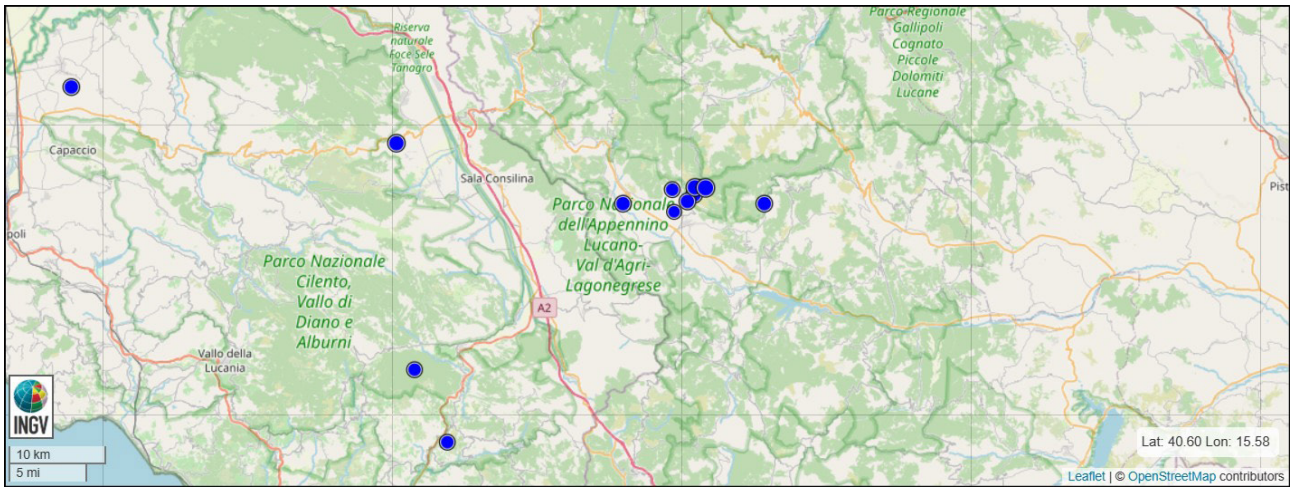

Figure 8. Earthquake swarm of October 9, 2004.

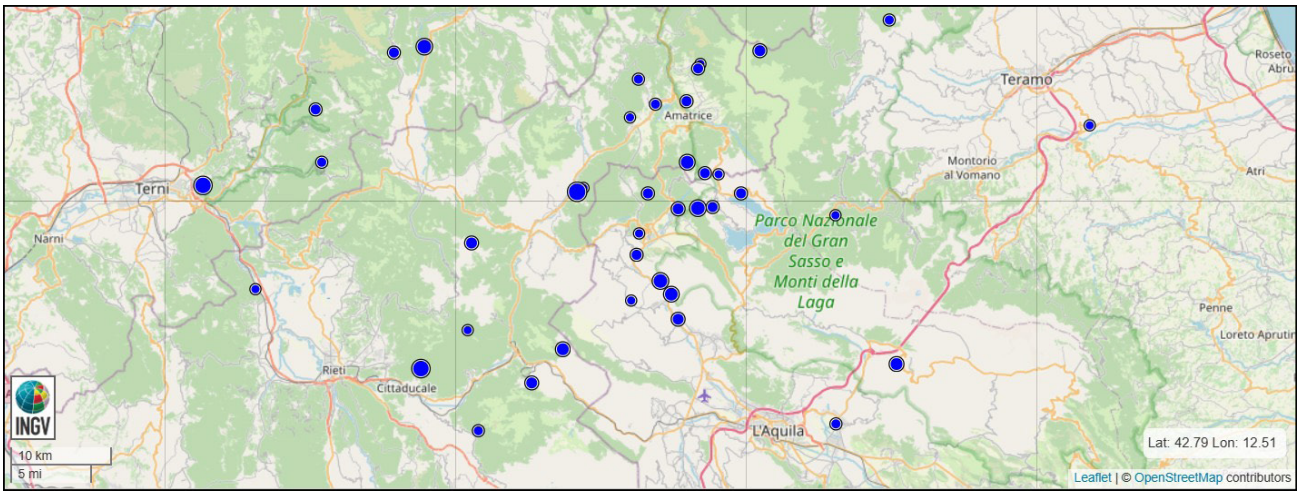

Figure 9. Earthquake swarm of October 16, 2008.

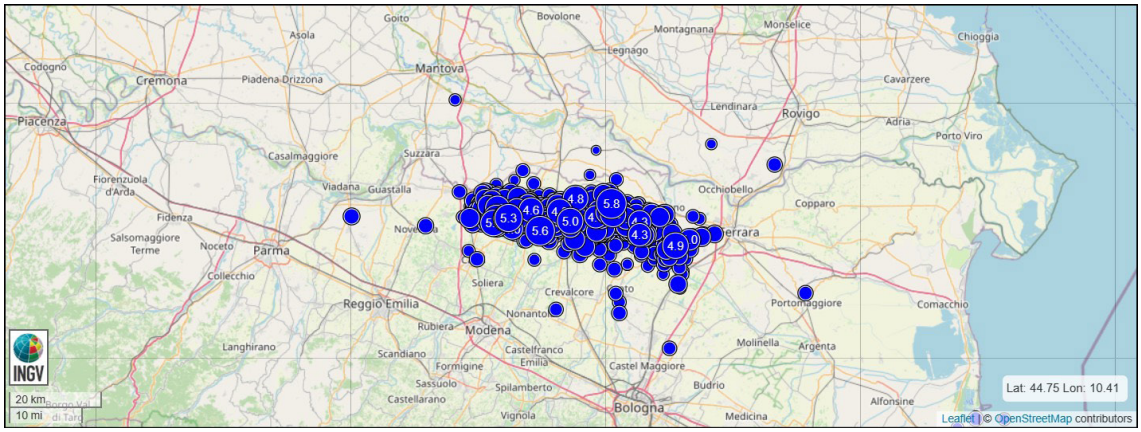

Figure 10. Earthquake swarm of May 20, 2012.

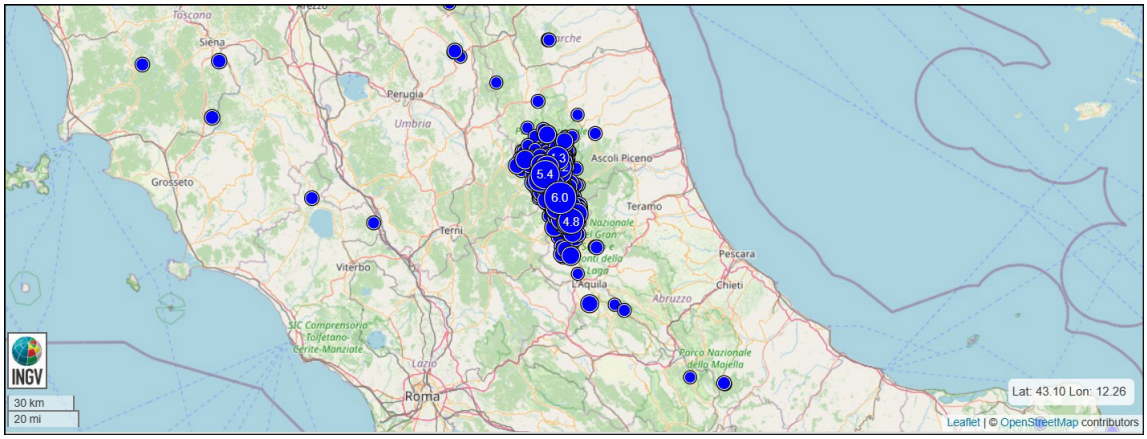

Figure 11. Earthquake swarm of August 24, 2016.

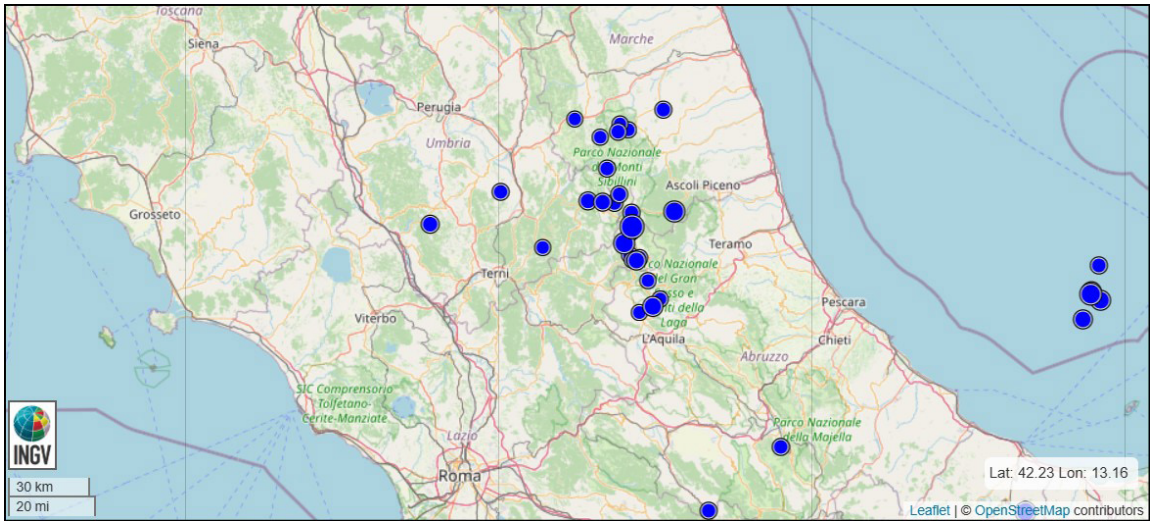

Figure 12. Earthquake swarm of January 18, 2020.

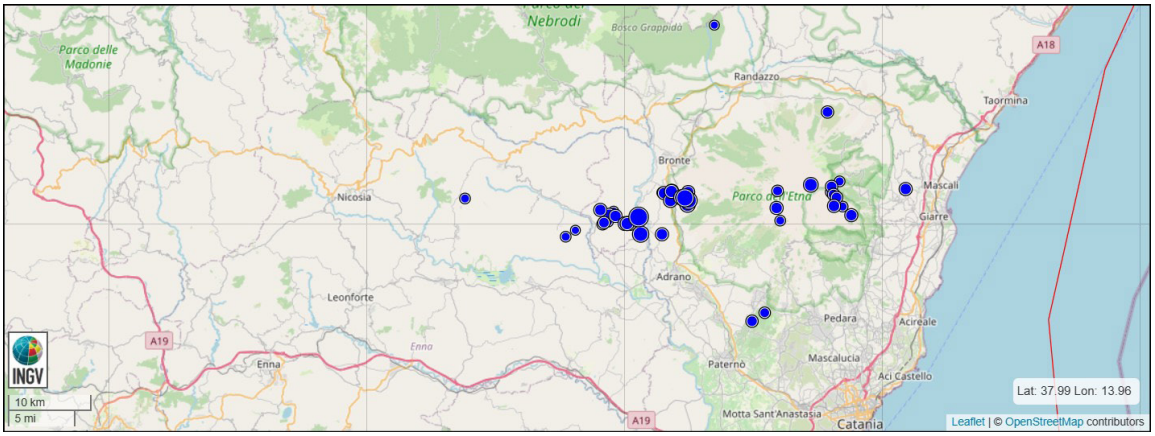

Figure 13. Earthquake swarm of May 24, 2020.

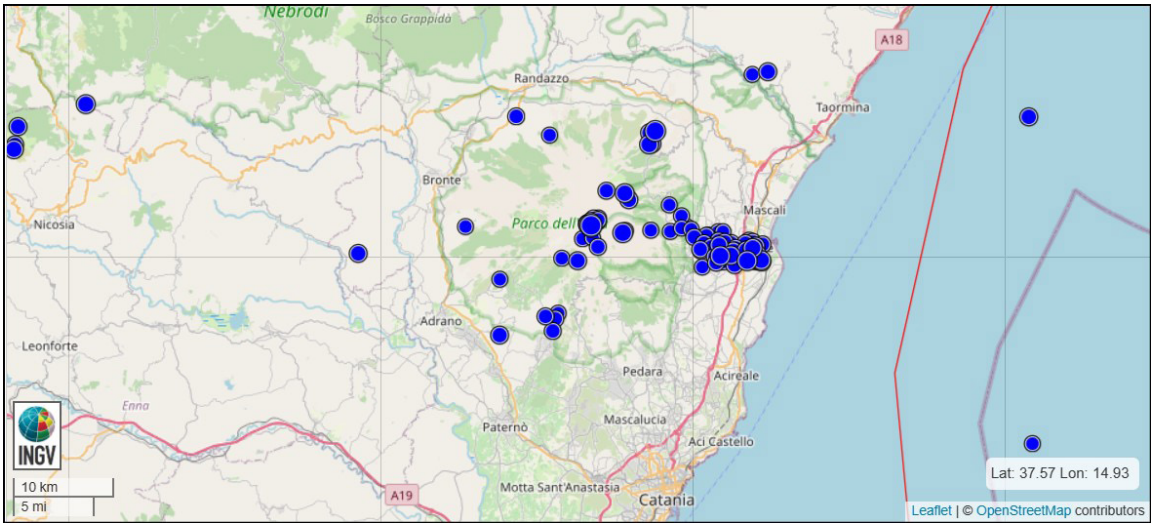

Figure 14. Earthquake swarm of January 18, 2021.

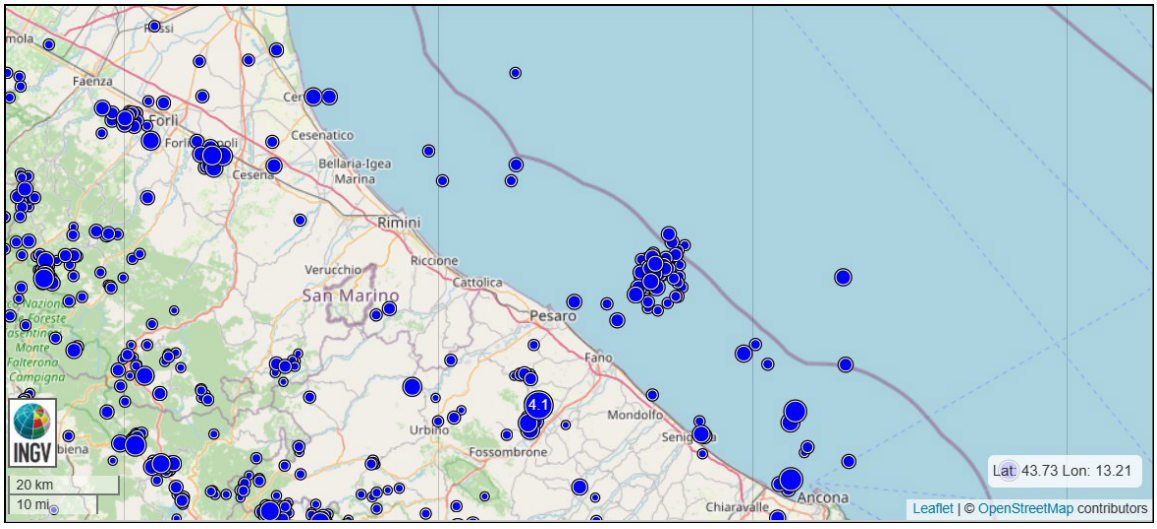

Figure 15. Earthquake swarm of July 31, 2021.

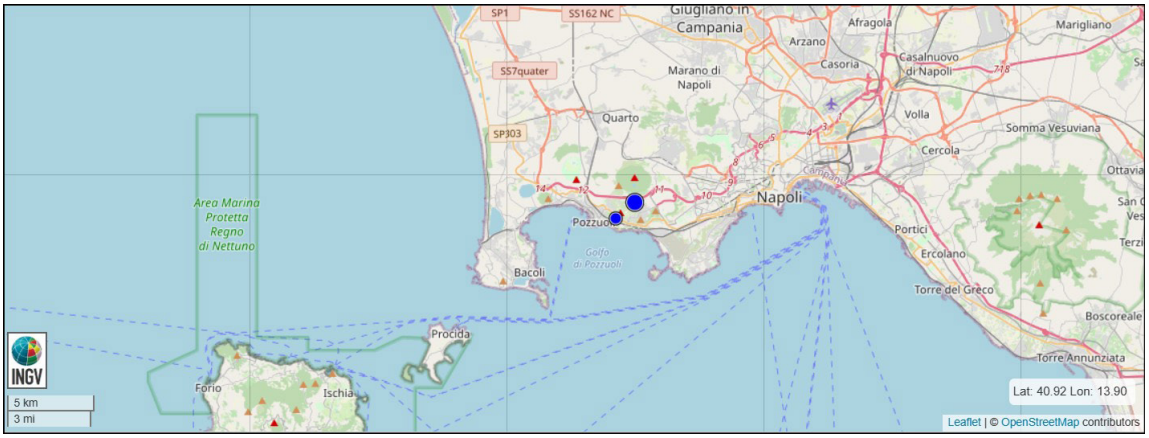

Figure 16. Earthquake swarm of March 18, 2022.

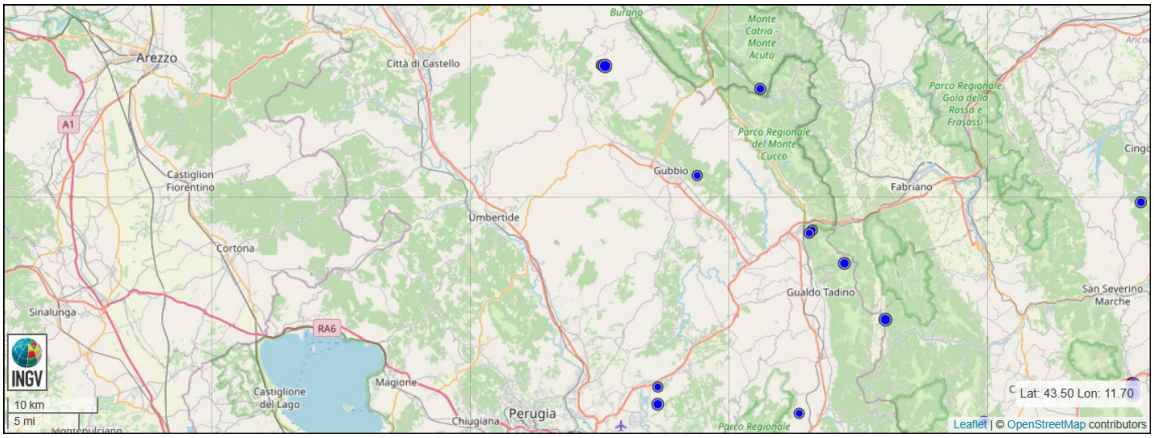

Figure 17. Earthquake swarm of March 22, 2022.

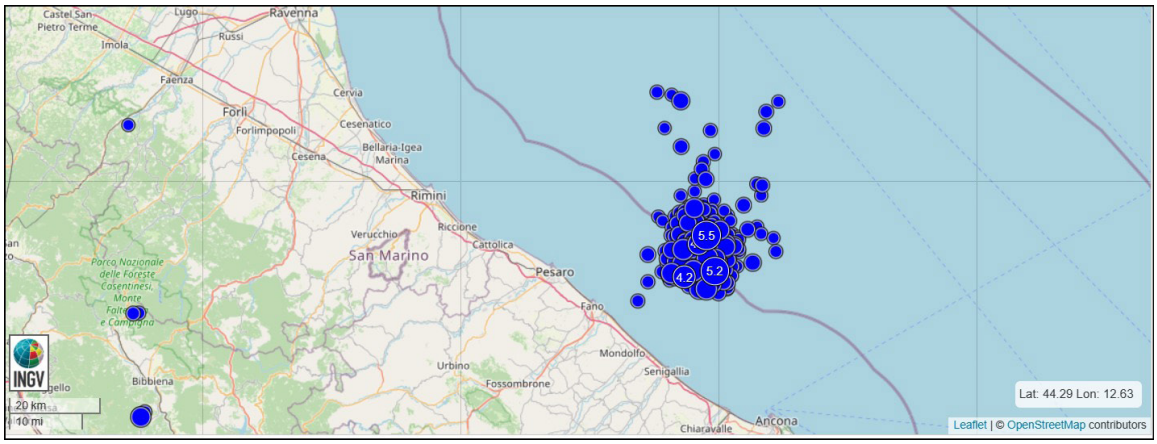

Figure 18. Earthquake swarm of 9 November, 2022.

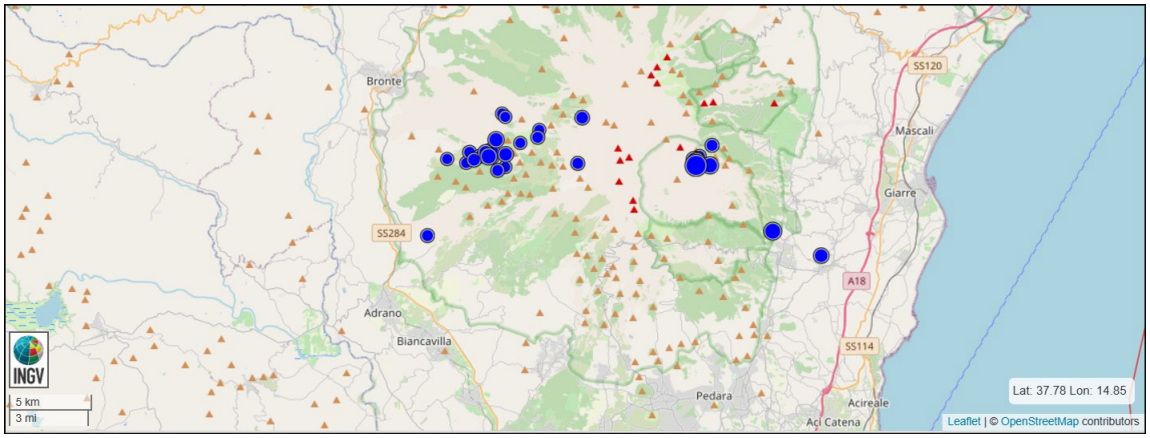

Figure 19. Earthquake swarm of May 28, 2023.

Table 2. Comparison of destructive earthquakes that have occurred in Italy since 1920 the duration of meteoric events and their respective intervals of occurrence.

N.	Swarms start	Lat.	Long.	Main shock (Mw)	Zone (Italy)	Interval between earthquake and precipitation (days)	Meteorological events (days)
1	08/09/1920	44.058	10.395	6.3	Molazzana	0	10
2	23/07/1930	40.980	25.341	6.6	Bisaccia Nuova	0	10
3	21/08/1962	41.175	15.009	6.2	Montecalvo Irpino	0	10
4	19/07/1963	43.343	08.153	6.3	San Lorenzo al Mare	0	10
5	19/07/1963	43.344	08.278	6.1	San Lorenzo al Mare	0	10
6	15/01/1968	37.745	12.997	6.0	Salaparuta	0	3
7	06/05/1976	46.356	13.275	6.5	Prato	0	10
8	17/06/1976	46.162	12.864	6.1	Lestans	0	10
9	15/09/1976	46.302	13.197	6	Isola	0	0
10	23/11/1980	40.914	15.366	6,9	Cairano	0	0
11	26/09/1997	43.084	12.812	6	Nocera Umbra	0	0
12	06/09/2002	38.381	13.701	6	Santa Flavia	0	1
13	06/04/2009	42.334	13.334	6.3	Sassa	2	1
14	20/05/2012	44.890	11.230	6	Massa Finalese	2	1
15	27/05/2012	44.814	11.115	6.3	Medolla	0	0
16	17/01/2016	41.558	14.603	7	Campobasso	0	1
17	24/08/2016	42.723	13.187	6.2	Accumuli	2	15
18	26/10/2016	42.956	13.066	6.1	Visso	0	1
19	30/10/2016	42.862	13.096	6.6	Preci	0	1

In **Figures 4-19**, the extensions of seismic swarms concerning the Italian territory can be observed.

4. Discussion

Italian chronicles from the past century, as well as others around the world, report earthquake events generally followed by various types of precipitation, such as rain, snow, or hail, even with repeated occurrences for weeks, as shown in **Tables 1 and 2**. **Figures 20 and 21** display the association between the two events; generally, on a time scale, physical shaking occurs first and then precipitation occurs. At least in the cases considered in Italy.

In the first case, seismic swarms were considered (**Table 1**), and considering that swarms are characterized by a succession of earthquakes of varying magnitude without depending on an earthquake of greater energy and lasting even months, as in the case of the seismic crisis that affected the Northwest Apennines, between 1927 and 1928 [35]. In this context, it is therefore very difficult to indicate the duration of the meteorological event and the time interval between it and the seismic event since we are talking about the succession of earthquakes lasting several days and, in some cases, several months. Thus, we referred to the date of onset as opposed to the total duration of the earthquake swarm, which extended up to a maximum time interval of 90 days. Within these limits, the interaction between lithosphere and atmosphere, discussed in this study was respected for all earthquakes analyzed.

The second case examined destructive earthquakes that occurred in the last century in Italy. The data are summarized in **Table 2** and report single earthquake events of potentially destructive magnitude. In this analysis, reference is made, to general weather conditions, in which storms, rain, drought, cold/freeze or stable conditions can be found, with respect to the date of occurrence of the main quake. The reference period is represented by the date of the event itself and its geographical location. In the discussion of the data (**Figure 21**), we have considered the areal extent of weather events, as their geographical extent sometimes extends beyond the geographical limits of the epicentres of the earthquake events examined.

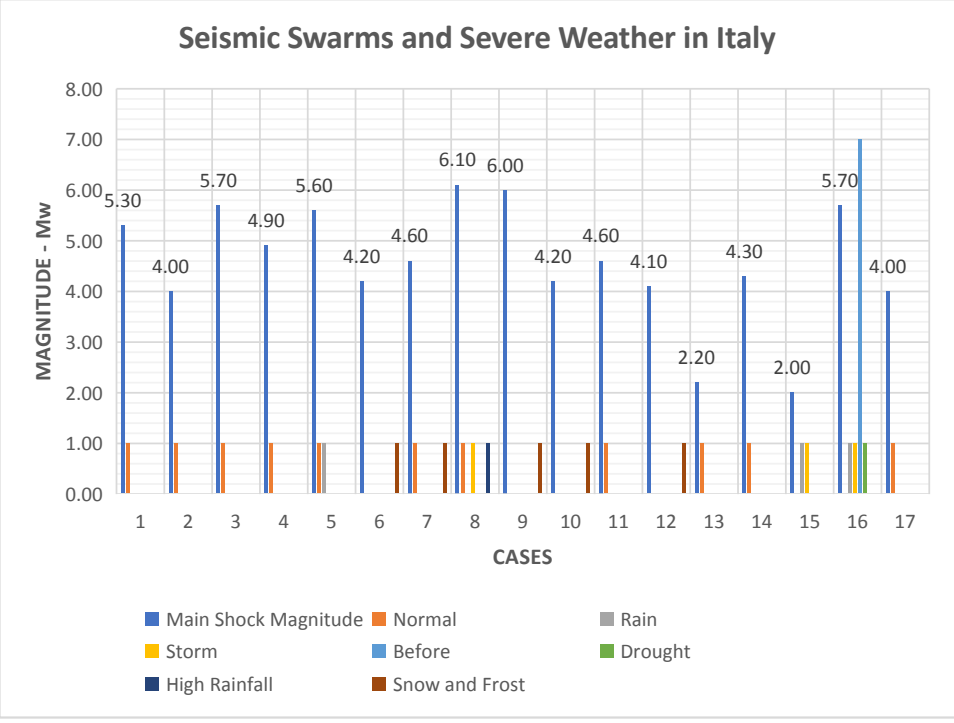

Figure 20. Comparison of seismic swarms and meteoric precipitation of various kinds that have occurred in Italy since 1927 (see **Table 1**).

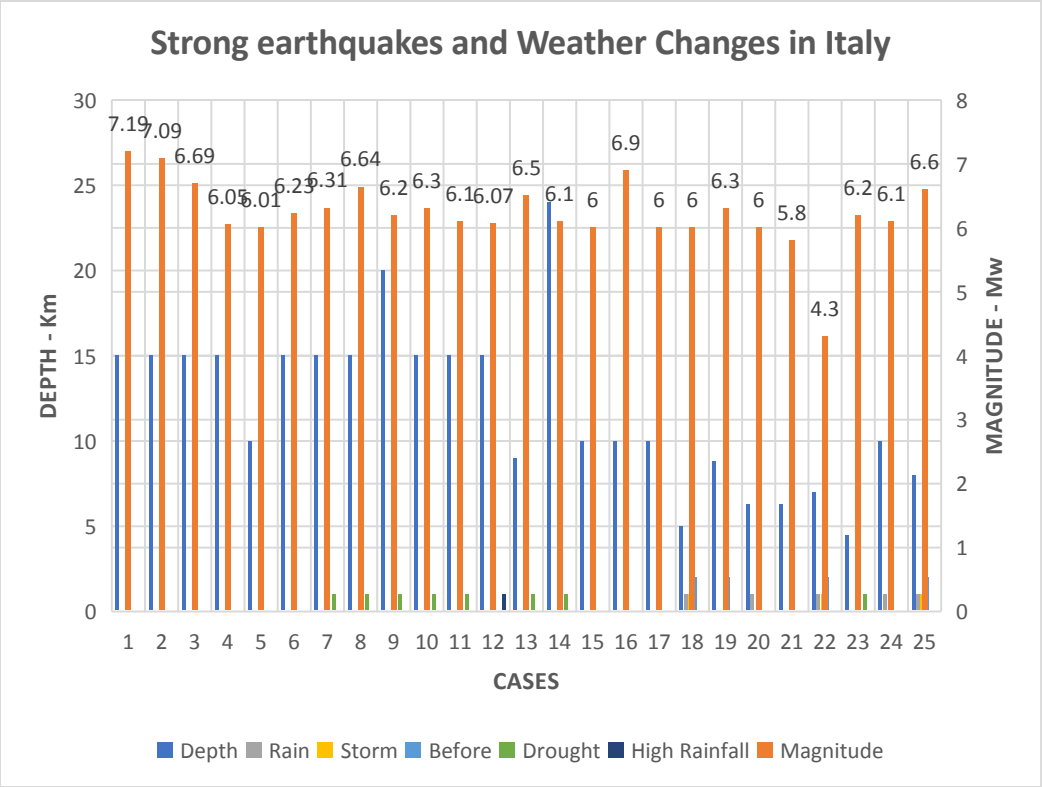

Figure 21. Meteoric events of various kinds and different intensities are associated with earthquakes of magnitude 6 or greater, except for two cases of magnitude 5.8 and 4.3, which have occurred in Italy since 1920 (see **Table 2**).

The recurrence between geophysical and hydro-climatic events, whether earthquake swarms or destructive earthquakes, allowed us to advance, at the level of hypothesis, the potential link between the two phenomena.

The first mechanism involves water condensation nuclei. They are transported by both radon gas, released from the ground in the pre-seismic and seismic phases on atmospheric gases, and cosmic rays in the upper atmosphere, generated by air ionization [34-37]. Radon gas, trapped in the lithosphere, is released in pre-seismic phases and during the main shaking in areas under tectonic stress. The release of the gas into the atmosphere increases its ionizing effect in the air, in agreement with the model proposed by Pulinets et al. [1].

A second mechanism not yet fully understood in the troposphere has been studied by Wu in recent work, concerning "jet streams" [38]. According to the author, these atmospheric streams would be influenced by the charges released from the subsurface and intercept in the pre-seismic phases the area of the area of the future epicentre a few days before the main shock [39-42].

5. Conclusions

The question we have tried to answer in this paper is whether there can be a direct relationship between earthquakes, precipitation, and extreme weather events, and what common denominator connects them. The answer is affirmative. The potential candidate is tectonic stress with which is associated the release of charges in fault zones close to rupture, responsible for the formation of water cores. Interdisciplinary studies may or may not confirm the repetition of extreme hydro-climatic events in other parts of the world to make long-term predictions. In fact, today, thanks to modern instruments, the use of satellites and interdisciplinary teamwork, the analysis of hydro-climatic phenomena can be assessed with a holistic approach, that is, considering anthropogenic impact, geophysical events, and radiation from space. The outcome of this study, which associates

earthquakes and seismic swarms with even extreme weather events and vice versa, can be considered in agreement with those of other authors who have analysed the interaction between the two physical and geophysical phenomena in various seismically active areas of the world [43-47].

Author Contributions

Valentino Straser has the main responsibility, and initiative based on several years of study of seismic precursors, especially in the electromagnetic field. The co-authors supported the present study with data collection.

Conflict of Interest

The author and co-authors declare that they have no conflicts of interest.

Funding

This research received no external funding.

References

[1] Straser, V., Giuliani, G., Cataldi, D., et al., 2020. Multi-parametric investigation of preseismic origin phenomena through the use of RDF technology (Radio Direction Finding) and the monitoring of radon gas stream (Rn 222). New Concepts Geoplasma Journal. 8(1), 11-27.

[2] Leybourne, B., Straser, V., Gregori, G., et al. (editors), 2019. North American solar electro-magnetic induction detection network. Proceeding of the 13th World Multi-Conference on Society, Cybernetics and Informatics (WMSCI); 2019 Jul 8; Orlando, Florida, USA.

[3] Leybourne, B., 2018. Stellar transformer concepts: Solar induction driver of natural disasters—Forecasting with geophysical intelligence. Systemics, Cybernetics and Informatics. 16(4), 26-37.

[4] Svensmark, H., Enghoff, M.B., Shaviv, N.J., et al., 2017. Increased ionization supports growth of aerosols into cloud condensation nuclei. Nature Communications. 8, 2199. DOI: https://doi.org/10.1038/s41467-017-02082-2

[5] Straser, V., Casati, M., Cataldi, G. (editors), 2016. "Water bombs" and seismic areas: Two sides to the same problem? EGU General Assembly 2016; 2016 Apr 17-22; Vienna, Austria.

[6] Straser, V., 2015. A potential relationship between seismic swarm and violent rainstorm? New Concepts in Global Tectonics Journal. 3(4), 467-475.

[7] Ondoh, T., 2004. Anomalous sporadic-E ionization before a great earthquake. Advances in Space Research. 34(8), 1830-1835.

[8] Kuang, C., McMurry, P.H., McCormick, A.V., 2009. Determination of cloud condensation nuclei production from measured new particle formation events. Geophysical Research Letters. 36(9).

[9] Pulinets, S., Ouzounov, D., 2011. Lithosphere-Atmosphere-Ionosphere Coupling (LAIC) model—An unified concept for earthquake precursors validation. Journal of Asian Earth Sciences. 41(4-5), 371-382.

[10] Pulinets, S., Boyarchuk, K., 2004. Ionosphere precursors of earthquake. Springer: Berlin.

[11] Svensmark, H., Friis-Christensen, E., 1997. Variation of cosmic ray flux and global cloud coverage—a missing link in solar-climate relationships. Journal of Atmospheric and Solar-Terrestrial Physics. 59(11), 1225-1232.

[12] Martinez, J.M., Andrè, P., Courty, M.A. (editors), 2017. Lightning process viewed trough the properties plasma nanocomposites formed by laboratory electric discharge. Proceding 2nd International Symposium on Lightning and Storm Related Phenomena. 2017 May 10-11; Aurillac, France.

[13] Courty, M.A., Martinez, J.M., 2015. Terrestrial carbonaceous debris tracing atmospheric hypervelocity-shock aeroplasma processes. Procedia Engineering. 103, 81-88.

[14] Milne, J., 1890. Earthquakes in connection with electric and magnetic phenomena. Transactions of the Seismological Society of Japan. 15,

135-162.

[15] Wang, J.H., 2021. Piezoelectricity as a mechanism on generation of electromagnetic precursors before earthquakes. Geophysical Journal International. 224(1), 682-700.

[16] Finkelstein, D., Hill, R.D., Powell, J.R., 1973. The piezoelectric theory of earthquake lightning. Journal of Geophysical Research. 78(6), 992-993.

[17] Freund, F., 2002. Charge generation and propagation in igneous rocks. Journal of Geodynamics. 33(4-5), 543-570.

[18] Brace, W.F., Paulding Jr, B.W., Scholz, C.H., 1966. Dilatancy in the fracture of crystalline rocks. Journal of Geophysical Research. 71(16), 3939-3953.

[19] Scholz, C.H., 2002. The mechanics of earthquakes and faulting. Cambridge University Press: Cambridge. pp. 471.

[20] Aviles, C.A., Scholz, C.H., Boatwright, J., 1987. Fractal analysis applied to characteristic segments of the San Andreas fault. Journal of Geophysical Research: Solid Earth. 92(B1), 331-344.

[21] Power, W.L., Tullis, T.E., Brown, S.R., et al., 1987. Roughness of natural fault surfaces. Geophysical Research Letters. 14(1), 29-32.

[22] Chester, F.M., Chester, J.S., 2000. Stress and deformation along wavy frictional faults. Journal of Geophysical Research: Solid Earth. 105(B10), 23421-23430.

[23] Wilson, J.E., Chester, J.S., Chester, F.M., 2003. Microfracture analysis of fault growth and wear processes, Punchbowl Fault, San Andreas system, California. Journal of Structural Geology. 25(11), 1855-1873.

[24] Faulkner, D.R., Mitchell, T.M., Jensen, E., et al., 2011. Scaling of fault damage zones with displacement and the implications for fault growth processes. Journal of Geophysical Research: Solid Earth. 116(B5).

[25] Sgrigna, V., Buzzi, A., Conti, L., et al., 2007. Seismo-induced effects in the near-earth space: Combined ground and space investigations as a contribution to earthquake prediction. Tectonophysics. 431(1-4), 153-171.

[26] Surkov, V.V., Molchanov, O.A., Hayakawa, M., 2003. Pre-earthquake ULF electromagnetic perturbations as a result of inductive seismomagnetic phenomena during microfracturing. Journal of Atmospheric and Solar-Terrestrial Physics. 65(1), 31-46.

[27] Lay, T., Wallace, T.C., 1995. Modern global seismology. Academic Press: Cambridge. pp. 521.

[28] Shiratoi, K., 1927. The variation of radon activity of hot spring. Scientific Report of Tohoku Imperial University. 3(16), 614-621.

[29] Riggio, A., Santulin, M., 2015. Earthquake forecasting: A review of radon as seismic precursor. Bollettino Di Geofisica Teorica e Applicata. 56(2), 95-114.

[30] Kawada, Y., Nagahama, H., Omori, Y., et al., 2007. Time-scale invariant changes in atmospheric radon concentration and crustal strain prior to a large earthquake. Nonlinear Processes in Geophysics. 14(2), 123-130.

[31] Allegri, L., Bella, F., Della Monica, G., et al., 1983. Radon and rilt anomalies detected before the Irpinia (south Italy) earthquake of November 23, 1980 at great distances from the epicenter. Geophysical Research Letters. 10(4), 269-272. DOI: https://doi.org/10.1029/GL010i004p00269

[32] Pulinets, S.A., Biagi, P.F., Tramutoli, V., et al., 2007. Irpinia earthquake 23 November 1980: lesson from Nature revealed by joint data analysis. Annals of Geophysics. 50(1), 61-78.

[33] Straser, V., 2021. Un nido di terremoti. Mille anni di Storia sismica in Val Taro e Val Ceno (Italian) [A nest of earthquakes. One thousand years of seismic history in the Taro and Ceno Valleys]. Monte Università di Parma: Parma PR. pp. 191.

[34] Garavaglia, M., Dal Moro, G., Zadro, M., 2000. Radon and tilt measurements in a seismic area: temperature effects. Physics and Chemistry of the Earth, Part A: Solid Earth and Geodesy. 25(3), 233-237.

[35] Heinicke, J., Koch, U., Martinelli, G., 1995. CO2 and radon measurements in the Vogtland Area (Germany)—A contribution to earthquake prediction research. Geophysical Research Letters. 22(7), 771-774.

[36] Omori, Y., Yasuoka, Y., Nagahama, H., et al., 2007. Anomalous radon emanation linked to preseismic electromagnetic phenomena. Natural Hazards and Earth System Sciences. 7(5), 629-635.

[37] Cataldi, D., Giuliani, G.G., Straser, V., et al., 2020. Radio signals and changes flow of Radon gas which led to the seismic sequence and the earthquake magnitude Mw 4.4 that has recorded in Central Italy (Balsorano, l'Aquila) on November 7, 2019. New Concepts in Geoplasma Tectonics Journal. 8(1), 32-42.

[38] Wu, H.C., Leybourne, B. (editors), 2020. Using jet stream's precursors to make earthquake forecast. 11th International Multi-Conference on Complexity, Informatics and Cybernetics; 2020 Mar 10-13; Orlando, Florida, U.S.A.

[39] Wang, J.H., 2021. Piezoelectricity as a mechanism on generation of electromagnetic precursors before earthquakes. Geophysical Journal International. 224(1), 682-700.
DOI: https://doi.org/10.1093/gji/ggaa429

[40] Straser, V., Cataldi, D., Cataldi, G., 2023. Radio direction finding method to mitigate tsunami risk in Sierra Leone. Advances in Geological and Geotechnical Engineering Research. 5(2), 64-75.
DOI: https://doi.org/10.30564/agger.v5i2.5617

[41] Nahornyi, V., Straser, V., Cataldi, D., 2022. Prediction of the vibration moment of Mount Etna based on electromagnetic signal monitoring. MM Science Journal. 5943-5948.

[42] Panda, A., Nahornyi, V., Straser, V., et al., 2021. Forecasting an vibration by monitoring the dynamics of changes its precursors of various physical nature. MM Science Journal. 4396-4399.
DOI: https://doi.org/10.17973/MMSJ.2021_6_2021019

[43] Zhao, D., Chen, L., Yu, Y., 2021. Associations between strong earthquakes and local rainfall in China. Frontiers in Earth Science. 9, 760497.
DOI: https://doi.org/10.3389/feart.2021.76049.7

[44] Mansouri Daneshvar, M.R., Khosravi, M., Tavousi, T., 2014. Seismic triggering of atmospheric variables prior to the major earthquakes in the Middle East within a 12-year time-period of 2002-2013. Natural Hazards. 74, 1539-1553.
DOI: https://doi.org/10.1007/s11069-014-1266-5

[45] Huang, L.S., McRaney, J., Teng, T.L., et al., 1979. A preliminary study on the relationship between precipitation and large earthquakes in Southern California. Pure and Applied Geophysics. 117, 1286-1300.
DOI: https://doi.org/10.1007/BF00876220

[46] Guo, G., Wang, B., 2008. Cloud anomaly before Iran earthquake. International Journal of Remote Sensing. 29(7), 1921-1928.
DOI: https://doi.org/10.1080/01431160701373762

[47] Goswami, H., Devi, M., Rambabu, S., et al., 2014. An analysis of the relation between precipitation and earthquake in the Indian region. Indian Journal of Radio and Space Physics. 43(1), 41-47.

BILINGUAL PUBLISHING GROUP

Advances in Geological and Geotechnical Engineering Research

https://ojs.bilpublishing.com/index.php/agger

ARTICLE

Investigation of Physicochemical Properties of Qalay Abdul Ali Soil, Kabul, Afghanistan

***Hafizullah Rasouli*[1*], *Ashok Vaseashta*[2*]**

[1] *Department of Geology, Geoscience Faculty, Kabul University, Jamal Mina 1006, Kabul, Afghanistan*

[2] *Applied Research, International Clean Water Institute Manassas, VA, 20108-0258, USA*

ABSTRACT

The article presents the physicochemical properties of soil from six different areas in Qalay Abdul Ali, Kabul, Afghanistan. The authors collected dissimilar samples from six diverse areas, each with a unique profile identifier, and transported them to the research laboratory. The key objectives of this study are to recognize and profile such areas in terms of their physical and chemical characteristics and correlate them with the earlier geological periods of the Qalay Abdul Ali Region. Due to regional conflicts in the region, such quantifications are necessary as very limited data for this region existed. From the analysis, the authors assess that the soil type is gravely soil, and silt with gravels with mostly neutral pH of the soil, although, in specific regions, it was near-acidic. The amounts of $CaCO_3$, EC (electroconductivity), and pH are dissimilar according to the locations, the values of EC, and pH within a normal range at whole locations, and the remnants of plants in various quantities. These observations recommend that the soil limitations can be used accordingly for the utilization of soil factors in the regions of the study sites and extra washbasins in the country. As the population continues to grow, such data will be critical to the future sustainability of this region.

Keywords: Geology; Topsoil profiles; Physicochemical limitations; Qalay Abdul Ali; Kabul Basin

1. Introduction

The Kabul Province is surrounded by a series of high mountains, with the maximum height reaching up to ~4,522 m in elevation toward the west of the study area. Koh-e Safi, a major historical district, lo-

*CORRESPONDING AUTHOR:

Hafizullah Rasouli, Department of Geology, Geoscience Faculty, Kabul University, Jamal Mina 1006, Kabul, Afghanistan; Email: hafizullah.rasouli133@gmail.com

Ashok Vaseashta, Applied Research, International Clean Water Institute Manassas, VA, 20108-0258, USA; Email: prof.vaseashta@ieee.org

ARTICLE INFO

Received: 9 June 2023 | Revised: 27 July 2023 | Accepted: 31 July 2023 | Published Online: 16 August 2023

DOI: https://doi.org/10.30564/agger.v5i3.5773

CITATION

Rasouli, H., Vaseashta, A., 2023. Investigation of Physicochemical Properties of Qalay Abdul Ali Soil, Kabul, Afghanistan. Advances in Geological and Geotechnical Engineering Research. 5(3): 55-68. DOI: https://doi.org/10.30564/agger.v5i3.5773

COPYRIGHT

Copyright © 2023 by the author(s). Published by Bilingual Publishing Group. This is an open access article under the Creative Commons Attribution-NonCommercial 4.0 International (CC BY-NC 4.0) License. (https://creativecommons.org/licenses/by-nc/4.0/).

cated in South-Eastern Parwan Province, has an elevation of approx. 2,816 m above sea level. The region of Qalay Abdul Ali Soil, Kabul, is to the west of our area of investigation [1,2] with the sedimentary formation ranging from approximately 200-500 m above the neighboring valleys and gorge bottoms. The heights of the series of central plateaus start at about 1,800 m in the adjacent main basins to 2,200 m in Paghman and Higher Kabul Sub-basins [3]. From the north and at the source in the Smaller Himalayas [4], noticeable seal terraces were accumulated, perhaps throughout the late Pleistocene carved out [5]. The relief of stress creates an active balance between current tectonics and other ongoing processes [6]. The sharp stress relief in conjunction with the uplift rates in the upper Himalayas Regions reproduces pushing over the mean-crustal slope quite a potion the isostatic reaction to re-carving of the Tibetan Plateau determined by late Cenozoic macroclimate alteration, or late Miocene repetition of the key Dominant Thrust. The kinetics of highland textures result from the mixture of crustal distortion and loss, with the two processes being perhaps joined [7-9]. These processes along with anthropogenic activities resulting from years of regional conflict and growing population necessitate a physicochemical assessment of this region for safe and sustainable water resources.

Hence, one of the goals is to map out river terraces of the Kabul Province and assess the place of diverse mineral deposits in the region of interest for this investigation. For the present objective, all samples from these terraces were collected and carefully transported to the research laboratory for analysis to account for different minerals. Furthermore, almost every basin in Afghanistan is from the tertiary geological period (ioncene and oligocene), since it is surrounded by mountains that were formed around (20-45) million years ago and their residues are formed by tertiary creation. The higher portion of the Kabul Basins is also from this period [10]. The greater portion of these sediments is enclosed by terraces, and it becomes gradual at the lower quaternary (Pleistocene). The value of these deposits is correlated to the neighboring peaks. The Kabul Province is a part of the structurally dynamic Kabul mass in the transferred platter border section of the country [11]. Afghanistan lies along a highly active plate region that has formed the world's highest peaks, viz. the Himalayas, Karakoram, Pamir, and the Hindu Kush. In Kabul, due to the tectonic movement of mountains, different sections consist of composites of displaced materials, viz. bottomless Gneiss Graben was designed and occupied by hundreds of meters of river sediments, sediments by gravity, and lake deposits [12]. The greatest sediment thus Neogen is enclosed by the medium quaternary and currently, a large portion is soft, and these sediments are protected by the alluvial of the upper quaternary. A smaller portion of these districts is positioned at the bottomless area of Tangi Mahipar (800 m a.s.l) and the maximum section of these areas is placed at the upper Kabul Mountain Series (up from 4,522 m a.s.l). The gorges of rivers form V and U shapes. Usually, the capital [13], involves gravel formations, and its width is changed from region to region. Bagrami Hill, Maranjan Hill, Bibi Mahrow Hill, and Kalola Pushta Hill are sited in the catchment, which is associated with the tertiary geological time scale, and whole remnants of dissimilar Kabul Basin regolith [14,15]. The neighboring elevations are mainly composed of Paleoproterozoic gneiss and Late Permian through Late Triassic rocks. The inter-basin edges which are collected of metamorphic core-complex rocks, are Paleoproterozoic gneiss. Underground basements in the Safi Mountains, to the east of the Kabul Basin, are Paleoproterozoic gneiss and migmatite of the Sherdarwaza Sequences and low-grade schist and quartzite of the Walayati Series. The underground is superimposed by the Permian to Jurassic shelf or platform carbonate rocks of the Khengal Group. The Khengal and basement rocks are overthrust by schist mixture, which has been called the Cottagay Series, in the northern Kohe Safi range, and they are underthrusted by concoction in the Kabul River valley [16].

The quantity of the main streams flowing into the Kabul Basin certainly contributes to the historical importance of the Kabul Region. The headwaters of the Kabul Waterway are west of the southwest angle

of the study area and passes region from the south, with currents due north about 21 km to the urban of Kabul that formerly flew east [17], leaving the reformed valley in the Safi Highlands Peaks. The Paghman Watercourse flows eastward from the Paghman Uplands and reaches the Kabul River in the city of Kabul close to the point where the Kabul River originates to flow east. The Logar River, a huge stream to the Kabul River, reaches the study area from the south from side to side with a sharp cut between mountains and runs northward for about 28 km. The Logar River combines with the Kabul River at the eastern edge of the city of Kabul, around 17 km downstream of the entry of the Paghman streams [18-20].

1.2 Geology of the Kabul Basins

Sediments are approved from Paghman, Aliabad, Asmayie, Qurugh, and Logar mountains. These altitudes are in the close regions of the Kabul Basin and these deposits are transported by water at dissimilar periods of time and form diverse thicknesses, the upper and middle portions of the Kabul Basin terrace sand there store some types of minerals, and these minerals deposits related on the source rocks that located at the immediate mounts are as of Kabul Basin [22,23]. For example, in Epidote, Kyanite, and Granite we can find terraces of the Kabul River basin since these are all sections of Metamorphic rocks (Crystalline), which are found in the mountains near the Kabul Basin. Besides, some minerals such as Rutile and Zircon also originate here because it is also some of the Igneous rocks of the Paghman Mountains strike [24]. In addition, there are some extra natural resources such as Muscovite and Biotite, also part of metamorphic rocks which is in the close mountains of the Kabul Basin, also Biotite and Rutile reserves in the inside and lower porches of the Paghman River fitting to Igneous Rocks of Paghman Mountain variety and all dregs approved by water and altogether further in terraces [25]. All rivers of the Kabul Basin are joined at reformed seats and all of them, composed, stream from west to East, and residues of this basin belong to Tertiary (Eocene and Oligocene), and the period of such sediments, surrounded by the upper and middle portions of the Kabul Basin is about (20-45) millions of years and are named Tertiary growths [26]. The upper part of these deposits is surrounded by fresh sediments of lower quaternary (Pleistocene) remains and it includes these terraces, having different composite, raises, and positions, for example, the upper part of the Kabul river basin belongs to the quaternary and here we can see more Stable and unstable gravels sediments, but the middle part of Kabul River Basin belong to Tertiary and there is certain unconsolidated sands, Marls (gray, white, green and brown) colors, and upper part of these sediments are covered by rivers terraces [27]. All mountains adjoining Kabul Province are made by means of metamorphic rocks, except for Paghman Mountains, which are shaped by metamorphic rocks, so it consists of igneous rocks also, other all mountains made from metamorphic rocks, studies using the Radiometry method. It was assessed that the lifetime of these mountains is almost (928 ± 8) million years back (**Figure 1**). The elder mountain is in the Khear Khana and the earlier one is in the Shawaky and Qurugh Mountains series [28].

The Qalay Abdul Ali is part of the Paghman District and is positioned on the common banks of Kabul-Kandahar Road. All sediments transported from different points of surrounding mountains such as the Paghman, and Chaltan Mountains are transported by surface streams and gravity to this sedimentary basin. The contribution of the accumulation of sediments by other means in this basin results in different layers and profiles. The sedimentary layers of Qalay Abdul Ali belong to the lower Quaternary (Pleistocene) and have different thicknesses. The types of sediments directly pertain to the surrounding mountains' main rocks [29,30].

1.3 Geology of Qalay Abdul Ali

The adjacent mountains of Qalay Abdul Ali are made from plutonic and metamorphic rocks (gneiss, granite). The mountains that surround this basin are Paghman Mountain ranges and they continue from northeast to southwest. Analysis of gravels shows that parent rocks are Gneiss and Granite, and it has

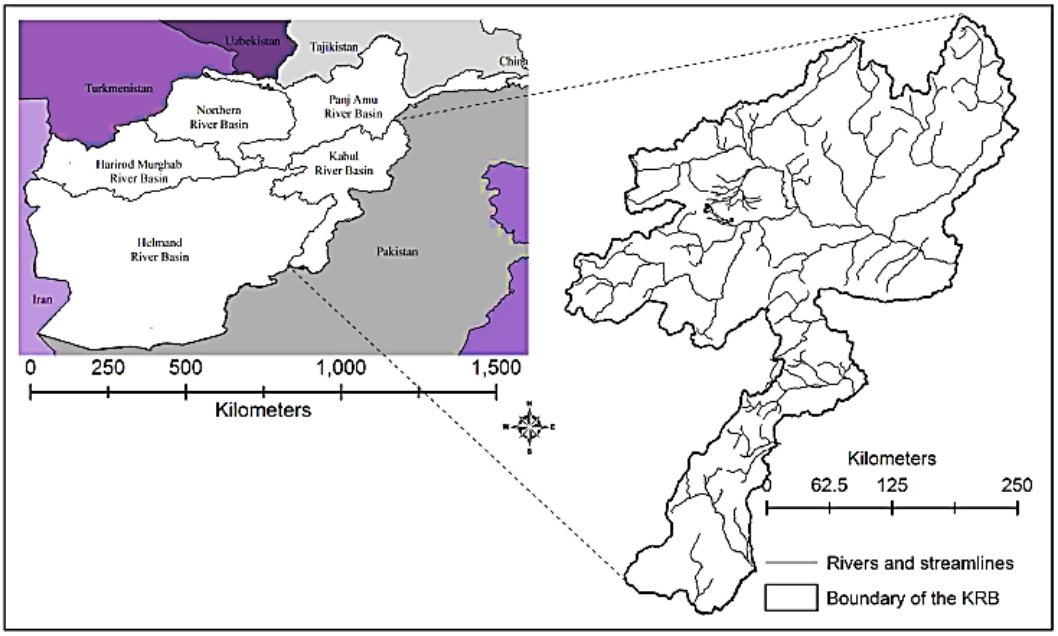

Figure 1. Site plot of Kabul basins, Afghanistan.

different sizes of bigger gravel formations. In these mountains, we found different structures such as anticline, syncline, dyke, and sill, and there are different types of valleys such as longitudinal, diagonal, transverse, synclinal, and anticlinal valleys in the area [31]. Also, there are different types of alluvial fans and alluvial aprons in the area (**Figure 2**).

1.4 The aim of research

The aim of this research is to analyze different data of soil physicochemical parameters, for six profiles of Qalay Abdul Ali to find pH, electroconductivity (EC), soil color, soil fraction, and its effects on water quality, soil quality and plants. One of the very significant goals is to quantity different parameters that impact water quality, soil quality and thereby agriculture, and its potential impact on groundwater. These parameters along with the identification of different toxic and nontoxic elements leaching into the ground impact human health with different health-related issues. Also, the amount of $CaCO_3$, found in some of these areas affects agricultural lands and thereby the quality of produce, typical to the area. Furthermore, we are also assessing different types of soil structures for groundwater infiltration rate, because the infiltration rate of such, generally platy, structures, is lower. However, in the prismatic, and columnar structures, the rate is higher. The pH indicates the amount of acidity and alkalinity of soil, in these areas and is mostly neutral, which can be used for both agricultural and drinking water. The EC shows the amount of salinity in soil which affects animals and plants. As we observe the amount of salt is normal and can be used for different purposes of agriculture and drinking water. The quality of soil is good and we can use it for different purposes of agriculture and drinking water. But in some places of Kabul province such as Qalay Zaman Khan, Taymany, and around Kabul airport the amount of EC and pH of soil are lower quality, and we cannot use them for agricultural and drinking purposes.

2. Area under investigation

This study is carried out from different soil profiles at the Qalay Abdul Ali (**Figure 2**), which is in the upper portion of the Kabul Province, on the Hindu Kush Mountain collection in the country. Kabul River starts from 80 km west side of Kabul, at an elevation of 4,522 m a.s.l in the Paghman elevation series (Sanglakh mountains regions) as part of the Hindu Kush elevation ranges in Afghanistan. The river throughout its first pass flows at a precise high

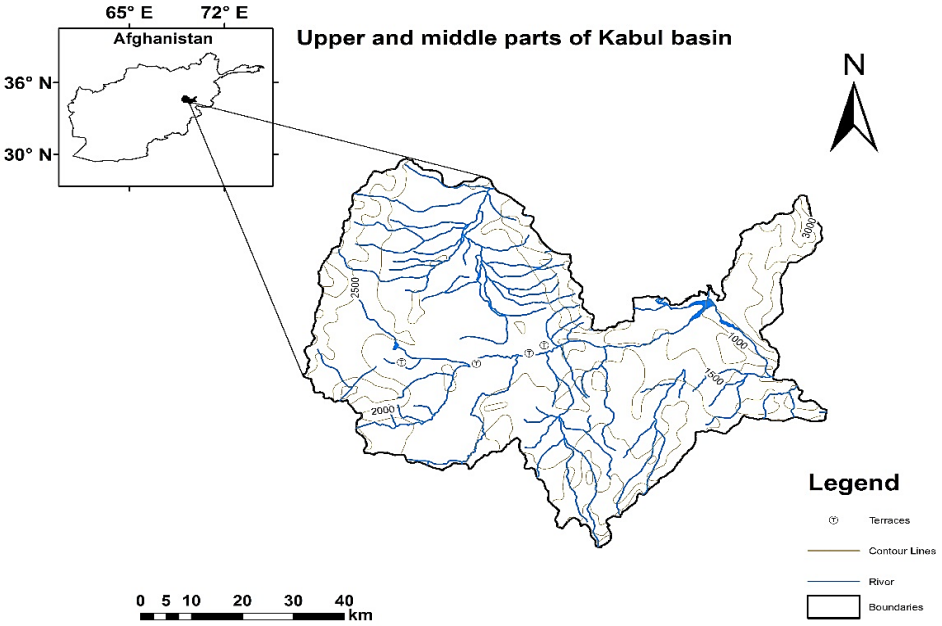

Figure 2. Scheme of the Qalay Abdul Ali basin, Kabul, Afghanistan.

speed with abundant carriage of residues from west to east and passes from the higher part of Maidan Share, Wardak Province. Afterwards, covering several kilometers, it changes direction to the southwest from Koha Qurugh and then it is called Kabul River. It then watercourses from the southwest of Lalander and arrives in Kabul City [31,32]. Paghman River starts from (3,500 m a.s.l.) Paghman Mountain Range, in the first stage the river running a very steep level and with very high velocity from north-south to Company Bridge after this river variations the course from Northwest to Northeast, and in the Gazarga area and junctions the Kabul River at Chahar Dahai. Logar River started from (4,600 m a.s.l) Daimirdad Mountain (Wardak mountain range) belongs to Wardak Province [33,34]. In the first stage, this river currents from west to east passes from Chack and Saidabad, Wardak Districts, and then enters Loger Province and Barakibarak Loger District which joins with the Charkh River. After that, it enters Kabul Province and joins with the Kabul River at the Sheena village into the Bagrami District [35,36].

3. Method and materials

In this investigation, we undertook a two-pronged approach. The first is the site or field research, in which we determine soil color by the Munsell color scheme using wet and dry conditions. The second approach is laboratory-based analysis in which we determine different chemical and physical parameters such as mechanical analysis of soil fraction, soil calcium carbonates, electro-conductivities, and soil pH, in the different locations in soil profiles at the Qalay Abdul Ali, Kabul. For the assessment to conduct this research we got 1 kg samples from every soil profile, and caring to the laboratory and performed the sieving analysis method for the determination of mixed smaller sizes we obtained 1 mg sample for determination of mechanical analysis, calcium carbonates, EC, and pH. Additionally, we study soil profiles, as well, in the field.

4. Results

4.1 Study of soil

In this research, we studied six different Pedogenic profiles which consist of profile 1, profile 2, profile 3, profile 4, profile 5, and profile 6. In these profiles, we found different types of plant roots, gravels, some caves of worms, and soil erosion, as well as in these

profiles we can find different types of arrangements such as crumbling, platy, and prismatic.

4.2 Munsell color chart

For this investigation, we assessed the soil color, following the scheme by Munsell, who selected the color for soil in 1999 at dry and wet conditions. For determination, we compared soil at the two conditions one is dry soil condition, and the second is the wet condition on six profiles of Qalay Abdul Ali regions, Kabul, Afghanistan (**Figure 3**).

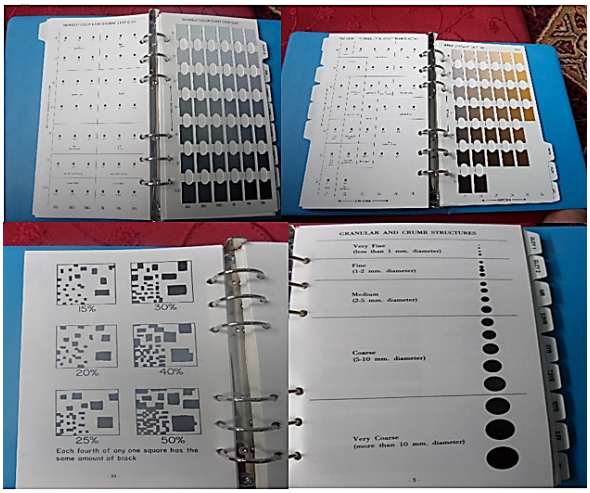

Figure 3. Munsell color chart for soil color determination.

4.3 Soil color

Rendering to the Munsell Color chart, the color of the soil in this profile 1 in the wet situation is reddish gray (2.5 YR 5/1) but in the dry state is yellowish brown (10 YR 5/6), profile 2 in the wet form is very pale brown (10 YR 8/2) but at a dry situation is reddish (10 YR 2.5/1), profile 3 at wet state is strong brown (7.5 YR 5/6) but at the dry state is reddish gray (2.5 YR 5/1), profile 4 at the wet form pale brown (10 YR 8/2), but at the dry form is strong brown (7.5 YR 5/6), profile 5 at the wet state is pinkish white (7.5 YR 8/2), reddish (10 YR 2.5/1), yellowish brown (10 YR 5/6), strong brown (7.5 YR 5/6) and at the dry state is pinkish white (7.5 YR 8/2) and at profile 6 at the wet state soil color is reddish (10 YR 2.5/1) and at the dry state is yellowish brown (10 YR 5/6) [14].

4.4 Laboratory approach

Comparative tools that we used in this investigation at laboratory and field in this study we used some laboratory devices such as a hydrometer, Calcimeter, pH meter, and Munsell color chart and we discovered the chemical and physical as well as microscope and discovered features of soil and sediments and rock type in Qalay Abdul Ali sedimentary basin.

4.5 Physical analysis

In this study, we conducted research laboratory work, such as mechanical analysis by hydrometer. In agreement with the hydrometer analysis, we establish the type of soil segment is silty loam and loam (**Figure 9**).

4.6 Calcimeter analysis

In this study from chemical laboratory work, we performed the determination of soil fractions by hydrometer analysis, $CaCO_3$ by Calcimeter, and pH and EC by pH-meter (**Figure 11**).

Profile 1

In this profile, we discover different soil structures such as platy, crumbling, and prismatic, and also found the roots of undergrowth at different depths and some gravels. After the decomposition of plants' roots, we conducted a study of different sizes of secondary pores for some live animals. During the secondary pores, there are some primary pores also, and they belong to the sizes of particles (**Figure 4**). As well as there are some caves of worms and macro animals caves also. According to the hydrometer analysis, the soil type from the A-horizon of this profile is silty loam, and the amount of calcium carbonate, EC and pH are 0.437%, 961 µs/cm, and 6.5.

Profile 2

In profile 2, there are not the same types of structures such as platy but for the other types of structures we cannot find such structures because in this profile, there is more gravel and the roots of plants

is about 1 m depth, in this profile, we are able to discovery dissimilar sizes of gravel such as cobble, pebbles, granules, sands, silts. Also, can find different sizes of worm and animal caves (**Figure 5**). When we get 1 kg soil sample of B-horizon generally the soil type is silty loam, the $CaCo_3$ is 0.6%, EC is 920 µs/cm, and pH is 7.87.

Figure 4. Soil horizon 1 at Qalay Abdul Ali Kabul.

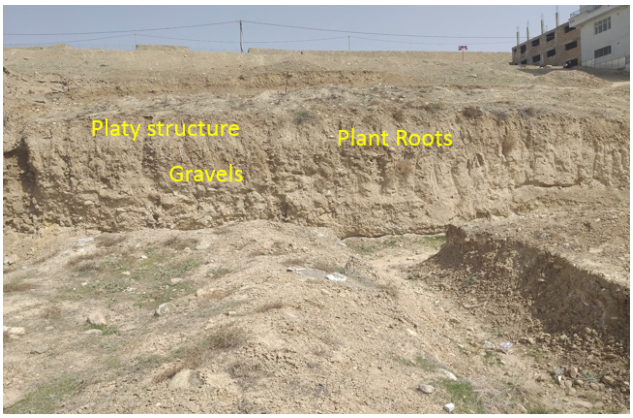

Figure 5. Soil horizon 2 at the Qalay Abdul Ali Kabul.

Profile 3

From the profile, we cannot find any gravel but there is more clay and silt, in this profile can find different types of topsoil arrangements such as platy, and prismatic. In this, we can find different forms of worms and animal caves. Also, there can understanding of altered soil erosions, the roots of plants are 1.5 m in depth (**Figure 6**). From the 1 kg sample of C-horizon of this profile, the soil type is loam, the amount of CaO_3 is 0.32%, EC is 875 µs/cm, and pH is 7.85.

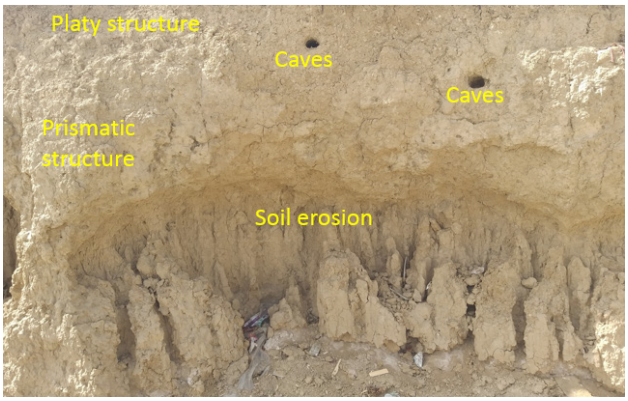

Figure 6. Soil horizon 3 at the Qalay Abdul Ali Kabul.

Profile 4

In profile 4, it is able to discover altered kinds of structures such as crumbling, and columnar. This profile is also made of silt and clay. Besides, nowadays this profile can find different sizes of caves, and roots, and there are changed soil erosion, and different categories of cracks (**Figure 7**). When we get the soil sample from A-horizon, the soil type is loam, the amount of $CaCO_3$ is 0.35%, the EC is 849 µs/cm, and the pH is 7.75.

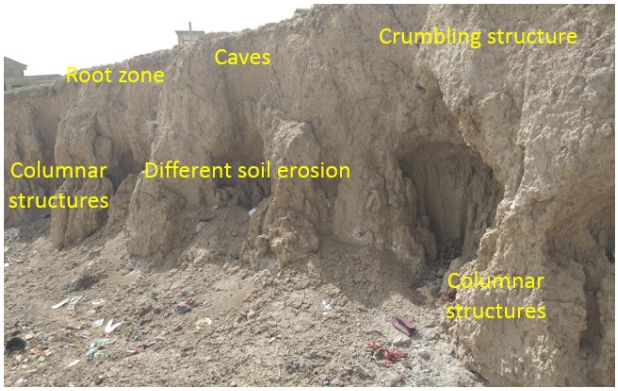

Figure 7. Soil horizon 4 at the Qalay Abdul Ali Kabul.

Profile 5

From this profile, can find different soil structures such as platy, crumbling or worm obstruct, and columnar structures. As well as in this profile we can find different caves of worms, and roots, the depth of roots is about 2 m (**Figure 8**). when we get 1 kg sample from B-horizon and analyzed it in the laboratory the soil type is loam, the amount of $CaCO_3$ is 0.46%, EC is 861 µs/cm, and pH is 7.75.

Profile 6

With this profile, we can find dissimilar worm caves, crumbling, and platy structures, as well as we can find different gravels, the depth of roots is about 1 m (**Figure 9**). When we get 1 kg sample from the C-horizon of this profile the soil type is silty loam, the amount of $CaCO_3$ is 0.474%, EC is 870 µs/cm, and pH is 7.75.

4.7 Textural triangle

In this research when we studied the sample via hydrometer the percentage of soil fine materials or fractions (sand, silt, and clay), we found by the triangle, in this triangle for found soil type from 12 classes of soil between the triangles (**Figure 10**). In this research study, generally, the soil type is silty loam and loam (**Figure 12**).

4.8 Hydrometer

In this research for soil fine materials, we used a hydrometer, as shown in **Figure 11**, for hydrometer analysis we get different samples from various horizons of profiles, and we find from the percentage of fine materials (sand, silt, clay) the soil types, as shown in **Figure 12**.

In this research for soil mechanical analysis, we used the hydrometer, and at what time we analyzed the soil sample by hydrometer the result, we found the soil types of silty loam and loam, as shown in **Figure 12**.

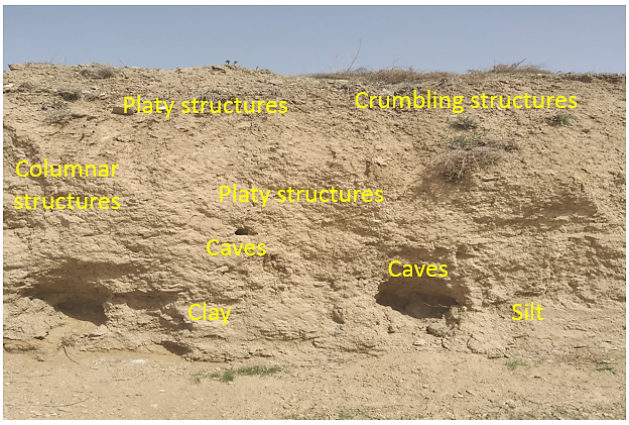

Figure 8. Soil horizon 5 at the Qalay Abdul Ali Kabul.

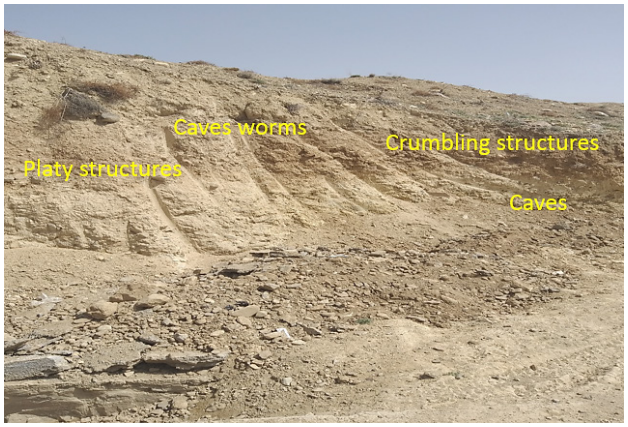

Figure 9. Soil horizon 6 at Qalay Abdul Ali Kabul.

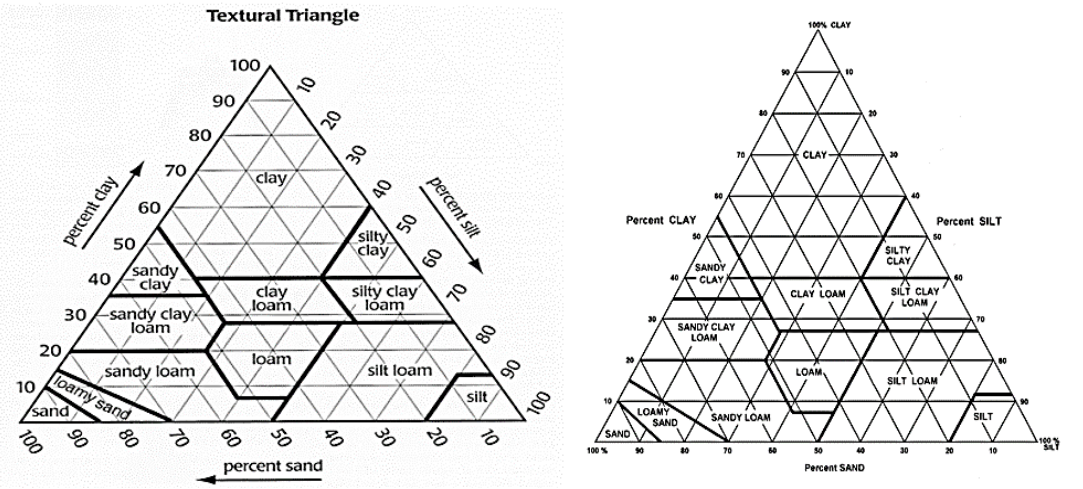

Figure 10. Triangle and 12 classes for determination of soil name from soil friction percentage.

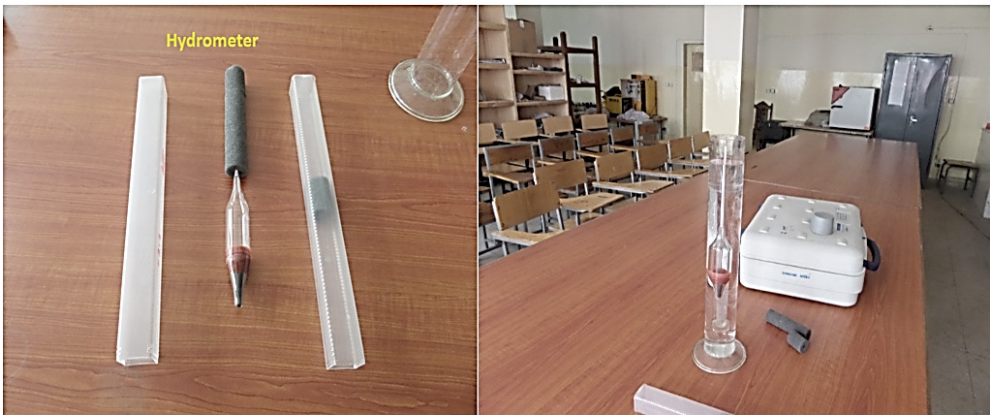

Figure 11. Device (tool) of the hydrometer for determination of soil mechanical analysis.

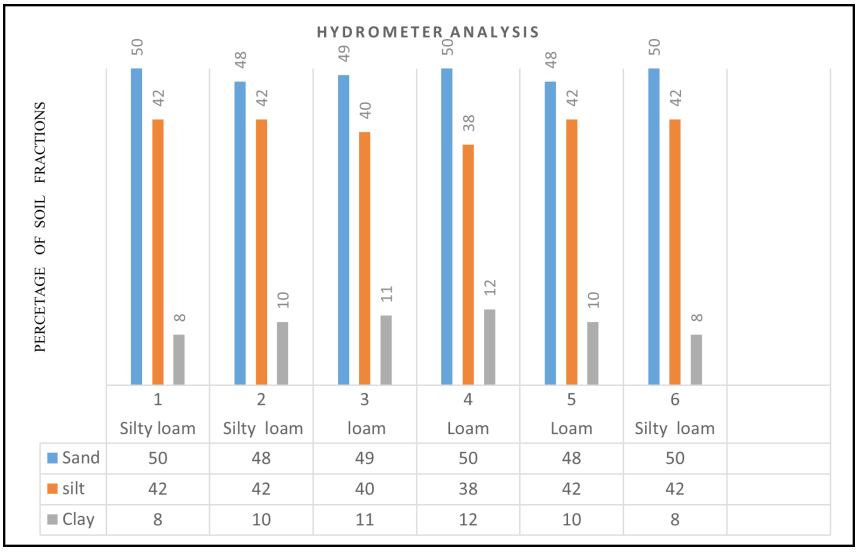

Figure 12. Determination of soil mechanical analysis by hydrometer.

4.9 Calcimeter

We conducted these experiments to find $CaCO_3$ in the soil profile. To do so, we used a Calcimeter, for doing this method we get a 1 kg sample from different horizons of profiles and it's analyzed by the sieving method, we mixed the fine sizes of sieves. After we get 1mg sample from this and mix we clean water and find the amount of $CaCO_3$ in soils of these profiles (**Figure 13**).

In this research at the Qalay Abdul Ali region soil profiles by using Calcimeter different amounts of $CaCO_3$, and this amount belongs to the location and type of soil. In these horizons of profiles, there are different amounts of $CaCO_3$: 0.437%, 0.6%, 0.32%, 0.35%, 0.46%, and 0.474% (**Figure 14**).

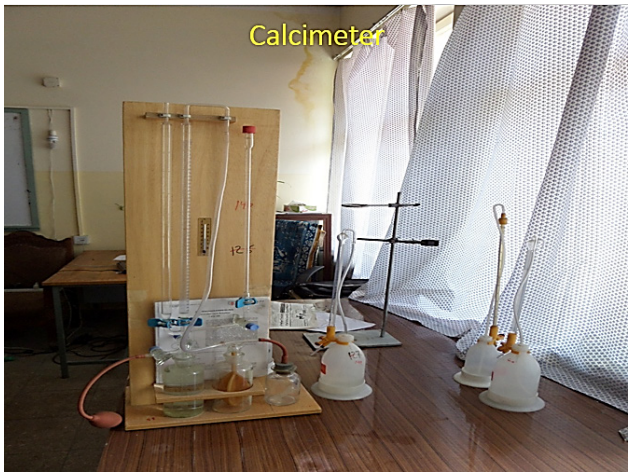

Figure 13. Calcimeter device for determination of calcium carbonates in soils.

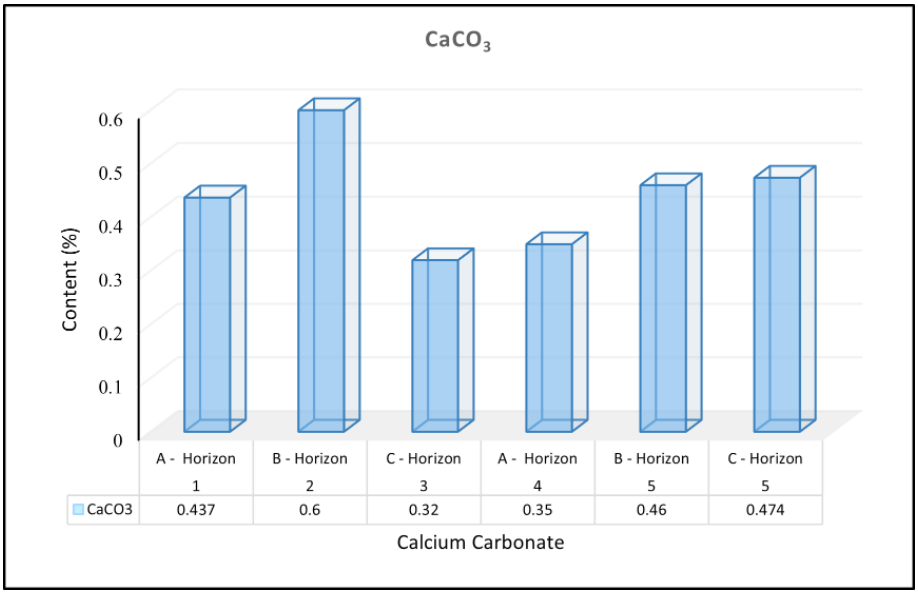

Figure 14. Determination of calcium carbonates in soils by a Calcimeter device.

4.10 pH-meter

In this research for the selection of the amount of EC and pH we used a pH meter (**Figure 15**), for these, we transported from different horizons of profiles. For determination we analyzed samples by sieving method, and after the smaller sizes were mixed after 1mg sample was analyzed by pH-meter and we find the amount of EC and pH (**Figures 16 and 17**).

In this research by pH-meter we find the different amounts of EC at the six different horizons of profiles, in this research generally the amount of EC is 961 µs/cm, 920 µs/cm, 875 µs/cm, 849 µs/cm, 861 µs/cm, and 870 µs/cm (**Figure 16**).

For the determination pH of Qalay Abdul Ali, we used the pH meter to assess the corresponding value of pH at the different horizons of six profiles. In this research, the pH around neutral consists of 6.5, 7.87, 7.85, 7.75, 7.75, and 7.75 (**Figure 17**).

Figure 15. pH-meter instrument for determination EC and pH in soils.

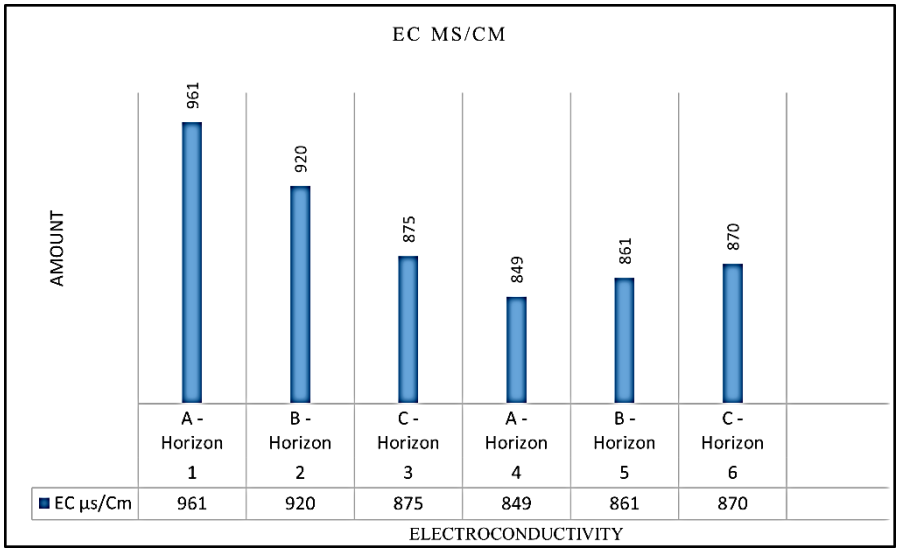

Figure 16. Determination of EC by pH-meter in soils.

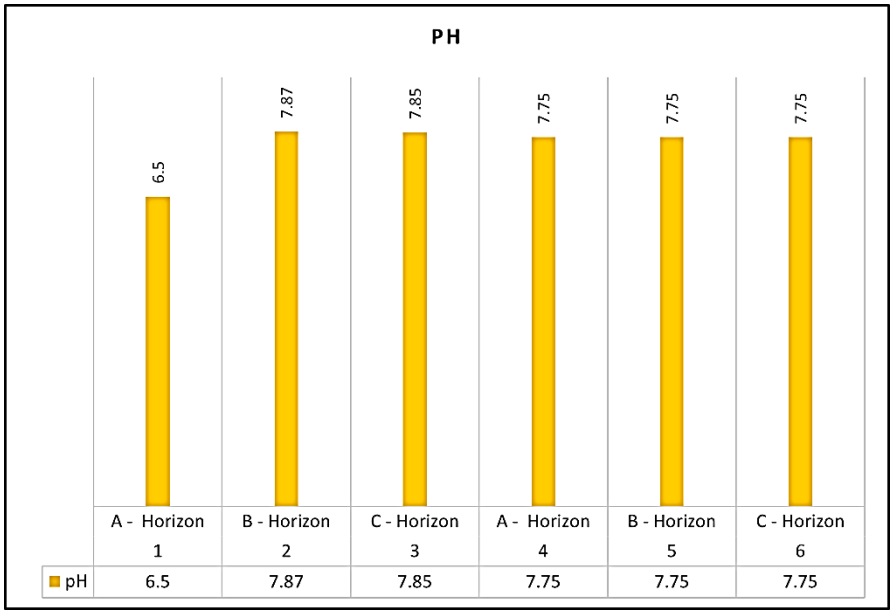

Figure 17. Determination pH by pH-meter in soils.

5. Conclusions

This physio-chemical investigation is used on six profiles to describe profiles of soil and chosen diverse masses of sand types of soils transported via surface stream discharges at the previous geological periods in Qalay Abdul Ali regions, Kabul, Afghanistan. From physical and chemical analysis, we found mechanical analysis, $CaCO_3$, electroconductivity, and pH of soils. For the determination, we conducted a mechanical analysis. We used a hydrometer on all the soil types—such as loam and silty loam. For $CaCO_3$ we used a Calcimeter and the amount of $CaCO_3$ was 0.437%, 0.6%, 0.32%, 0.35%, 0.46%, and 0.474%, for determination of EC and pH we used a pH-meter, in this research the amount of EC was 961 µs/cm, 920 µs/cm, 875 µs/cm, 849 µs/cm, 861 µs/cm, 870 µs/cm, and the amount of pH were 6.5, 7.87, 7.85, 7.75, 7.75, 7.75, and the soil colors are in the wet condition is reddish gray (2.5 YR 5/1) and at the dry condition pale brown (10 YR 8/2), strong brown (7.5 YR 5/6), pinkish white (7.5 YR

8/2), reddish (10 YR 2.5/1), yellowish brown (10 YR 5/6). In this research, the pH, EC, and $CaCO_3$ are according to national and international standards, and it's not desisted for plants growing in soils. Also, there is no risk for surface and groundwater. The outcomes proposed in this pedogenic investigation be able to be used professionally in the further catchments of the basin and further highland basins in Afghanistan.

Author Contributions

Hafizullah Rasouli (H.R.), Ashok Vaseashta (A.V.), Conceptualization: H.R., A.V.; Methodology: H.R.; Software: H.R., A.V.; Validation, H.R., A.V.; Formal analysis, H.R., A.V.; Investigation, H.R.; Resources, H.R, A.V.; Data curation, H.R., A.V.; Writing-original and draft preparation, H.R., A.V.; Visualization, H.R., A.V.

Conflicts of Interest

The authors declare no conflicts of interest regarding the publication of this paper.

Funding

This research received no external funding.

References

[1] Abdullah, S.H., Chmyriov, V.M., 1997. Map of mineral resources of Afghanistan: Kabul, Ministry of Mines and Industries of the Democratic Republic of Afghanistan, Department of Geological and Mineral Survey. V/O Technoexport USSR, scale 1:500,000.

[2] Avouac, J.P., Burov, E.B., 1996. Erosion as a driving mechanism of intracontinental mountain growth. Journal of Geophysical Research: Solid Earth. 101(B8), 17747-17769.

[3] Banks, D., Soldal, O., 2002. Towards a policy for sustainable use of groundwater by non-governmental organisations in Afghanistan. Hydrogeology Journal. 10, 377-392.

[4] Bohannon, R.G., Turner, K.J., 2005. Geologic map of quadrangle 3468. Chak-e-Wardak (509) and Kabul (510) quadrangles: Afghan Open-File Report (509/510), 1001.

[5] Bohannon, R.G., Turner, K.J., 2007. Geologic map of quadrangle 3468, Chak Wardak-Syahgerd (509) and Kabul (510) quadrangles, Afghanistan (No. 2005-1107-A). Geological Survey (US).

[6] Broshears, R.E., Chornack, M.P., Mueller, D.K., et al., 2005. Inventory of ground-water resources in the Kabul Basin. U.S. Geological Survey Scientific Investigations Report 2005-5090. p. 34.

[7] Asaad, F.A., Lamoreaux, P.E., 2004. Field methods for geologists and hydrogeologists. Springer: Verleg Berline Heidelberg.

[8] Younger, P.L., 2009. Groundwater in the environment: An introduction. John Wiley & Sons: San Francisco.

[9] Koons, P.O., 1989. The topographic evolution of collisional mountain belts; a numerical look at the Southern Alps, New Zealand. American Journal of Science. 289(9), 1041-1069.

[10] Lavé, J., Avouac, J.P., 2001. Fluvial incision and tectonic uplift across the Himalayas of central Nepal. Journal of Geophysical Research: Solid Earth. 106(B11), 26561-26591.

[11] Putnis, A., 1992. An introduction to mineral sciences. Cambridge University Press: Cambridge.

[12] Molnar, P., 1990. A review of seismicity and the rates of active underthrusting and deformation at the Himalaya. Journal of Himalayan Geology. 1, 131-154.

[13] Montgomery, D.R., 1994. Valley incision and the uplift of mountain peaks. Journal of Geophysical Research: Solid Earth. 99(B7), 13913-13921.

[14] Munsell Color Company, 1999. Munsell soil color charts. Munsell Color Company: USA.

[15] Biswas, T.D., Mukherjee, S.K., 1994. Textbook of soil science, second edition. Tata McGraw Hill Education Private Limited: New Delhi.

[16] Niard, N., 2005. Hydrogeology of Kabul Basin Part III: Modelling approach Conceptual and

Numerical Groundwater Models. Foreign Office of the Federal Republic of Germany: BGR. [Internet]. Available from: https://www.bgr.bund.de/EN/Themen/Wasser/Projekte/abgeschlossen/TZ/Afghanistan/hydrogeology_kabul_basin_3.pdf?__blob=publicationFile&v=3

[17] Nakata, T., 1972. Geomorphic history and crustal movements of the foothills of the Himalayas. Science Reports of the Tohoku University, 7th Series (Geography). 22, 39-177.

[18] Ruleman, C.A., Crone, A.J., Machette, M.N., et al., 2007. Map and database of probable and possible Quaternary faults in Afghanistan. US Geological Survey Open-file Report. 1103(1).

[19] Raymo, M.E., Ruddiman, W.F., Froelich, P.N., 1988. Influence of late Cenozoic mountain building on ocean geochemical cycles. Geology. 16(7), 649-653.

[20] Summerfield, M.A., Hulton, N.J., 1994. Natural controls of fluvial denudation rates in major world drainage basins. Journal of Geophysical Research: Solid Earth. 99(B7), 13871-13883.

[21] Torge, T., Georg, H., Thomas, H., 2003. Hydrogeology of the Kabul Basin Part I: Geology, Aquifer Characteristics, Climate, and Hydrography. Foreign office of the Federal Republic of Germany. BGR record 200310277/05 (2003): 23. [Internet]. Available from: https://www.bgr.bund.de/EN/Themen/Wasser/Projekte/abgeschlossen/TZ/Afghanistan/hydrogeology_kabul_basin_1.pdf?__blob=publicationFile&v=3

[22] Wheeler, R.L., Bufe, C.G., Johnson, M.L., et al., 2005. Seismotectonic map of Afghanistan, with annotated bibliography. US Department of the Interior, US Geological Survey: Reston, VA, USA.

[23] Arian, H., Kayastha, R.B., Bhattarai, B.C., et al., 2015. Application of the snowmelt runoff model in the Salang river basin, Afghanistan using MODIS satellite data. Journal of Hydrology and Meteorology. 9(1), 109-118.
DOI: https://doi.org/10.3126/.jhm.v9i1.15586

[24] Hamdard, M.H., Soliev, I., Rasouli, H., et al., 2022. Groundwater quality assessment in Chak Karstic Sedimentary Basin, Wardak Province, Afghanistan. Central Asian Journal of Water Research. 8(2), 102-109.
DOI: https://doi.org/10.29258/CAJWR/2022-R1.v8-2/110-127.eng

[25] Latati, A., 1986. Thoughts on karst water resources in the Middle Atlas mountains, Morocco. IAHS-AISH Publication. (161), 633-642.

[26] Urbano, L., Waldron, B., Larsen, D., et al., 2006. Groundwater–surfacewater interactions at the transition of an aquifer from unconfined to confined. Journal of Hydrology. 321(1-4), 200-212.

[27] Worthington, S.R., Ford, D.C., 2009. Self-organized permeability in carbonate aquifers. Groundwater. 47(3), 326-336.

[28] Thornthwaite, C.W., 1948. An approach toward a rational classification of climate. Geographical Review. 38(1), 55-94.

[29] Manga, M., 2001. Using springs to study groundwater flow and active geologic processes. Annual Review of Earth and Planetary Sciences. 29(1), 201-228.

[30] Sree Devi, P., Srinivasulu, S., Kesava Raju, K., 2001. Hydrogeomorphological and groundwater prospects of the Pageru river basin by using remote sensing data. Environmental Geology. 40(9), 1088-1094.

[31] Rasouli, H., 2020. Well design and stratigraphy of Sheerkhana Deep Well in Chak District, Wardak, Afghanistan. International Journal of Geology, Earth & Environmental Sciences. 10(2), 54-68.

[32] Rasouli, H., Kayastha, R.B., Bhattarai, B.C., et al., 2015. Estimation of discharge from Upper Kabul River Basin, Afghanistan using the snowmelt runoff model. Journal of Hydrology and Meteorology. 9(1), 85-94.
DOI: https://doi.org/10.3126/jhm.v9i1.15584

[33] Rasouli, H., Quraishi, R., Belhassan, K., 2021. Investigations on river sediments in Chak Sedimentary Basin, Wardak Province, Afghanistan. Journal of Geological Research. 3(4), 21-29.
DOI: https://doi.org/10.30564/jgr.v3i4.3574

[34] Rasouli, H., 2022. Climate change impacts

on water resource and air pollution in Kabul Sub-basins, Afghanistan. Advances in Geological and Geotechnical Engineering Research. 4(1), 11-27.

[35] Rasouli, H., Vaseashta, A., Hamdard, M.H., 2023. Sedimentlogical study of Chack Hydropower Reservoir, Wardak, Afghanistan. International Journal of Earth Sciences Knowledge and Applications. 5(1), 21-32.

[36] Rasouli, H., Vaseashta, A., Belhassan, K., 2023. Mechanical analysis of Khair Abad Village, Surskhrud District, Nangarhar Province, Afghanistan. International Journal of Earth Sciences Knowledge and Applications. 5(1), 103-120.

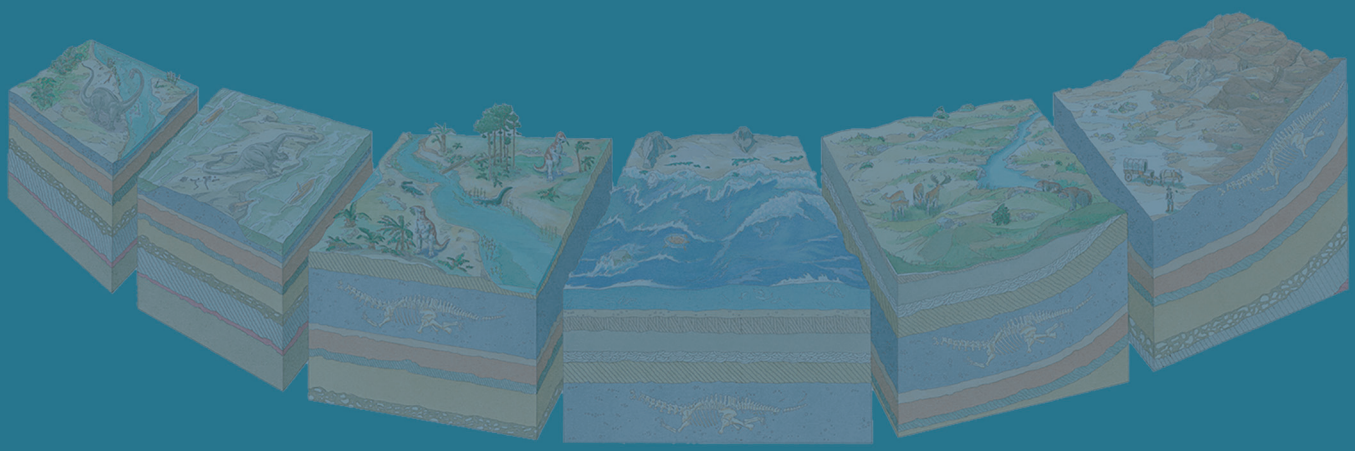

BILINGUAL PUBLISHING GROUP
Tel:+65 65881289
E-mail: contact@bilpublishing.com
Website:https://journals.bilpubgroup.com

2810-9384 03
9 772810 938231